Doctoral Dissertation

Investigation on synthesis and structure analysis of twisted graphene on graphene/SiC template

Yao Yao

Department of Applied Physics
Graduate School of Engineering
Osaka University

January 2025

Supervisor: Prof. Yoshihiro Kobayashi

Abstract

Twisted graphene with randomly stacked layers has garnered significant attention due to its exceptional electrical and optical properties, which stemmed from its linear band dispersion near the Fermi level and its screening effect that minimized the influence of substrate impurities. Traditionally, twisted graphene was fabricated by transferring monolayer graphene prepared via mechanical exfoliation or chemical vapor deposition (CVD) on copper substrates. However, contaminants introduced during the transfer process can severely impact the resulting device performance. As a result, developing a clean crystal growth technology for large-area synthesis becomes a critical challenge.

The catalyst-free CVD process on a graphene template presented a promising solution for synthesizing high-performance twisted few-layer graphene (tFLG). In this vapor-solid growth process, the formation of graphene layers with random stacking is preferred, as it is challenging for spontaneously formed graphene nanoflakes to rotate on a solid surface during nucleation. However, when using template monolayer graphene obtained through mechanical exfoliation or CVD on copper, macrostructural defects such as wrinkles and transfer-induced impurities adversely affected the vapor-solid growth process. These defects degraded the uniformity and crystallinity of the resulting few-layer graphene. To overcome these challenges, this dissertation explored innovative strategies for synthesizing high-quality twisted graphene on graphene/ silicon carbide (SiC) templates using ethanol chemical vapor deposition (CVD). The study was divided into three parts, each addressing critical challenges in the growth and control of twisted graphene structures.

In the first part of this dissertation, the overlayer growth of graphene on epitaxial graphene/SiC was investigated using ethanol across a wide temperature range from 900 ºC to 1450 ºC. Structural analysis through atomic force microscopy (AFM) and scanning tunneling microscopy (STM) revealed that graphene islands grown at 1300 ºC formed hexagonal twisted bilayer graphene with a high crystallinity and random stacking twist angles. By combining microscopic nucleation behavior and classical nucleation theory, the growth mechanism for the randomly twisted structures was also discussed. These findings demonstrated that graphene overlayer growth on an epitaxial graphene/SiC solid template at 1300 ºC was an effective method for synthesizing high-quality twisted graphene.

To obtain larger graphene islands, the growth temperature was increased to above 1400 ºC, resulting in graphene islands adopting a circular morphology. However, moiré patterns with varying periodicities were observed within individual islands, indicating that they were composed of multiple graphene domains with different twist angles. Investigation of the initial nucleation stage suggested that this phenomenon was caused by high and localized nucleation density. By analyzing multiple factors, the underlying mechanism that ran counter to conventional thermodynamic trends was elucidated.

In the second part of this dissertation, a sequential thermal (ST) process was explored as an effective approach to address the challenges of growing twisted graphene with reduced nucleation density. This method involved limiting the exposure of the graphene/SiC template to ambient air before CVD growth. AFM analysis revealed that the ST process significantly suppressed the

nucleation density of CVD graphene under identical growth conditions. Furthermore, a wide temperature range study showed that nucleation behavior changed drastically beyond a threshold temperature of 1300 °C, likely due to the onset of etching effects. Combined with the mechanism of growing graphene overlayers using ethanol as a carbon source, a specific mechanism was proposed to explain this behavior. Raman spectroscopy confirmed the successful synthesis of twisted graphene, with the G' band analysis indicating a high ratio of twisted structures in the grown graphene.

However, the nucleation behavior on ST-treated graphene/SiC surfaces proved highly sensitive to carbon source concentration and process temperature. On the clean graphene/SiC surface prepared via the ST process, higher carbon source partial pressure was required compared to air-exposed (AirE) surfaces. Despite improvements, multilayer island structures persisted, with relatively few monolayer regions, which hindered achieving large-area, layer-by-layer growth of tFLG.

In the third part of this dissertation, a carbon dioxide (CO_2)-assisted etching process was employed to create active sites on the graphene/SiC template surface, facilitating nucleation and growth directly on the terraces of the graphene/SiC structure. By optimizing temperature, pressure, and etching time during the etching stage, CO_2 etching of graphene/SiC was performed under the optimized conditions of 1150°C, 80 kPa, and 1 minute. This process successfully facilitated the nucleation and growth of twisted monolayer graphene from the active sites on the etched graphene/SiC in the subsequent CVD stage. Remarkably, a regrowth of the graphene/SiC template during the subsequent CVD growth stage was observed by comparing untreated graphene/SiC, CO_2-etched graphene/SiC, and CVD-grown graphene. Structural analyses using Raman spectroscopy, AFM, and SEM confirmed the regrowth of the template graphene and the successful synthesis of monolayer graphene under optimal conditions. Therefore, controlling the extent of CO_2 etching was crucial to balance the regrowth of the graphene/SiC template with the growth of an additional graphene layer during CVD. Additionally, to enhance the comprehensiveness of the research framework, this study investigated the effects of etchants during the CVD growth process and presented findings from the two-stage growth of twisted graphene, providing an effective method for the uniform synthesis of large-area tFLG. The CO_2-assisted etching approach effectively activated the clean surface, creating a reliable pathway for the nucleation and layer-by-layer growth of twisted graphene on graphene/SiC templates.

This dissertation presented a series of innovative methods for synthesizing high-quality twisted graphene on graphene/SiC templates. First, through analysis of twisted structures and investigation of their growth behavior, a catalyst-free CVD-based method was developed to produce high-crystallinity, randomly stacked twisted graphene. Second, an effective strategy for suppressing local nucleation during graphene growth was established using the ST process, with a mechanism that elucidated nucleation behavior at a threshold temperature of 1300 °C. Lastly, a novel approach for growing twisted monolayer graphene on clean surfaces was introduced, employing CO_2 as an etchant to induce nucleation on graphene/SiC terraces and thus advanced layer-by-layer growth. This work established a solid foundation for the large-scale production of high-quality tFLG and offered extensive opportunities for studying its physical properties and exploring its applications.

Table of Contents

Chapter 1. Introduction

1.1 Introduction of twisted graphene

Since 2004, when Geim and Novoselov first exfoliated graphene sheets from graphite using adhesive tape, the unparalleled electronic properties of graphene were discovered [1]. Shortly afterward, they discovered an entirely new quantum Hall effect and proposed that graphene's charge carriers behave like massless high-energy particles traveling at relativistic speeds [2]. These groundbreaking findings earned them the Nobel Prize in Physics in 2010. This single-layer graphene (SLG), just one carbon atom thick, is poised to spark an unprecedented technological revolution in industry.

As graphene research continues to deepen, the stacked multilayer structure of graphene has attracted more and more scientific interest. When two single-layer graphene (SLG) are stacked and form bilayer graphene (BLG), the deformation of the Dirac cone degrades the above excellent properties. As the number of layers increases, the three-dimensional properties become stronger, and graphene eventually transforms into graphite [3]. Fortunately, it has been reported that rotational stacking can significantly improve the physical properties of graphene to approach the original SLG behavior [4,5]. More interestingly, recent studies have achieved breakthrough results from enhanced optical absorption [6,7] to superconductivity [8–10] of graphene with specific twist angle, which are completely beyond the scope of original SLG. Therefore, the twisted structure of graphene has aroused great enthusiasm and even inspired the formation of a new field of twisted two-dimensional (2D) materials.

1.1.1 Structure and properties of twisted graphene

Graphene is a single layer of carbon atoms arranged in a hexagonal lattice, derived from graphite. This 2D crystal features a honeycomb structure formed by sp^2-hybridized

carbon atoms (Figure 1.1(a)). The nearest-neighbor carbon bond length is 1.42 Å, with a lattice unit constant of 2.46 Å (Figure 1.1(b)). Of particular importance to the physics of graphene is its semi-metallic behavior, arising from the linear dispersion near the Dirac point (the K point at the corners of the graphene Brillouin zone) (Figure 1.1(c)) [11–13].

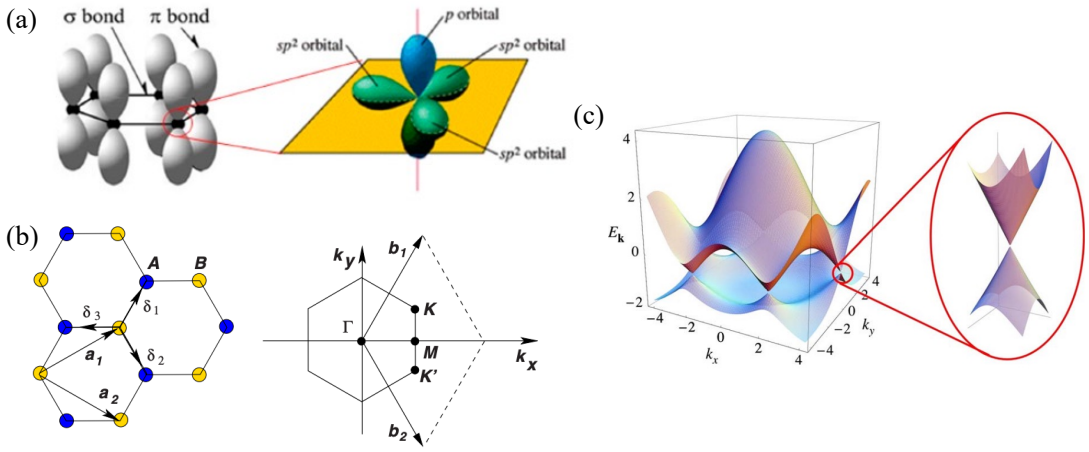

Figure 1.1 (a) σ and π bonds in graphene. (b) Honeycomb lattice and its Brillouin zone. ($\boldsymbol{a_1}$ and $\boldsymbol{a_1}$ are the lattice unit vectors, and δi, $i = 1, 2, 3$ are the nearest-neighbor vectors. (c) Electronic dispersion and Dirac point (zoom in) in the honeycomb lattice.

Graphene exhibits a wide array of extraordinary properties, primarily arising from the unique characteristics of Dirac fermions. One remarkable characteristic is its unexpectedly high opacity for an atomic monolayer, with a white light absorption rate of 2.3% [14,15]. The electrical characteristics show that the electron mobility at room temperature is very high, and the experimentally reported value 10,000 ~ 15,000 $cm^2 V^{-1}s^{-1}$ for exfoliated graphene on SiO_2-covered silicon wafers [1,16]. Its exceptional intrinsic carrier mobility facilitates low power consumption and rapid response, making it highly advantageous for high-speed electronic devices, efficient ambipolar gating, and superior chemical sensitivity [17–19]. Moreover, graphene retains its electronic properties even at the nanometer scale, providing a critical advantage for miniaturizing

devices and achieving advanced integration [20–23].

Twisted graphene is a new type of graphene system involving angular twists between highly crystalline two-dimensional layers. The rotation between two graphene layers generates periodic moiré patterns with an enlarged unit cell (Figure 1.2(a)). When two graphene layers are superposed with a relative twist angle, their corresponding Brillouin zones also rotate relative to each other. This results in a separation of the Dirac cones from the two layers by a distance that increases with the twist angle, given by $\Delta K = 2K\sin(\theta/2)$, where $K = 4\pi/3a$ (Figure 1.2(b)). More than 30 years ago, scanning tunneling microscope (STM) observations revealed periodic superlattices on the graphite surface [24], which were accurately interpreted as moiré patterns arising from a misalignment of graphite. For twisted bilayer graphene (tBLG), the moiré patterns form strictly periodic superlattices only at discrete commensurate angles. However, at infinite wavelengths outside the moiré period, scanning probe microscopy is visually dominant, enabling the identification of an infinite number of tBLG structures over the entire range of twist angles. In the following sections, this property is exploited to calculate the angles of tBLG.

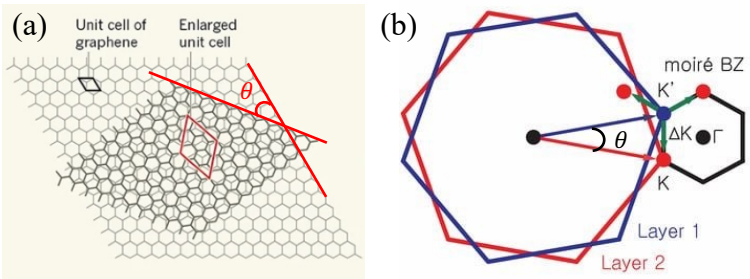

Figure 1.2 (a) Schematic of twisted bilayer graphene [25]. (b) Brillouin zone (BZ) of tBLG with the separation between Dirac cones, ΔK [26].

Graphene layers are typically arranged in an AB stacking configuration in graphite, where interlayer interactions disrupt the relativistic behavior of charge carriers inherent to single-layer graphene (SLG) [27–29]. However, this changes dramatically when graphene layers are stacked with a rotational misalignment or twist angle θ [26,30,31]. Theoretically, in twisted graphene, the relative rotation alters the band structure of the electrons, distinguishing it from the band structure of AB stacked graphene (Figure 1.3(a)). The electronic structure is modified, with the dispersion near the Fermi surface becoming linear (Figure 1.3(b)) [5], which is similar to the structure observed in SLG, even for epitaxial graphene films tens of layers thick [30]. However, the exact band structure is highly sensitive to variations in the rotation angle, with angular electron velocities undergoing renormalization [32]. For large angles ($15° \leq \theta \leq 30°$), the Fermi velocity closely matches that of graphene. For intermediate angles ($3° \leq \theta \leq 15°$), perturbation theory [33] accurately predicts the velocity renormalization. In contrast, for small rotation angles ($\theta < 3°$), a distinct regime emerges with are very flat bands (Figure 1.3(c) and (d)), where the velocity approaches zero.

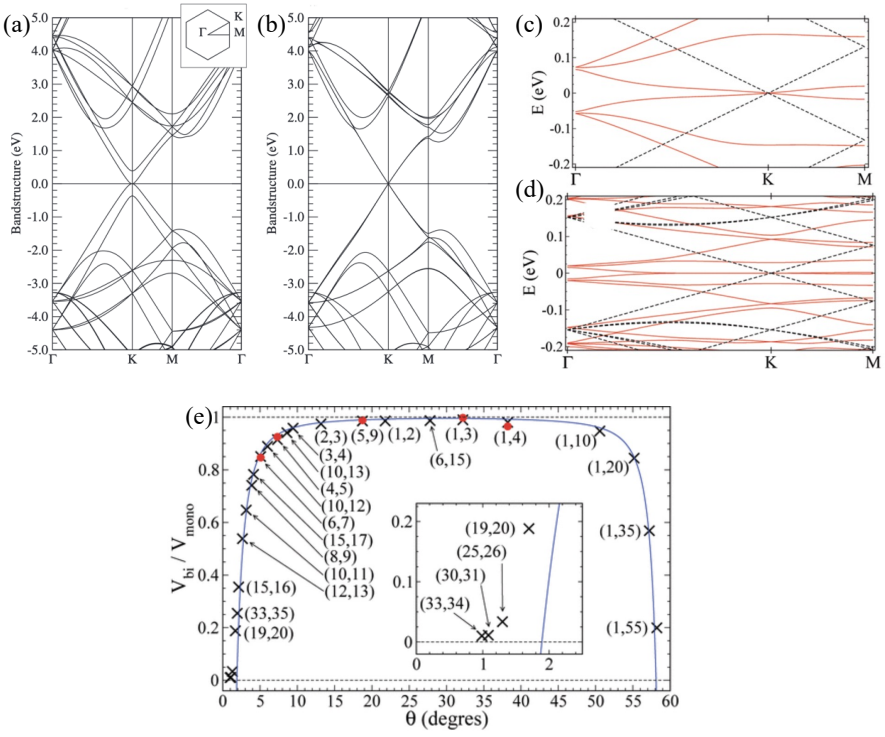

Figure 1.3 The 2D electronic band structures of Bernal AB (a) and twist (turbostratic) bilayer graphene with misorientation at (b) 38.21° [5], (c) 1.70°, (d) 0.99°. (e) Velocity ratio Vbi /Vmono for bilayer cell versus rotation angle θ [32].

In twisted bilayer graphene with a small twist angle, the formation of flat bands in the electronic energy structure has attracted widespread attention due to the Van Hove singularities [34,35] and superconductivity [8–10,36] near the magic angle (1.1°). For few-layer graphene (FLG) (<10 layers) with large twist angles and thicker twisted multilayer graphene (>10 layers) like turbostratic graphene, its electronic structure not only resembles that of single-layer graphene (SLG) due to the twisted configuration and weak interaction between graphene layers [37,38], but the multilayer structure also effectively suppresses substrate scattering from carrier impurities and enhances the uniformity of carrier transport pathways [39–41]. This leads to higher carrier mobility and conductivity compared to monolayer graphene, making them promising for applications in high-performance devices [42–44].

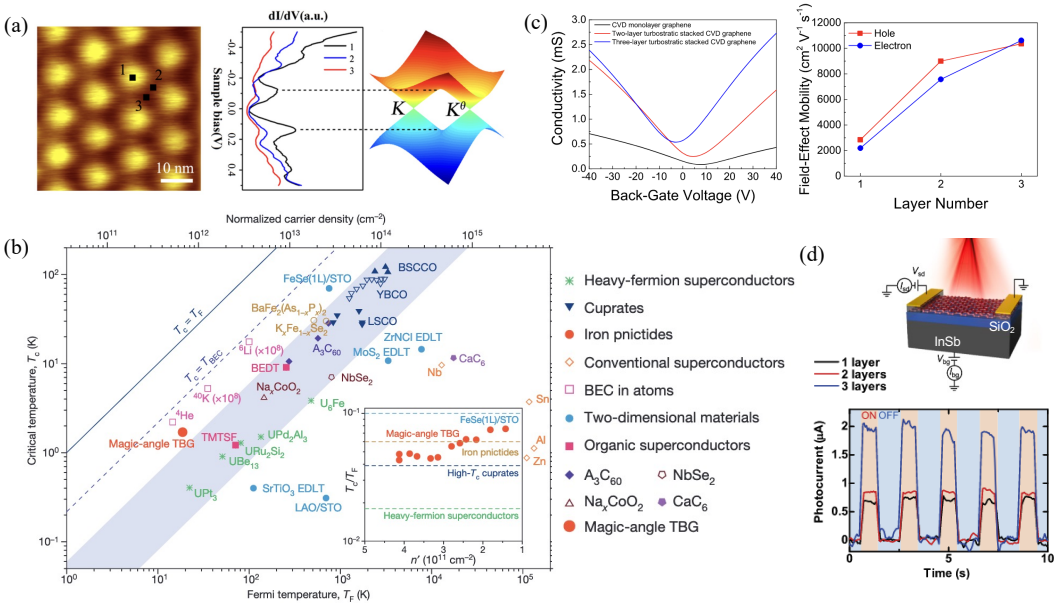

Figure 1.4 (a) two saddle points (VHSs) from a separation of ΔK in a graphene bilayer

with the twisted angle ~1.1° [35]. (b) comparing magic-angle tBLG in the context of other superconductors [8]. (c) conductivity and field-effect mobility for turbostratic stacked graphene [42]. (d) High-responsivity turbostratic stacked graphene mid-wavelength infrared detector [44].

1.1.2 Synthesis of twisted graphene

Chemical vapor deposition (CVD) allows precise control over the thickness and morphology of graphene crystal growth, making it a powerful method for large-scale industrial production [45]. By utilizing various carbon-containing precursors, such as methane, ethylene, or acetylene, the process decomposes these carbon sources at high temperatures in the presence of a metal catalyst, typically copper or nickel, facilitating the deposition of carbon atoms that assemble into high-quality graphene crystals with controlled thickness and morphology. In recent years, CVD has achieved significant success in synthesizing SLG [46–49] and AB-stacked multilayer graphene [50,51]. For the synthesis of twisted graphene, adjusting the CVD growth conditions on low-carbon-solubility transition metal substrates, such as Cu-foils (Cu-CVD), results in the random formation of AB-stacked regions and twisted structures. The tBLG produced typically exhibits lateral sizes ranging from 1 μm to 10 μm, with the twist angle distribution favoring regions of small and large rotational mismatch [52–54]. Moreover, taking advantage of the high solubility of carbon in the Ni layer, Ni-Cu alloy was used to achieve large-area tBLG growth by controlling the atomic ratio of Ni [55,56] or the Ni-Cu gradient structure [57].

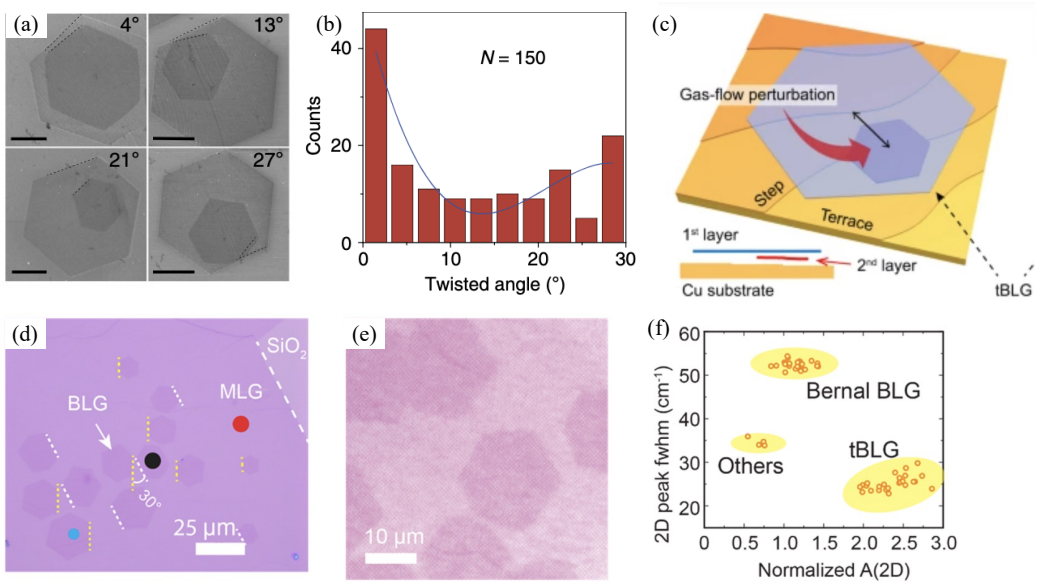

Figure 1.5 (a,b) morphology and stacking order preference of tBLG grown on a Cu substrate [53]. (c) Structural schematic of the tBLG on a Cu substrate [54]. (d-f) morphology and stacking order preference of graphene grown on a Ni−Cu gradient alloy [57].

Silicon carbide (SiC) epitaxy, which involves the evaporation of silicon atoms and the subsequent reconstruction of carbon atoms on the SiC surface, enables the growth of graphene films at extremely high temperatures, offering a reliable method for producing uniform and defect-free graphene layers [58]. SiC has two polar faces: the Si-terminated face of SiC(0001) and the C-terminated face of SiC(000-1). The graphene grown on these two faces exhibits different layer number and stacking orders [59]. Graphene grown on the Si-terminated face tends to expand layer by layer from the surface, typically used for the fabrication of high-quality SLG, AB stacking BLG and AB or ABC stacking FLG [60–65]. By purposefully treating the SiC substrate to create an appropriate crystalline surface, the morphology and layer number of graphene can be effectively controlled [66]. In contrast, on the C-terminated face, graphene may grow in a multilayer form, with varying interlayer rotational angles, potentially resulting in partially twisted layers. It has

been demonstrated that regions of multilayer graphene with Bernal stacking coexist with layers composed of twisted bilayer graphene [30,67,68].

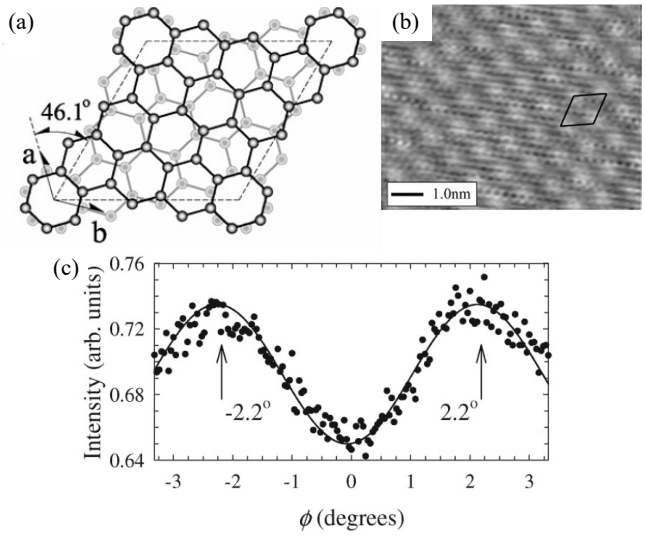

Figure 1.6 (a) Schematic of two graphene layers rotated at 32.204°. (b) STM image and (c) stacking order preference of graphene grown on a C-face SiC [30].

The folding method originated from the accidental folding of graphene when the graphite was mechanically peeled off. To improve the control accuracy of the folding process, researchers have approached the challenge from different aspects. 1) Ultrasound was used to excite several layers of graphene in suspension, and washing the flakes bonded to the substrate with water resulted in transversely folded twisted regions [69,70]. 2) In nanofabrication using atomic force microscopy (AFM), a particularly effective and controllable folding method was proposed [71]. By applying a strong interaction force between the tip and the sample, folded graphene structures can be mechanically fabricated by repeatedly tracing a programmed path within a microscale range [72]. 3) Using a customized SiO_2/Si substrate with hydrophobic and hydrophilic regions, the single-layer graphene obtained by Cu-CVD forms tBLG with a twist angle during the transfer process [73].

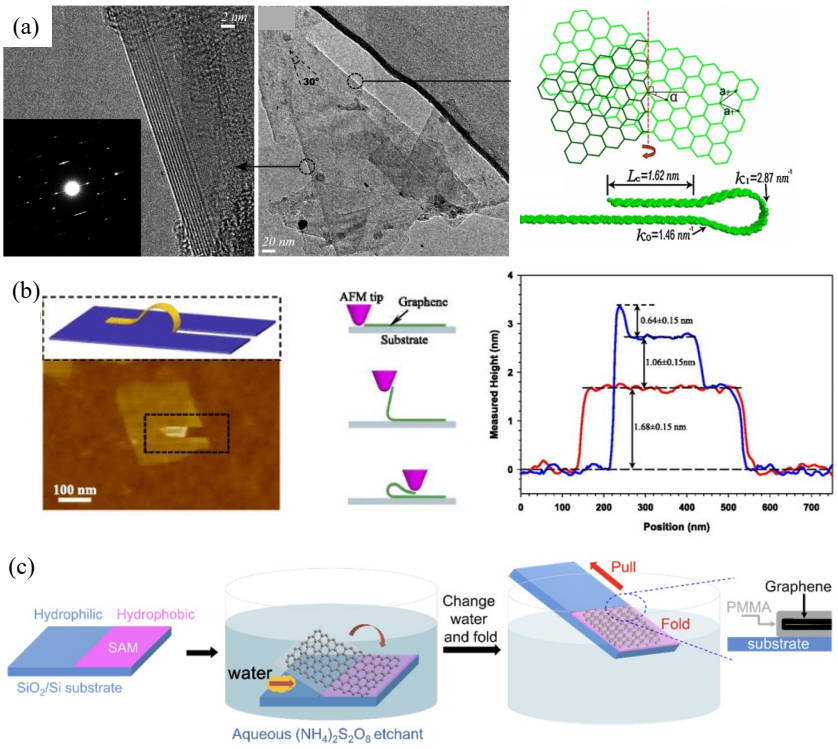

Figure 1.7 (a) TEM image of a multilayer graphene sheet and schematic of folding a graphene sheet with 22.5° [70]. (b) AFM image of one graphene sheet with a self-folded stripe [72]. (c) Schematic of the folding process of a monolayer graphene film [73].

Multiple transfer of SLG is one of the most common methods to obtain twisted graphene. This method involves transferring one SLG onto another to create a stacked structure. Since the discovery of graphene [1], mechanical exfoliation of bulk graphite onto polymers, followed by stacking onto substrates, has been a reliable method for obtaining two-dimensional graphene [74]. The exfoliation method offers the dual benefits of high quality and low cost, as well as the advantage of controllable twist angles, making it particularly appealing. Angular control in twisted graphene systems was initially achieved by using the vertical edge or femtosecond-laser-cut line of the sample as a reference for crystal orientation, providing a rotational misalignment accuracy of approximately 1° [75,76]. With advancements in techniques, the precision of twist angle control has significantly improved, achieving accuracies within 0.1° to 0.2°. To facilitate

the process, a hemispherical handle was employed to cut the monolayer graphene, allowing a portion to be separated and redeposited onto the remaining SLG following the transfer process [26,77].

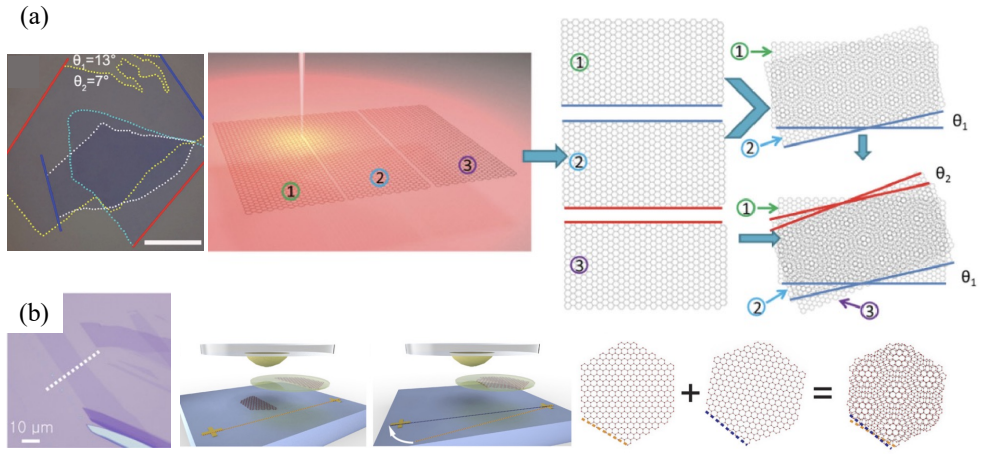

Figure 1.8 Optical micrograph and schematic illustration of the tBLG fabricated by a (a) femtosecond laser cutting technique [76] and (b) a hemispherical handle transfer technique [78].

To break through the size limitation of graphite, the starting SLG was commonly obtained by CVD methods. By wet transfer of SLG obtained from Cu-CVD is an effective way to obtain random stacked or angle aligned twisted graphene [79–82]. During the stacking process, the organic polymer that assists the transfer of graphene remains at the interface, resulting in a decrease in the quality of graphene. Therefore, researchers have made many efforts[83] to advance the quality by treatments of transferred graphene, including annealing [84],CO_2 etching [85], acetic acid method [86], VU/ozone [87] and macro-cleaning operations [88,89].

1.1.3 Structure characterization of twisted graphene

For twisted graphene, the evaluation of the rotation angle is a key step in its structural analysis. For twisted graphene, evaluating the rotation angle is an important item for its structural analysis. There are three common methods: 1) Directly measure the rotation angle of two layers of graphene with a goniometer. In some cases, graphene has smooth straight edges, and the atoms are evenly arranged without grain boundaries, so the rotation angle of the two layers of graphene is projected on the relative position of the edge, which can be called the twist angle of the lattice structure (Figure 1.9(a)). Generally, CVD technology can achieve the growth of tBLG consisting of two layers of hexagonal single-crystalline graphene with straight edges [54,90]. 2) Calculated by the period of the moiré superlattice. The close contact and interlayer interaction of two periodically arranged graphene layers produce a moiré superlattice. The period (D) of the moiré pattern is related to the twist angle (θ) and lattice constant (a) of graphene as follows:

$$D = \frac{a}{2\,sin(\theta/2)} \quad ...(1.1)$$

Technically, the moiré pattern of tBLG can be directly observed in real space by obtaining atomic-level images through scanning electron microscopy (STM) [91]. 3) Diffraction pattern of the twist angle. For SLG and AB stacking graphene, there is only one set of diffraction spots with a hexagonal shape. The diffraction pattern of tBLG has 12 spots, which can be regarded as a combination of two sets of hexagonal diffraction patterns with rotation angles. The twist angle is reflected in the rotation of the two sets of diffraction spots (Figure 1.9(b)). For randomly stacked twisted graphene, the number of hexagonal diffraction points increases with the increase in the number of layers until a diffraction ring is formed. Based on this, the selected area electron diffraction (SAED) (Figure 1.9c) and low-energy electron diffraction (LEED) (Figure 1.9d) patterns can be used to characterize the twist angle [92–94].

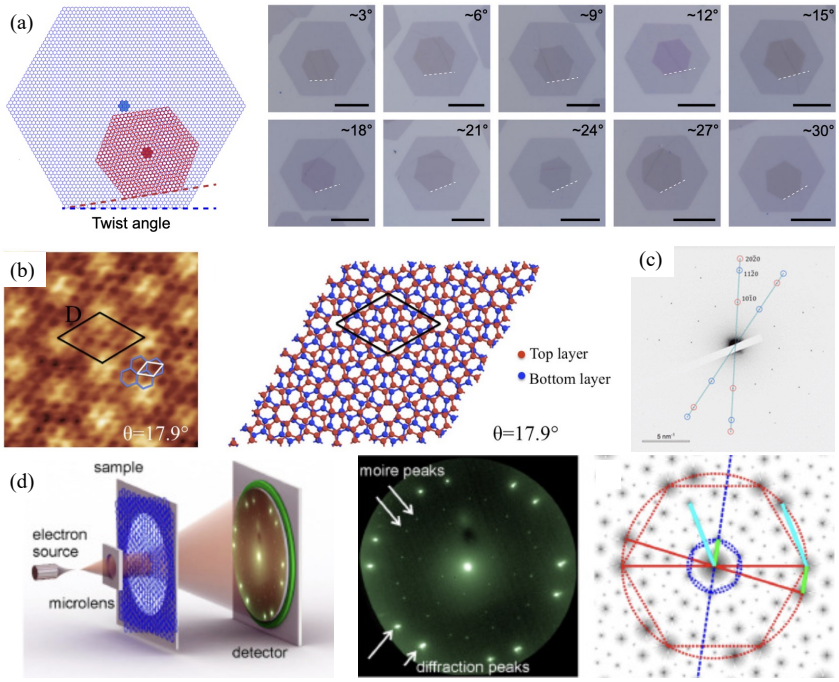

Figure 1.9 (a) optical microscope (OM) images of as grown tBLGs with twist angles. The twist angle is measured relative to the straight side of the hexagon [54]. (b) (3×3 nm^2) STM image showing the moiré superlattice (black unit cell), the graphene lattice (white unit cell) and the graphene honeycomb structure (blue), and scheme of the moiré pattern [91]. (c) 30°-tBLG SAED pattern. (d) Sketch of LEED equipment, experimental and simulated diffraction pattern of tBLG [93].

In addition, since the twist angle shows a strong correlation in some graphene observation methods, it can also be used as a basis for determining twisted graphene. It mainly involves the color variation of optical imaging with transferred tBLG ($2° < \theta < 15°$) on SiO_2/Si substrates [95] and rotation-dependent trends in the position, width and intensity in Raman spectrum. The rotation-dependent G' and G bands are experimentally established and accounted for theoretically in terms of the changes in electronic band structure [96–98]. Moreover, the frequencies of the R band and G' band based on superlattice and double resonance effect [99–101] provides important information of the

identification of twisted structure.

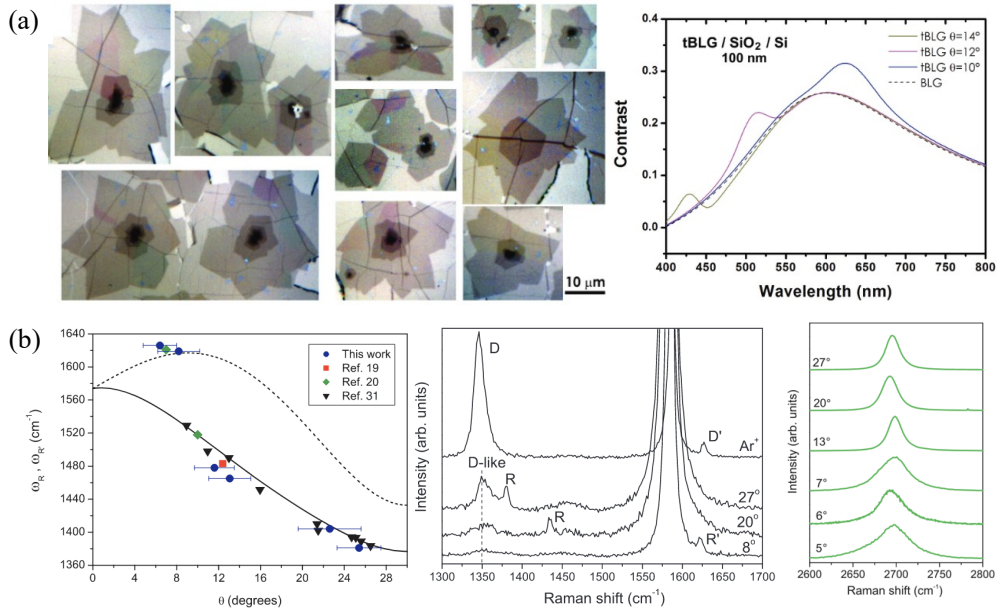

Figure 1.10 (a) optical imaging of tBLG and the calculated optical contrast spectra for tBLG/SiO_2/Si systems with different twist angles. (b) R′ and R bands frequencies as a function of the twist angle θ, Raman spectra of tBLG with R band and D band with E_L=2.41eV [99].

1.2 Introduction of crystal growth

1.2.1 Classical nucleation theory

In general, the surface of the crystal features structures such as flat terraces, steps with varying edges, and bent kinks along the steps (Figure 1.11(a)). In vapor-solid growth system, when atoms from the vapor phase are deposited onto a crystal surface, they are first adsorbed onto the flat terraces. While moving around the surface driven by thermal fluctuations, these atoms eventually incorporate at the kinks. This is primarily because kinks possess more dangling bonds than terraces or exhibit the lowest surface potential energy ($U_{kink} < U_{step} < U_{surface} < U_{vapor}$, U is potential energy). The movement of atoms across the surface is known as surface diffusion, and the subsequent process where atoms

become strongly bound at kink positions (Figure 1.11(b)) can be considered a crystallization process. In contrast, when the crystal surface is nearly atomically flat with few kinks or defects, atoms deposited from the gas phase diffuse across the surface of the crystal substrate. These atoms cluster into groups of two, three, or more, forming covalent bonds as precursors for two-dimensional nucleation. Subsequently, steps are created to facilitate the expanding growth of the crystal.

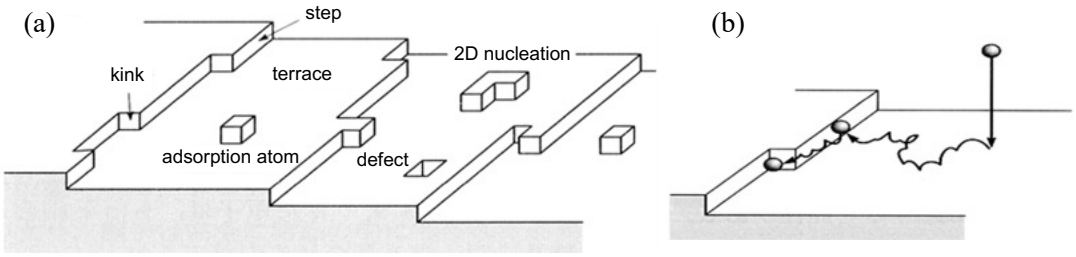

Figure 1.11 (a) Topography of crystal surface. (b) Atom adsorption, surface diffusion and crystallization. [102]

1.2.2 Microscopic nucleation behavior of graphene

The initial nucleation process on graphene templates can be described as follows: carbon monomers or dimers adsorb and diffuse across the surface, acting as carbon sources that form carbon chains. Once the chain length exceeds 6–12 carbon atoms, a more stable sp^2-hybridized carbon network begins to emerge, commonly referred to as a graphene nanoflake (C_N, where $N > 6$) [103].

Compared to adsorption on metal surfaces (e.g., ~0.6–0.8 eV/atom for $C_{N=16}$ on Ru(111), Ni(111), and Cu(111) [104], average result considering edge-to-metal bonding), the weak van der Waals interactions (~0.02 eV/atom [105]) binding these nanoflakes to the graphene template are far less robust. As a result, small nanoflakes are prone to desorption. As shown in Figure 1.12, carbon atoms (carbon precursors) depositing on the graphene template, driven by thermally activated collisions, have a certain probability of

bonding with surrounding precursors to form carbon chains or nanoflakes. When the nanoflake is small, it tends to desorb from the surface, returning to the gas phase and participating in subsequent adsorption and diffusion. However, once it grows beyond a critical size, it remains anchored to the template, acting as a nucleation center that continues to expand by incorporating activated carbon precursors at its edges.

This behavior aligns with classical nucleation theory of two-dimensional nucleation [106], which states that a stable and larger graphene nanoflake can only form once it reaches higher thermodynamic stability.

According to classical nucleation theory, when a two-dimensional nucleus of radius r forms on the crystal surface, the change in Gibbs free energy (ΔG) is described by [107]:

$$\Delta G = -\pi r^2 a\Delta\mu + 2\pi r a\sigma \ldots (1.2)$$

Here, σ represents the surface energy of the nucleus, a is the step height, which is also the interplanar spacing and $\Delta\mu$ is the change in potential energy for an atom transitioning from the gas phase to the solid phase, serving as the driving force for crystal growth. For the crystalline growth of graphene, nucleation typically occurs in the form of hexagons. Therefore, the Gibbs free energy of a graphene nucleus with a side length of r_H is given by the following expression:

$$\Delta G_H = -\frac{3\sqrt{3}}{2} r_H 2a\Delta\mu + 6 r_H a\sigma \ldots (1.3)$$

The variation of Gibbs free energy with the nucleus side length r_H exhibits an initial increase followed by a decrease, reaching a maximum before diminishing as the nucleus grows. The critical side length r_H* and the corresponding maximum Gibbs free energy ΔG_H* increment are expressed as:

$$r_H{}^* = \frac{\sqrt{3}\sigma}{\Delta\mu} \ldots (1.4)$$

$$\Delta G_H{}^* = \frac{3\sqrt{3}\sigma^2 a}{2\Delta\mu} \ldots (1.5)$$

In the early stages of nucleation, nanoflakes are unstable. Only a small fraction of nanoflakes manages to reach the critical size r_H*, where the Gibbs free energy increment reaches its maximum, marking a critical equilibrium state between growth and desorption. This critical size is referred to as the nucleation size. The corresponding maximum Gibbs free energy increment, ΔG_H*, is known as the nucleation barrier. This barrier represents the energy threshold that must be surpassed for crystal growth to proceed. Before the nucleation barrier is reached, nanoflakes undergo repeated aggregation and disintegration, with growth being an endothermic process that occurs very slowly and can be considered a quasi-thermodynamic equilibrium process. Once the nanoflake surpasses the critical size, the Gibbs free energy increment decreases further as the nanoflake grows, and the nanoflake begins to grow rapidly in a continuous manner, driven by kinetic processes.

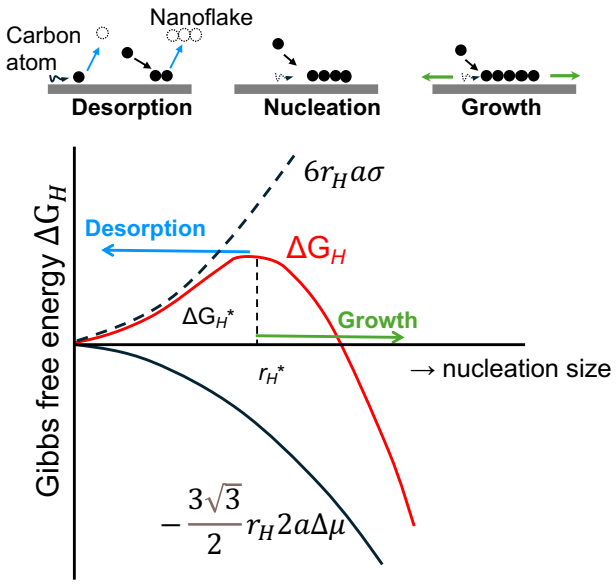

Figure 1.12 Classical nucleation theory of graphene growth from a hexagonal shape nucleation and the explanation of microscopic nucleation behavior as the nucleus size

increases.

1.2.3 Nucleation and growth dynamics of graphene

The typical growth of graphene is divided into three steps (Figure 1.13): 1) carbon-containing gas dehydrogenates and cracks on the substrate surface; 2) when the carbon atoms on the substrate surface reach a certain concentration, the nucleation process is triggered; 3) the nuclei grow further, and multiple nuclei fuse into continuous graphene layers. However, the orientation of the nuclei is originally derived from the arrangement of carbon clusters on the substrate surface in the early stage of graphene nucleation. More importantly, the nucleation barrier in process 2 determines the density of critical nuclei. In addition, the critical nucleus size and the nucleation barrier determine the reaction conditions and time required for nucleation. It is very important to have a deep understanding of the details of graphene nucleation on the substrate surface. Based on this, we can try to adjust the nucleation conditions and control the density of graphene grains to improve the quality of graphene synthesis in this dissertation.

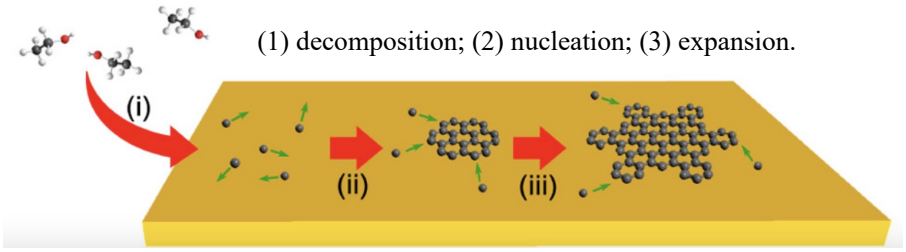

Figure 1.13 Schematic of the initial growth of graphene [48].

1.2.4 Mechanisms of graphene growth by chemical vapor deposition

In typical CVD processes, transition metal films are used as catalysts to facilitate the reaction of carbon precursors (such as methane) at approximately 1000°C, resulting in

graphene growth on the metal surface. Transition metal catalyst substrates play crucial roles in graphene growth, including acting as a flat template to support the growing graphene, decomposing raw materials, controlling the number of graphene layers, and aiding in defect repair [108–111]. Extensive studies have been conducted on graphene growth using various transition metal surfaces (such as Ni, Cu, Ru, Pd, Pt, Ir, Co, Au, Rh, and their alloys), revealing diverse growth behaviors. These differences arise from variations in the carbon solubility, carbon affinity, bulk diffusion, and surface diffusion characteristics of different metals [112]. During the thermal catalytic CVD process, graphene growth relies on the adsorption, dehydrogenation, and diffusion of carbon source molecules (such as methane) from the gas phase onto the metal surface (Figure 1.14). However, as the graphene film progressively covers the metal surface, the catalytic activity decreases significantly. This reduction occurs because the metal surface, once covered by graphene, can no longer effectively adsorb and decompose carbon source molecules. This phenomenon, known as catalyst poisoning, is a "self-limiting" effect [113] commonly mentioned during CVD on Cu substrates (Figure 1.14(a)). In contrast [114], on Ni and other transition metals, CVD growth of graphene occurs via bulk diffusion of carbon due to the high solubility of carbon and segregation during the cooling step (Figure 1.14(b)).

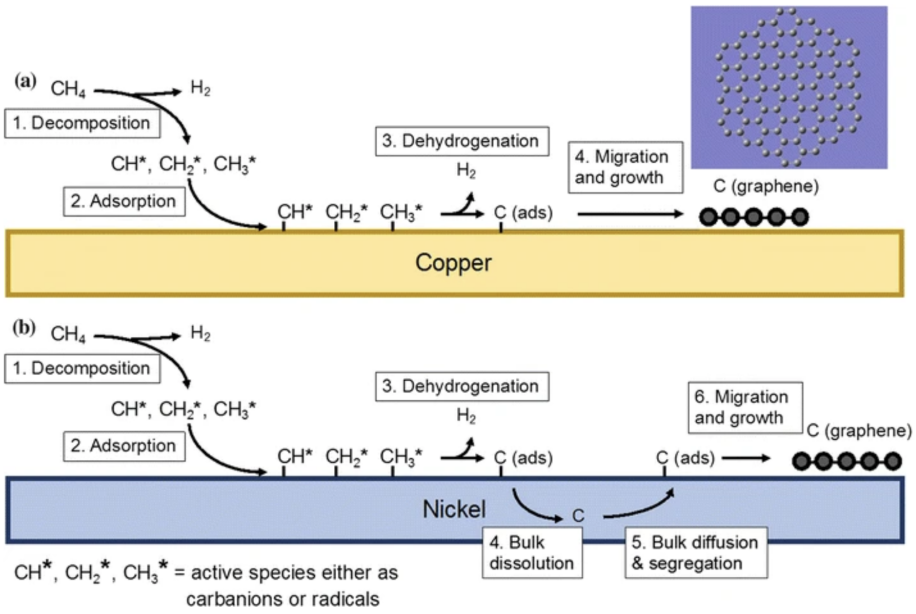

Figure 1.14 Growth kinetics of graphene produced by CVD on different catalysts: The case of CH_4 on Ni and Cu [115].

The mechanism of multilayer graphene growth on metal substrates involves the second layer nucleating and growing beneath the first layer, which is either adsorbed onto the metal surface or segregated within the bulk material. As discussed in Section 1.1.2, twisted graphene grown on Cu substrates exhibits a self-limiting behavior, leading to a structure where the first layer is consistently larger than the second layer (Figure 1.15(a)). To address the challenge of self-limitation and enable controlled top-down multilayer growth, researchers have developed various strategies and explored their underlying mechanisms. These include increasing the growth pressure, enhancing the supply of carbon precursors [116,117], and utilizing oxygen-containing carbon sources [118,119] to facilitate the growth of upper adhere graphene layers. One approach that has garnered significant attention is the use of ethanol as a growth precursor on Cu, which facilitates partial carbon substitution in the self-limiting graphene. This process aids in the nucleation of the second graphene layer, enabling the layer-by-layer growth of a large-

area graphene.

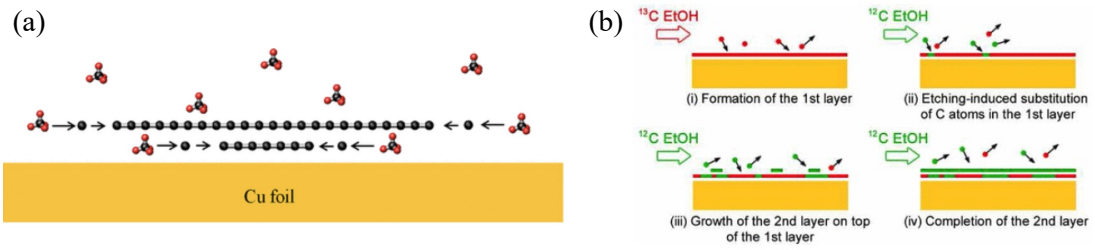

Figure 1.15 (a) Schematic of growth mechanism of the second graphene layer in the case of CH_4 on Cu [120]. (b) Schematic the layer-by-layer epitaxy mechanism for equilibrium BLG growth using ethanol as CVD precursor [118].

Recently, CVD technology has been applied to grow graphene directly on dielectric and semiconductor substrates without metal catalysts to avoid the presence of metal impurities during the manufacture of electronic devices. This also helps to avoid the transfer process of impurities and defects (introduced in 1.1.2). The direct CVD growth in oxygen-aided system is thought to involve a catalytic role played by the oxygen-rich substrate [121,122]. Researchers suggest that oxygen atoms present on the surface of the dielectric assist in facilitating the diffusion of hydrogen atoms away from the system, thereby enabling carbon atoms to remain on the surface and form graphene [122]. In the direct CVD process on catalyst-free surface [123], the growth of graphene on nonmetallic substrates relies on the formation and deposition of graphene nanoflakes (like cluster in classical nucleation theory) in the gas phase. The fate of these nanoflakes depends on their size: larger nanoflakes, with stronger adhesion, attach to the substrate and form stable structures, while smaller nanoflakes may leave due to thermal vibrations unless they bond with already stable nanoflakes. High temperatures, smooth substrates, and high precursor pressure facilitate the rapid formation and deposition of nanoflakes, promoting the preferential growth of SLG. Additionally, reorientation and alignment of the nm-sized flakes requires temperatures >2000 °C [124–126], resulting in disordered thin films.

1.2.5 Mechanism of graphene nucleation on graphene templates via ethanol CVD

The CVD technique using ethanol as the carbon source is a widely employed, cost-effective, and efficient method for graphene synthesis [127]. However, the mechanism by which ethanol promotes graphene nucleation remains unclear. Based on the nucleation mechanisms described in Section 1.2.2 and 1.2.4, a possible mechanism for metal-free CVD on a graphene template was proposed and its key steps were analyzed.

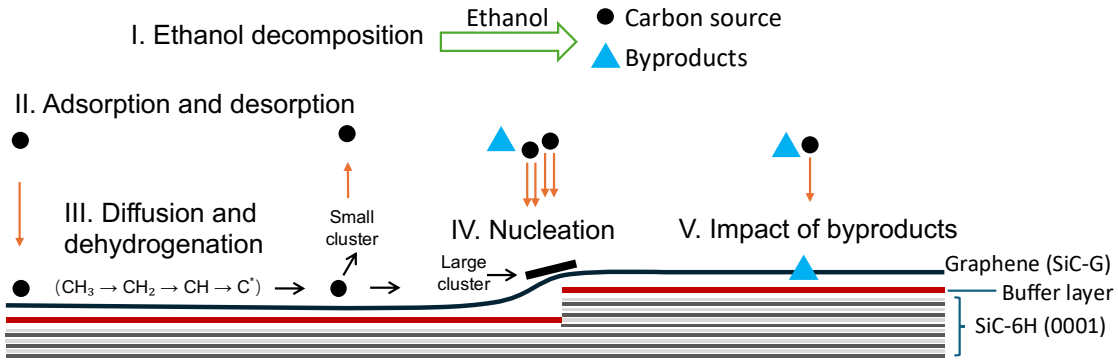

Figure 1.16 Schematic of nucleation mechanism for metal-free CVD on a graphene/SiC template

As shown in Figure 1.16, the mechanism of graphene growth on graphene templates involves five key steps as described below:

I. **Ethanol decomposition**

Under high-temperature conditions, ethanol (C_2H_5OH) undergoes thermal decomposition, yielding intermediates such as methyl (CH_3), ethylene (C_2H_4), acetylene (C_2H_2), and active carbon species (C*). Oxygen-rich byproducts, including water (H_2O), carbon monoxide (CO), and carbon dioxide (CO_2), are also formed [128]. These intermediates serve as abundant carbon sources for subsequent graphene growth.

In the low-temperature region (<800°C), CH_3 and C_2H_4 are the primary intermediates.

However, their low reactivity and limited decomposition kinetics result in an insufficient supply of active carbon, hindering graphene nucleation and growth. Conversely, in the high-temperature region (>1000°C), significant cleavage of C–C bonds occur, generating higher amounts of C_2H_2 and active carbon (C*), which promote efficient nucleation. Nevertheless, excessive byproduct formation at such temperatures may adversely affect the growth process.

II. Adsorption and desorption of carbon sources

The unique π-π conjugated structure of graphene templates allow selective adsorption of carbon-based intermediates, such as CH_3 or C_2H_4, primarily through van der Waals interactions at pristine regions and stronger chemical bonding at defect sites and edges. Adsorbed intermediates serve as precursors for graphene growth, undergoing further decomposition or desorption to release hydrogen (H_2) or oxygen-containing species. This dynamic balance between adsorption and desorption plays a critical role in governing the effective utilization of carbon sources [103,129,130].

Defects and regions under bending stress on the graphene template surface further influence this adsorption process. Defect sites, such as vacancies or grain boundaries, exhibit higher chemical reactivity due to unsaturated carbon bonds, which can strongly anchor carbon intermediates [131]. Similarly, areas under bending stress experience lattice distortion, resulting in altered electronic structures and localized high-energy sites that enhance the binding affinity for carbon precursors [132]. These stress-induced regions act as preferential adsorption zones, concentrating carbon sources and facilitating their activation.

III. Diffusion and dehydrogenation of carbon sources

Carbon-based intermediates, such as CH_3, C_2H_4, or C_2H_2, diffuse across the graphene template surface, driven by thermal energy and surface energy gradients. On an atomically smooth graphene surface, diffusion occurs with minimal energy barriers,

allowing intermediates to move freely and uniformly distribute. However, surface defects, such as vacancies, dislocations, or grain boundaries, disrupt the diffusion pathway by acting as energy wells. These defects trap intermediates, creating localized high-concentration zones that may lead to uneven growth. Similarly, areas under bending stress can create distorted lattice configurations, altering the diffusion dynamics and enhancing the likelihood of intermediate accumulation.

At elevated temperatures, dehydrogenation of carbon-based intermediates takes place, releasing hydrogen (H_2) and generating highly reactive carbon atoms (C*). These reactive carbon atoms possess high mobility and tend to aggregate at high-energy sites, such as defect regions or surface irregularities, where they are more likely to overcome the energy barriers associated with nucleation.

The balance between diffusion and dehydrogenation is critical for forming initial carbon clusters. Excessive dehydrogenation without sufficient diffusion can result in localized overgrowth or multilayer regions, while insufficient dehydrogenation limits the availability of active carbon for nucleation.

IV. Nucleation

The nucleation process on graphene templates is governed by a combination of thermodynamic and kinetic factors. The stability of nuclei is determined by the Gibbs free energy change (ΔG) of the system, which depends on the template surface energy, carbon cluster surface energy, and the binding energy between the clusters and the template. While graphene templates typically have low surface energy, defects or edge sites exhibit locally higher energy, facilitating carbon atom adsorption. Small carbon clusters with high surface energy are unstable and prone to desorption, whereas clusters reaching the critical size become stable as their surface energy decreases, allowing them to grow into nuclei by incorporating diffusing carbon atoms . The binding energy between the template and the clusters plays a pivotal role in overcoming the nucleation energy barrier. By

optimizing the template surface properties, such as introducing defects or doping, and adjusting growth conditions, it is possible to control nucleation density and grain size, thereby influencing the growth kinetics and crystal quality of graphene.

The randomness of nucleation orientation is mainly influenced by the distribution of defects, surface energy gradients, and growth conditions. Disordered or high-density defects disrupt the periodic symmetry of the template, creating complex local energy gradients that weaken the ordering of carbon cluster stacking, leading to randomly twisted structures. Specific defects, such as dopant atoms with strong adsorption capability or edge defects, can guide the arrangement of carbon clusters, reducing randomness and stabilizing low energy stacking configurations. Moreover, rapid deposition rates and low temperatures limit the time available for carbon clusters to diffuse and adjust their positions, further enhancing the randomness of orientation. These factors collectively determine the degree of order or randomness in nucleation orientation.

V. Impact of byproducts

Oxygen-containing byproducts from ethanol decomposition exhibit dual effects on graphene growth, primarily due to their interactions with carbon sources and the graphene surface [103].

On the one hand, oxygen groups alter the electronic environment of the graphene surface, increasing its chemical reactivity and creating localized high-energy sites. These sites facilitate the aggregation of carbon species, promoting the formation of initial carbon clusters. However, the orientation of these clusters during nucleation may exhibit randomness due to the absence of a dominant guiding mechanism. The distribution of nuclei and their twist angles is influenced by the substrate's energy landscape, where subtle variations in surface stress or defects can shift the balance toward specific orientations. While this randomness may reduce long-range crystalline order, it can also introduce diversity in the twist-angle-dependent electronic properties of the resulting

graphene layers.

Moreover, moderate amounts of oxygen groups can act as surface activators, playing a pivotal role in facilitating graphene growth. These groups interact with carbon-based intermediates (e.g., CH_3, C_2H_4, or C_2H_2) via chemical bonding or weak van der Waals forces, effectively lowering the energy barrier for carbon adsorption and nucleation. For example, hydroxyl groups may temporarily bond with carbon intermediates, stabilizing reactive species that decompose into active carbon (C*). This mechanism enhances the incorporation of carbon atoms into the growing graphene lattice, promoting efficient nucleation and growth [129].

On the other hand, oxygen species such as hydroxyl (–OH), carbonyl (C=O) groups and carbon dioxide (CO_2) can chemically react with the carbon lattice at the template graphene, particularly at pre-existing defect sites and regions under bending stress. These interactions are more pronounced where the lattice structure is distorted, as such areas exhibit higher chemical reactivity. This leads to edge etching, where oxygen breaks the C–C bonds and gradually removes carbon atoms from the lattice. Consequently, the structural continuity of the graphene film is compromised, and excessive etching disrupts the uniform growth of graphene layers. This selective interaction underscores the sensitivity of graphene growth to both surface conditions and the concentration of oxygen species, highlighting the importance of optimizing synthesis parameters.

By carefully controlling ethanol flow rates and reaction temperatures, the competing effects of oxygen species can be effectively balanced. Optimized conditions minimize the detrimental impacts of over-etching and defect formation while leveraging the activation properties of oxygen groups. This approach ensures efficient nucleation and controlled growth, leading to high-quality, uniform graphene films with tailored properties.

1.3 Motivation and challenges

In this study, we focus on randomly stacked twisted few-layer graphene (tFLG) because it has great advantages in the next generation of graphene-based devices. First, it is theoretically predicted to display a linear dispersion of electronic bands near the Fermi level due to weak interlayer coupling, which behaves similarly to massless fermions observed in monolayer graphene [5,133,134]. This unique band structure allows tFLG to exhibit electronic and optical properties comparable to those of monolayer graphene [135]. Second, the few-layer stacked structure effectively reduces the influence of charge impurities [136] and surface roughness [137,138] through a screening effect, offering a promising approach to mitigating the extreme sensitivity of the electronic band structure in monolayer graphene to environmental factors.

As introduced in Section 1.1.2, whether using the transfer SLG method or the CVD method for synthesizing twisted graphene on metal, the transfer process remains crucial for fabricating next-generation electronic devices incorporating large-area graphene. However, this process is costly, time-consuming, and susceptible to defects, which can degrade device performance. Therefore, this doctoral thesis focuses on introducing a method for directly growing twisted graphene using graphene templates via CVD, offering a novel approach to achieving transfer-free processes.

According to our previous research [139], twisted graphene has been successfully grown directly on fused quartz substrates with graphene templates via CVD, enabling the measurement of its electrical properties. In electrical transport analysis, tFLG demonstrates higher conductivity and carrier mobility compared to single-layer template graphene. However, in our earlier studies [140], the monolayer graphene templates were derived from Cu-CVD transfers, which introduced defect sites from annealing of polymer and unexpected wrinkles. These defects and transferred wrinkles cause carbon binding for 3D nucleation, increasing the local growth rate and forming island graphene, leading to non-uniformity in tFLG as the number of layers increases.

In this study, we proposed a novel growth method that eliminates the need for the conventional transfer process to achieve twisted graphene with high crystallinity and large domain sizes. Specifically, we utilized graphene/SiC templates for the direct growth of twisted graphene and focused on investigating its growth mechanism, including uniform nucleation and lateral growth. One of the key challenges in using graphene/SiC as a substrate lies in its inherently low surface energy, which makes it particularly difficult to grow graphene directly on non-metallic substrates or graphene templates. Unlike growth on metallic substrates, controlling the growth rate and nucleation density of graphene on monolayer graphene templates presents significant complexities [141]. Therefore, these challenges underscore the necessity for further research to deepen our understanding of the conditions and mechanisms that enable the direct CVD growth of twisted graphene on graphene templates.

1.4 Organization of the thesis

This thesis consists of seven chapters.

Chapter 1 begins by discussing the electronic structure of single-layer graphene, AB-stacked graphene, and twisted graphene, highlighting their properties directly tied to these structural variations. It then introduces the common synthesis methods and structural characterization techniques used for twisted graphene. To provide a foundation for understanding the growth behavior of twisted graphene on various graphene templates, the chapter delves into classical nucleation theory and growth kinetics as they relate to graphene nucleation and growth. Finally, it explores the nucleation mechanisms of graphene on different substrates, offering a comprehensive background for subsequent discussions.

Chapter 2 outlines the experimental setup and characterization methods used in this study. It begins by describing the sample preparation setup, including the design of the

infrared radiation furnace and gas flow system, which are key to synthesizing template graphene/SiC and twisted graphene. The chapter then introduces the characterization techniques employed, such as atomic force microscopy (AFM), scanning tunneling microscopy (STM), scanning electron microscopy (SEM), and Raman spectroscopy. The principles behind these methods are briefly explained, along with their specific applications in the experiments.

Chapter 3 begins by demonstrating the feasibility of synthesizing twisted graphene on graphene/SiC templates. The twisted structure and angle distribution of the resulting graphene are characterized using STM and AFM. Following this, the chapter investigates the temperature dependence of the growth process and examines the time dependence under optimized conditions across a wide temperature range of 900–1450°C. Based on these studies, a growth model for graphene on graphene/SiC templates is proposed, providing insights into the underlying mechanisms.

Chapter 4 builds on the findings of Chapter 3 and introduces a new approach to tackle the issue of high local nucleation density. In this method, both the synthesis of graphene/SiC templates and the subsequent CVD growth process are conducted within the same reaction chamber. This combined setup aims to enhance surface cleanliness and minimize nucleation density by eliminating the exposure of the intermediate product to air. By comparing the number and morphology of nuclei from AFM observation under the air-exposure (AirE) method and the continuous sequential thermal (ST) method, the superior ability of the ST process to suppress nucleation is demonstrated. Additionally, the chapter proposes a detailed nucleation mechanism for graphene growth on graphene templates using ethanol as the carbon source in the CVD process, offering deeper insights into the growth dynamics.

Chapter 5 presents a method for growing monolayer graphene on graphene/SiC using the ST process introduced in Chapter 4. This approach involves introducing CO_2 as an etchant to create controlled defects on the graphene/SiC surface, which act as nucleation

sites for subsequent CVD growth with a lower energy barrier. The samples are characterized before and after etching, as well as after CVD growth, using Atomic Force Microscopy (AFM), Scanning Electron Microscopy (SEM), and Raman spectroscopy. The impact of etching intensity is systematically investigated by varying parameters such as temperature, pressure, and etching duration. Finally, the specific mechanism of CO_2-assisted nucleation is elucidated, building on the growth model proposed in Chapter 4 to provide a deeper understanding of the process.

Chapter 6 serves as a supplement to the main dissertation, providing additional insights into the synthesis and properties of twisted graphene. First, it highlights the advantages of twisted graphene synthesized on graphene templates for electrical measurements, while showing the challenges of structural inhomogeneity associated with using Cu-CVD as a template. Then, comparative experiments demonstrate the superiority of layer-by-layer growth on graphene/SiC templates. Furthermore, this chapter presents experimental results showcasing the large-area lateral growth of twisted graphene achieved under the ST process, reinforcing its potential for scalable applications.

In the final chapter, a summary was provided of the previous six chapters, and a future perspective was offered based on the high crystallinity and the scalable layer-by-layer growth model of twisted graphene on graphene/SiC template.

Chapter 2. Experiments

2.1 Graphene synthesis: furnace, gas supply and exhaust system

An infrared radiation (IR) furnace equipped with a cold-wall heating system was utilized for ultra-high temperature treatments. Figure 2.1 presents both the external appearance and a schematic diagram of the furnace. The furnace used in this study is an SR1800G ultra-high temperature rapid thermal annealing device manufactured by Thermo Riko Co., Ltd. Infrared light emitted from the furnace's lamps is focused at the center of the sample by a transparent quartz spherical mirror, enabling the temperature to rise to a maximum of 1800 °C. A radiation thermometer (measurement range: 160–2000 °C, emissivity: 0.78) is employed to monitor the temperature during operation.

This setup, combined with the specifically designed gas supply and exhaust system, allows for dual functionality in this experiment: the epitaxial growth of graphene on SiC substrates and the CVD synthesis of twisted graphene. This versatility is achieved by precisely controlling the gas flow, pressure, and temperature, enabling the realization of both growth methods in a single system.

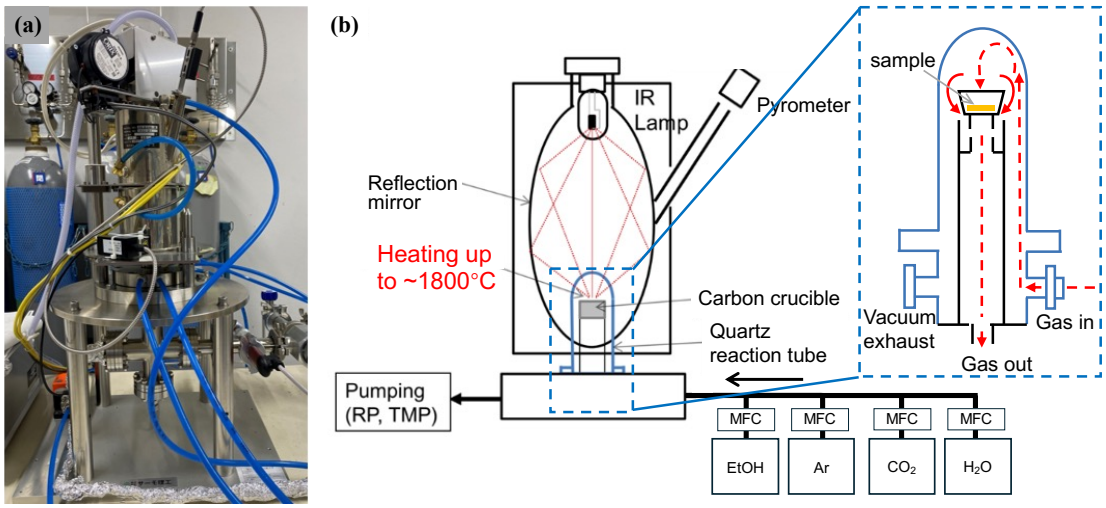

Figure 2.1 (a) Infrared radiation furnace. (b) Schematic diagram of internal structure in (a).

Figure 2.2 illustrates the designed and modified gas supply and exhaust system connected to the IR furnace. This system is designed to precisely control the flow of carrier and reactive gases during the high-temperature process. Initially, only the carrier gas flows through the furnace while the temperature increases. Once the target temperature is reached, the system switches to a mixture of the carbon source gas and carrier gas. This approach minimizes pressure fluctuations and ensures stable process conditions.

In this study, argon (Ar) was used as the carrier gas with a maximum flow rate of 700 standard cubic centimeters per minute (sccm). However, the mass flow controller (MFC) for Ar (MKS M-330H) has a maximum capacity of 100 sccm. To meet the requirements, additional Ar was supplied via an auxiliary electric furnace MFC, which can achieve a maximum flow rate of 1000 sccm (see Figure 2.2 for the gas supply system of the tubular electric furnace). Ethanol was used as the carbon source, with its MFC providing a maximum flow rate of 10 sccm.

The ethanol vaporizer, equipped with a mantle heater, was maintained at 40 °C to ensure stable vaporization. Ethanol vapor was delivered through piping sections heated to 50 °C to prevent condensation, with the temperature increasing further downstream. The MFC for ethanol was operated under a backpressure of approximately 18 kPa, corresponding to the saturated vapor pressure of ethanol at 40–50 °C, adjusted as needed based on the reaction pressure.

To support additional experimental designs, CO_2 and H_2O gas routes were integrated into the system. For the H_2O route, water vapor was generated using the gas supply system of a nearby electric furnace and mixed with the carrier gas before entering the IR furnace. To prevent condensation, the piping for the water vapor was heated to 80 °C, with the temperature increasing further downstream. This versatile setup allows for expanded

experimental capabilities tailored to the research requirements.

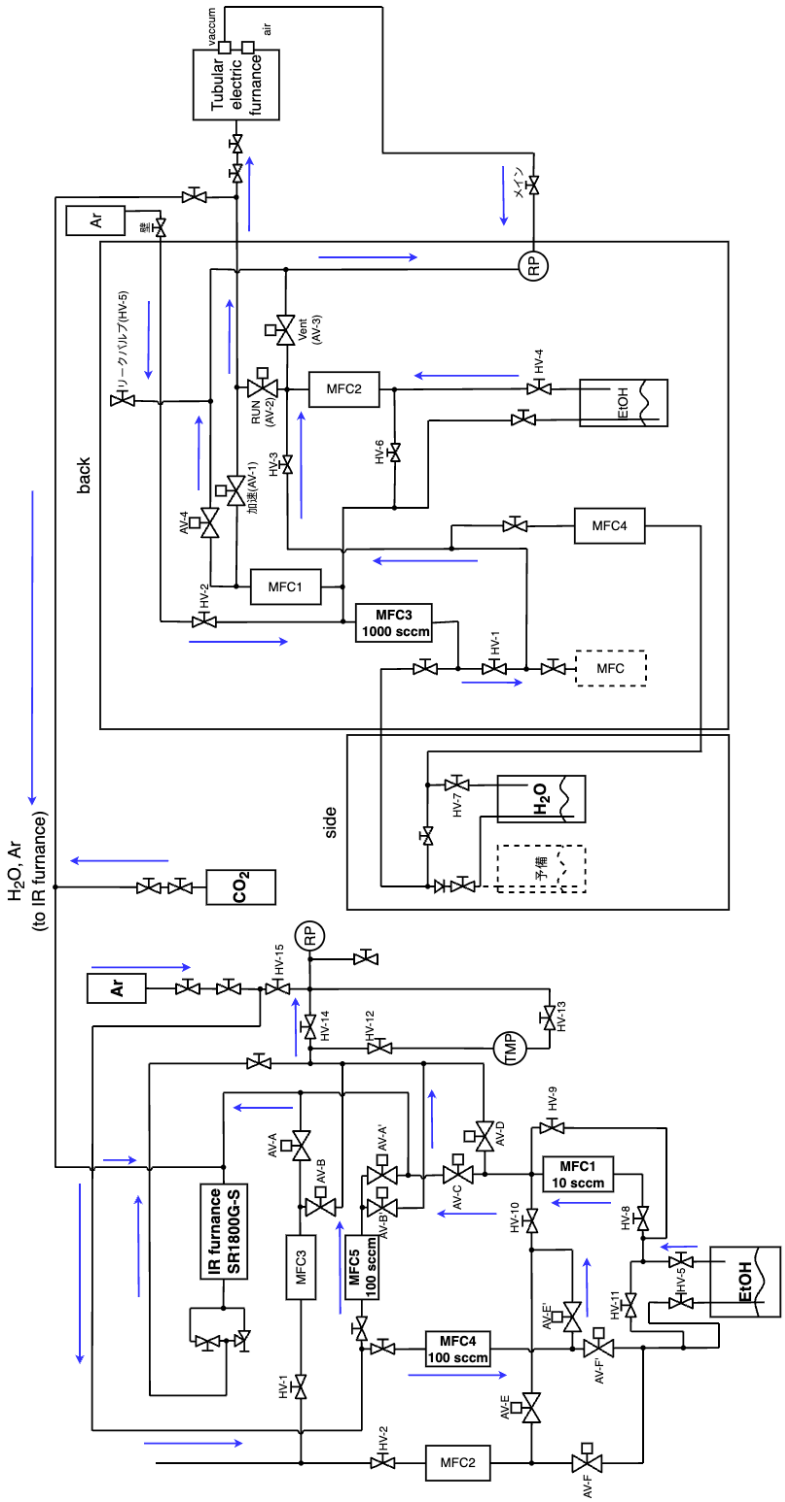

Figure 2.2 The diagram of gas lines of the gas supply and exhaust system connected to the IR furnace and the tubular electric furnace.

2.2 Characterization techniques

2.2.1 Atomic force microscopy

Atomic Force Microscopy (AFM) operates by scanning a sample surface with an ultra-fine cantilever, capturing detailed signals to construct a high-resolution image of the surface's topography. The key to AFM's functionality lies in the interaction between a sharp tip at the cantilever's end and the sample surface. When the tip approaches or touches the surface, forces such as van der Waals forces, electrostatic forces, and even chemical bonding forces come into play. These forces cause the cantilever to bend or deflect, an effect described by Hooke's law. The degree of deflection alters the path of a laser beam directed at the cantilever, changing the intensity of light reflected into a photodiode. This change in reflected light is measured with extreme precision, providing feedback to adjust the cantilever height dynamically (Figure 2.3(a)). By maintaining a constant interaction force or response signal, AFM maps the surface morphology with nanoscale accuracy.

The cantilever, typically tens to hundreds of microns in length and made from silicon or silicon nitride, is integral to this process. It carries a sharp probe tip (Figure 2.3(b)), often with a radius of curvature on the order of nanometers, allowing for precise interaction with the surface. The scanning process involves moving the cantilever in a raster pattern across the sample, enabling AFM to produce high-resolution three-dimensional images that reveal fine details of the surface structure.

AFM is particularly valuable in graphene research due to its ability to detect individual graphene flakes and provide nanoscale and atomic-level insights. With a resolution reaching sub-angstrom levels, AFM can distinguish single atomic layers on substrates with ease. It is also highly effective for characterizing the quality of thin films, including their morphology, roughness, uniformity, and defects. These capabilities make

AFM indispensable for understanding the properties of graphene and other two-dimensional materials.

In this experiment, AFM was utilized to analyze the lateral and vertical morphology, as well as the twist angle, of graphene samples. The HITACHI AFM5100N (Hitachi High-Tech, Japan) was operated in dynamic mode at room temperature (Figure 2.3(c)). This mode allows for non-contact or intermittent-contact scanning, minimizing damage to delicate surfaces while providing high-quality data. Both phase and topographic images were recorded simultaneously, offering complementary insights into surface properties. For each image, resolutions of 512 × 512 or 1024 × 1024 pixels were selected, with scan sizes ranging from 1000 nm to 10000 nm per side. These settings ensured sufficient detail for morphological analysis while maintaining a manageable data size. For even finer structural characterization and higher-resolution observations, Scanning Tunneling Microscopy was employed, as detailed in the following subsection.

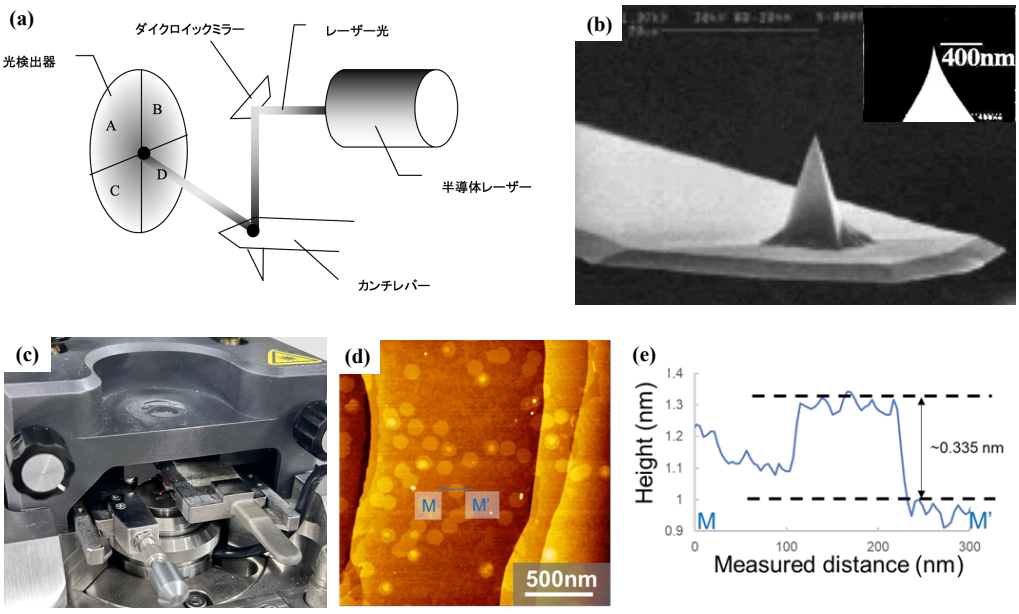

Figure 2.3 (a) Principle of AFM operation. (b) SEM image of the cantilever. (c) Work platform of the HITACHI AFM5100N for AFM measurement. (d, e) Typical AFM phase morphology and height profile of monolayer graphene sample.

2.2.2 Scanning tunneling microscopy

Scanning Tunneling Microscopy (STM) is a powerful technique within the family of scanning probe microscopies. It operates by detecting the quantum tunneling current between a sharp metallic probe tip and a sample surface (Figure 2.4(a)). This tunneling current, which occurs when the probe tip is brought within a few angstroms of the surface, is highly sensitive to the tip-to-sample distance. By measuring and controlling this current, STM can resolve surface features with atomic-scale precision, making it an indispensable tool for examining atomic-level surface fluctuations.

The probe tip is mounted on a piezoelectric ceramic tube, which precisely controls its position in three dimensions (x, y, and z). The scanning process is guided by two primary modes of operation: constant current mode and constant height mode, each offering unique insights into surface properties. 1) Constant current mode: In this mode, the tunneling current is maintained at a constant setpoint by a feedback circuit. To achieve this, the piezoelectric tube continuously adjusts the tip's height (z-direction) to compensate for surface height variations. The vertical movement of the tip reflects the topography of the surface. By mapping the z values across the x-y plane, a highly detailed three-dimensional height profile of the surface is generated. 2) Constant height mode: In this mode, the z-position of the probe tip remains fixed. Instead of adjusting the height, the variations in the tunneling current are recorded as the tip scans across the surface. These current fluctuations provide a two-dimensional map in the x-y plane, which can reveal electronic properties and local density of states.

For graphene, STM is particularly valuable due to its atomic resolution, which allows for detailed visualization of graphene's characteristic honeycomb lattice structure. In STM measurements, observing graphene's lattice and the moiré patterns in twisted bilayer graphene requires carefully optimized experimental conditions, including bias voltage

adjustments, tunneling current control, and ensuring a flat sample surface. STM detects the local density of electronic states (LDOS) on the surface by measuring the tunneling current between the probe and the sample. Since graphene exhibits low LDOS near the Fermi level, with electrons predominantly localized on carbon atoms, atomic spacing of 0.246 nm and electronic features at the K-point can be resolved. To achieve clear imaging, bias voltage should be tuned near the Dirac point to minimize background noise and enhance atomic-scale structural resolution. For twisted bilayer graphene, the relative rotation between two graphene layers induces periodic interference effects in atomic arrangement, forming moiré patterns. The period of these patterns is determined by the twist angle: smaller twist angles result in longer periods and prominent superlattice structures, while larger angles result in shorter periods that may become indistinguishable. Under these conditions, STM imaging not only reveals the geometric characteristics of moiré patterns but also reflects their unique LDOS distributions.

In this experiment, STM was employed to investigate the moiré patterns and graphene structures at high resolution. The equipment used included the Nanoscope IIIa scanning probe microscope (Digital Instruments, Santa Barbara, CA) and HITACHI AFM5100N (Hitachi High-Tech, Japan) (Figure 2.4(b)). Measurements were conducted at room temperature, operating in constant current mode. This mode was chosen for its ability to maintain a constant tunneling current by dynamically adjusting the probe's height, which provides a precise three-dimensional representation of surface morphology. Such precision is particularly advantageous for studying moiré patterns in twisted graphene, as these patterns often involve periodic height variations that are best captured through constant current mode. Additionally, this mode effectively accommodates the larger-scale height fluctuations of moiré patterns, minimizing distortion and enabling clear visualization of the periodic features (Figure 2.4(c), using Nanoscope IIIa system). By providing detailed topographical data, constant current mode ensures an accurate characterization of the moiré structures and their dependence on twist angles.

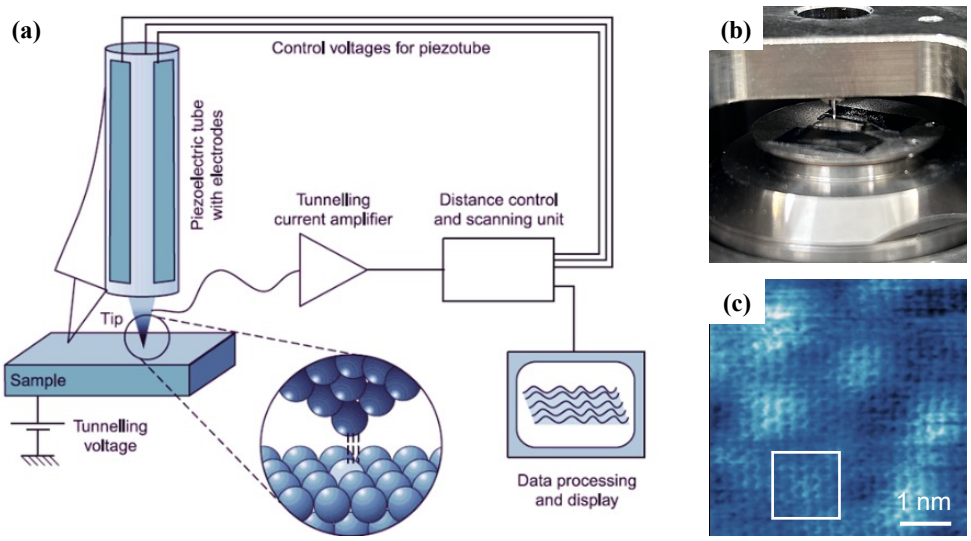

Figure 2.4 (a) Principle of STM operation. (b) Work platform of the HITACHI AFM5100N for STM measurement. (c) Typical STM image of tBLG graphene sample (I = 10 pA, V = -0.5 V).

2.2.3 Scanning electron microscopy

Scanning Electron Microscopy (SEM) is a versatile imaging technique that utilizes a focused beam of high-energy electrons to generate detailed surface information. As the electron beam interacts with the sample surface, it produces various signals, such as secondary electrons, backscattered electrons, and characteristic X-rays, which are collected to form an image (Figure 2.5(a)). The most commonly used signal for imaging is secondary electrons, which provide high-resolution details of the surface morphology. The ability of SEM to achieve nanoscale resolution makes it suitable for characterizing two-dimensional materials like graphene.

In the context of graphene, SEM leverages contrast differences in secondary electron yields, which arise from interactions between the graphene layer and the substrate, enabling the observation of features such as monolayers, defects, and surface uniformity. On metallic substrates (Figure 2.5(b)), the contrast arises primarily from differences in

secondary electron yields between graphene-covered and uncovered regions, often influenced by oxidation. On insulating substrates, graphene's conductive nature modifies the charging behavior of the substrate, resulting in a bright secondary electron image due to electron-beam-induced currents (EBIC) and charge redistribution. These mechanisms enable the clear visualization of graphene, even though graphene itself contributes relatively little to the secondary electron signal.

In this experiment, the S-4800 SEM (Hitachi) was employed to verify the presence and distribution of graphene on the substrate (Figure 2.5(c)). Imaging was conducted using low-energy primary electrons (typically around 0.5–1.5 keV) to optimize contrast while minimizing sample damage. Secondary electron imaging was used to differentiate graphene layers, taking advantage of the strong contrast generated by their interactions with the substrate. The choice of electron energy was critical for enhancing visibility, particularly for monolayer graphene, whose transparency to secondary electrons allows for accurate identification. This approach provided a rapid and reliable method for graphene characterization, serving as an essential precursor to further high-resolution analyses with techniques such as AFM and STM.

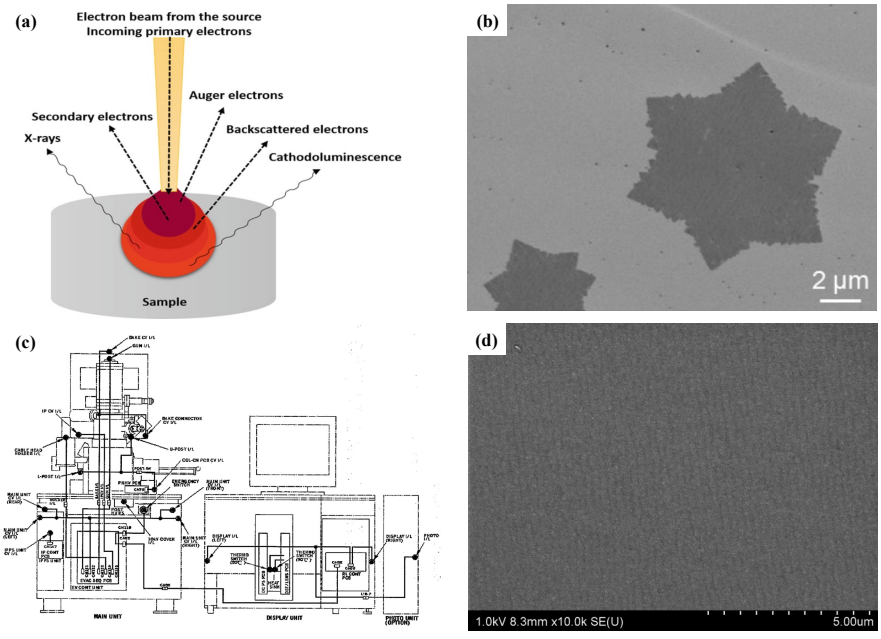

Figure 2.5 (a) Schematic representation of various signals for SEM imaging [142]. (b) Typical SEM patterns of monolayer graphene on Cu surface [143]. (c) Schematic instruments of S-4800 SEM. (d) Typical SEM image of graphene/SiC sample.

2.2.4 Raman spectroscopy

Raman spectroscopy is an analytical technique that relies on the inelastic scattering of light, where a small portion of the scattered light experiences a shift in energy corresponding to molecular vibrations, rotations, or electronic transitions (Figure 2.6(a)). This energy shift, known as the Raman shift (cm^{-1}), provides a molecular fingerprint of the sample. A Raman spectrum, which plots the intensity of scattered light against the Raman shift, is used to interpret the material's structural and chemical properties (Figure 2.6(b)).

For twisted graphene, Raman spectroscopy is an exceptionally sensitive tool for characterizing sp^2 nanocarbon materials. It provides critical insights into layer crystallinity, interlayer interactions, and strain effects. The technique is particularly effective for identifying graphene's characteristic vibrational modes, such as the G-band (arising from in-plane stretching of sp^2 carbon atoms) and the 2D-band (a second-order overtone linked to double-resonance scattering processes). Additionally, Raman spectroscopy is sensitive to twist angle effects, which manifest as changes in the 2D-band shape and position due to electronic structure rearrangements caused by interlayer interactions in twisted graphene systems.

In this experiment, Raman spectroscopy was employed to evaluate the crystallinity and quality of grown graphene layers at room temperature, with the detector cooled to -70°C for enhanced sensitivity. Measurements were conducted using a HORIBA LabRAM HR-800 micro-laser Raman spectrometer with a 532 nm laser excitation and a 100× objective lens (spot diameter: ~1 μm) (Figure 2.5(c)). For graphene suspended on a

graphene/Cu template, the laser power was carefully maintained at 0.2 mW to prevent damage to the fragile graphene layer. In contrast, for graphene on a SiC substrate, the laser power was increased to 48–60 mW due to the enhanced thermal conductivity provided by the substrate. The elevated power improved the detection of graphene against the stronger SiC substrate peaks, enabling precise characterization of graphene layers and their structural features.

Additionally, to characterize the graphene's feature spectra, normalization and substrate subtraction were performed on the SiC substrate during the analysis. The spectrum of monolayer graphene on SiC, after substrate subtraction, is shown in Figure 2.6(d). Since a monolayer graphene template was obtained via thermal decomposition on a 6H-SiC (0001) substrate, buffer layer/graphene peak deconvolution was also carried out in the Raman spectroscopy analysis. The detailed analysis process can be found in the Appendix: Raman Spectroscopy of Graphene Synthesized on SiC (0001).

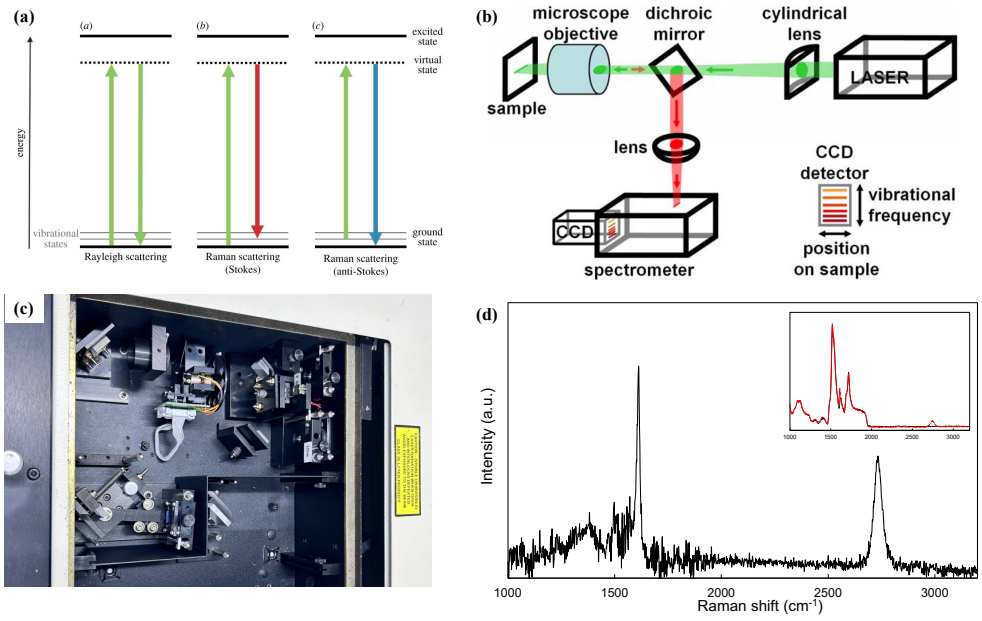

Figure 2.6 (a) Rayleigh scattering and Raman scattering [144]. (b) Schematic presentation of typical Raman spectroscopy instrument [145]. (c) Image of Raman microscopy spectrum. (d) Typical Raman spectrum of graphene/SiC sample with D (~1350 cm^{-1}), G

(~1600 cm^{-1}), and G′ bands (~2700 cm^{-1}). The spectrum is the result after subtraction of SiC substrate peaks and normalization. The noise signal near the G-band originates from the presence of the SiC (0001) buffer layer between the epitaxial graphene and SiC [146]. The inset shows the original SiC spectrum (black line) and the graphene/SiC spectrum (red line).

Chapter 3. Scanning probe analysis of twisted graphene grown on a graphene/SiC template

3.1 Background

Twisted few-layer graphene (tFLG) has gained significant attention for its unconventional electrical properties [38], including superconductivity and Mott-like insulating behavior at a small twist angle of 1.1° [8,147,148]. Common methods to fabricate tFLG include multiple transfer methods [77,79] of monolayer graphene prepared by a mechanical exfoliation method [1] and Cu-CVD [53]. Unfortunately, transfer methods are not suitable for the scalable synthesis of tFLG, and the Cu-CVD method has difficulty fabricating graphene with more than two layers [114].

Epitaxial graphene growth on SiC substrates offers a promising route for wafer-scale FLG synthesis [60,61]. This process involves high-temperature annealing of the SiC substrate in an ultrahigh vacuum or argon atmosphere, during which silicon atoms are sublimed, leaving carbon atoms to form FLG. Therefore, the stacking structures and surface morphologies of the epitaxial graphene layers strongly depend on the Si- and C-terminated faces of the SiC substrate [59]. For the Si-terminated face, uniform FLG with a stable order stacking (i.e., AB and ABC stacking) is preferentially formed [62,64,65]. On the other hand, for the C-terminated face, thicker multilayer graphene with a random stacking like a turbostratic structure is formed [30]. However, the surface morphology of multilayer graphene is very rough due to the high decomposition rate of the C-face [149]. Thus, the growth technique utilized for graphene formation from SiC is not suitable to synthesize highly crystalline tFLG.

To fabricate tFLG via the CVD process, growing additional graphene layers on template graphene is a promising strategy [150–152]. In this vapor-solid growth process, a graphene layer with random stacking should be formed preferentially because it is difficult to rotate the grown graphene layer in a solid environment [53]. Previously [140], we reported that FLG is synthesized by overlayer growth of graphene on a Cu-CVD

monolayer graphene template using the CVD method. We found that a moiré pattern appears in the lattice structure of a grown graphene 2D island by the scanning transmission electron microscopy (STEM) images, indicating that the twist angle between the grown graphene and template graphene differs from that of the order stacking [139]. However, when Cu-CVD monolayer graphene is used as the solid template, macrostructures such as wrinkles and defects produced in the transfer process have an adverse effect on the vapor-solid growth process [153], degrading the uniformity and crystallinity of the grown multilayer graphene.

In this study, we directly grow tFLG via the metal-free CVD method on an atomically flat epitaxial graphene/SiC substrate, serving as a solid template. The SiC substrate's Si-terminated face is utilized for this purpose. After determining the local twist angle, we investigate the temperature dependence of the broader surface morphology and crystal structure of graphene islands grown on the epitaxial graphene template to elucidate the growth mechanism of tFLG.

3.2 Experiment design

As shown in Figure 3.1, the epitaxial graphene/SiC (SiC-G) used as a solid template was prepared by the sublimation method in an argon atmosphere, as previously reported [154,155]. Typically, SiC substrates are annealed around 1600–1750 ºC in Ar at a pressure of 10–40 kPa. We confirmed the formation of continuous epitaxial monolayer graphene with a low density of defects on SiC substrates by Raman spectroscopy and STM at room temperature under atmospheric conditions. Graphene overlayer growth via CVD was carried out in infrared heating furnace at high temperature (900–1450 ºC) with ethanol as a carbon feedstock in an argon carrier gas (Figure 3.1). Graphene layers were deposited by flowing a mixture of ethanol/argon (1 sccm/700 sccm) for 10 minutes with a pressure below 10 kPa. In some experiments, shorter processing times of 1.5 and 3 minutes were

attempted to elucidate the initial growth mechanism at elevated temperature (1450 ºC). The CVD grown graphene (CVD-G) on SiC-G were characterized using AFM, Raman spectroscopy, and STM with the same condition as SiC-G. Generally, silicon in the SiC substrate should hardly sublimate through the grown graphene layer even at the ultrahigh temperatures in this experiment since the silicon atom diameter and the free space in the graphene lattice are extremely close [156]. Accordingly, epitaxial SiC-G was utilized as a stable template for CVD growth at ultrahigh temperatures. However, the reactive environment caused by the decomposition of the carbon feedstock for the graphene growth may influence the stability, as discussed in detail in the next section.

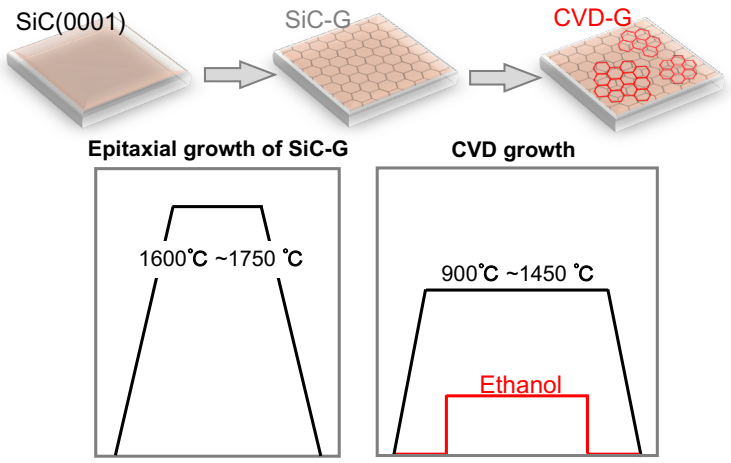

Figure 3.1 Schematic diagram for epitaxial growth of SiC-G and CVD-G growth.

We confirmed the formation of continuous epitaxial monolayer graphene with a low density of defects on SiC substrates by Raman spectroscopy and STM at room temperature under atmospheric conditions. Raman spectroscopy was carried out at room temperature using laser excitation of 532 nm with a ×100 objective lens (typical spot diameter ~1 μm). The laser power was kept at a constant value of 7 mW. The AFM and STM measurements were acquired by a HITACHI AFM5100N (Hitachi High-Tech, Japan) and a Nanoscope IIIa scanning probe microscope (Digital Instruments, Santa

Barbara, CA). The AFM observations were conducted in the dynamic force mode under atmospheric conditions at room temperature. Only the representative data of AFM images, which are important for the analysis and discussions, are selectively exhibited in this paper, although we observed AFM images from various samples grown under a variety of conditions. The STM observations were performed with a sample bias voltage of –500 mV and a tunneling current of 10 pA under the constant current mode. In this study, monolayers graphene areas with a more stable electronic state are selectively observed in the STM measurements to achieve accurate analysis of periodic moiré patterns.

3.3 Structure analysis of twisted graphene

3.3.1 Structural characterization of twisted graphene

Figure 3.2 shows the morphology of the sample surface before (Figure 3.2(a)) and after (Figure 3.2(c)) CVD growth at 1400 ºC observed by STM with a high resolution and the Raman spectra from these samples. As shown in the enlarged image in the upper right corner of Figure 3.2(b), a hexagonal lattice is clearly observed from the sample before the CVD process. This honeycomb structure corresponds to the typical atom-scale image observed from monolayer graphene [157], where the green and red spots represent two kinds of carbon atoms in the unit cell. Therefore, the SiC samples used in this study are uniformly covered with high-quality monolayer graphene before CVD treatment, which is used as the growth template.

After the CVD treatment, the grown graphene islands are observed clearly by STM, as shown in Figure 3.2(c). The step height of the island in the cross section along line L-L' approximately corresponds to the monolayer height. The atomic-resolution image in the inset also exhibits a honeycomb lattice structure, causing the moiré pattern induced by the twisted structure between the grown graphene layer and the monolayer graphene template layer, as shown in Figure 3.2(d). The green dots indicate the periodicity of the

moiré pattern as a superlattice structure. According to the geometric calculation analysis of equation (1.1) in Section 1.1.3, the twist angle θ is related to the periodicity length D, where a is the lattice constant of graphene (~0.246 nm). From the periodicity of the moiré pattern (D = 1.72 nm) observed in the STM image (Figure 3.2(d)), the estimated twist angle of this sample is θ = 8.2º. Figure 3.2(e) is the Raman spectra obtained from the samples before and after CVD treatment. In these Raman spectra, the signals from the SiC substrate are subtracted as the background spectra. After the CVD treatment, the appearance of D-band and the G'-band shifts to a higher frequency, possibly caused by the additional graphene layer and/or island formation. Notably, the G-band intensity increases, as observed after distinguishing the buffer layer peak (Table A1) [146]. The relative increase in G-band intensity is considered supporting evidence for the lateral growth of CVD graphene.

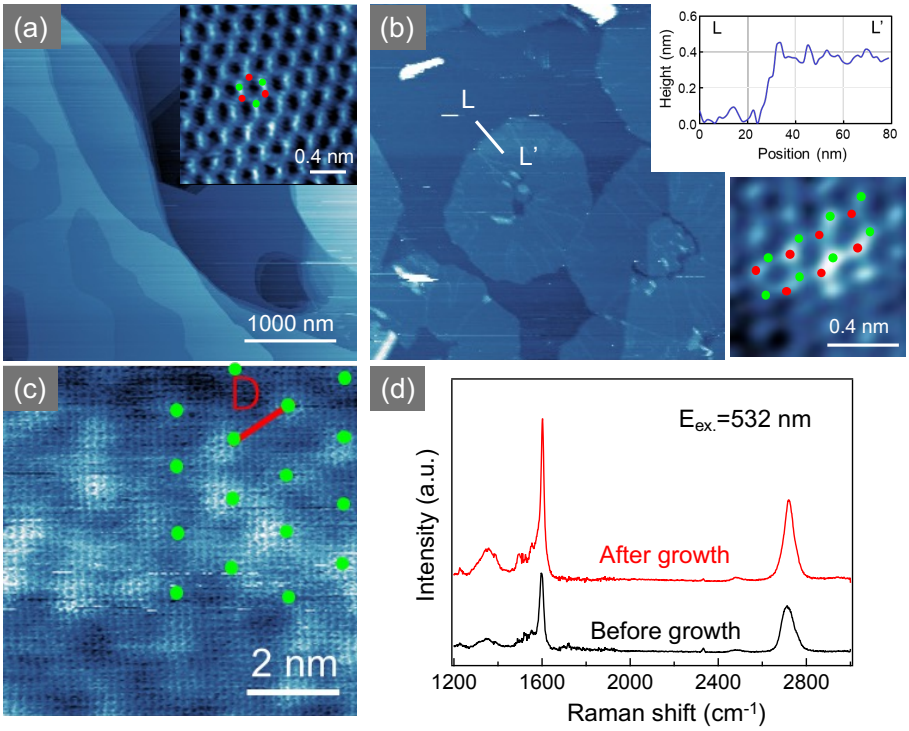

Figure 3.2 STM images observed from (a, b) the epitaxial monolayer graphene on the SiC substrate and (c) the graphene islands grown via the CVD process. Cross-sectional profile along L-L' in the STM image (c) is also shown to evaluate the height difference. (d)

Magnified STM image (I = 10 pA, V_{bias} = -0.5 V) of (c) to observe the moiré patterns. (e) Raman spectra observed from the samples in (a) and (c) with 532 nm laser excitation. Several spectra obtained from different measurement spots with diameters about 1 μm are averaged. All these spectra are the results after the subtraction of the SiC substrate peaks and normalization.

Figure 3.3(a) shows the AFM images of the sample surface after CVD growth at 1300 ºC . By measuring the straight edges of the grown monolayer graphene with a single-crystal structure and if the epitaxial graphene template on the SiC substrate corresponds to the observed region, we directly identified the twist angle of the grown graphene. The hexagonal depressions formed by the sublimation of silicon atoms during buffer layer generation were used to determine the orientation of the template monolayer graphene (highlighted as the black hexagon in the upper-right corner of Figure 3.3(a). As shown in Figure 3.3(b), the twist angle between the template graphene and the SiC substrate, obtained through thermal decomposition, is 30°. Therefore, the twist angle θ between each CVD-grown hexagonal graphene domain and the template graphene is correctly calculated as the orientation angle between the SiC substrate and the CVD-grown graphene domain, minus 30°. Figures 3.3(c) and (d) provide examples illustrating the method of angle measurement, including cases for 0° and 30°.

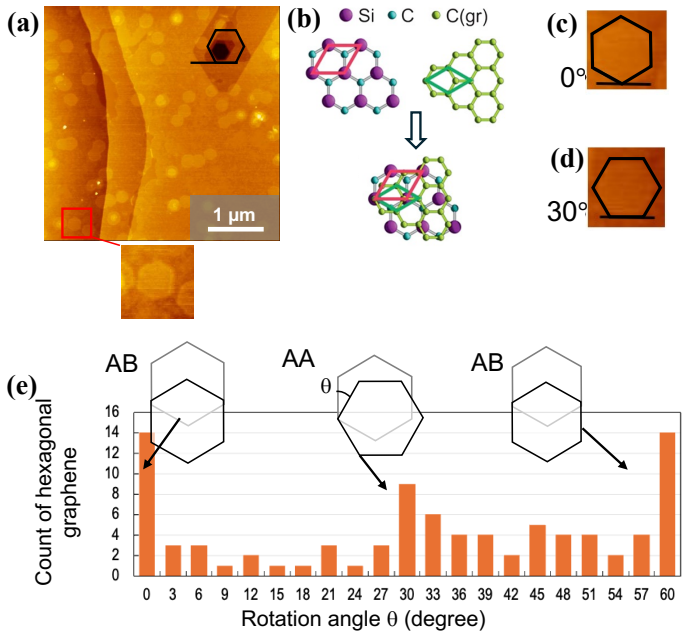

Figure 3.3 (a) Morphology of CVD grown graphene on SiC/graphene substrate. (b) A schematic diagram illustrating the template graphene obtained through thermal decomposition, the SiC substrate, and the twist angle between them. c, d) Two zoomed-in images of (a) highlight the hexagonal graphene islands and provide examples of twisted angle measurements. (e) Histogram showing the angular distribution, based on measurements from 75 randomly selected hexagonal islands.

The angle analysis performed using AFM enables the determination of the twist angle distribution in the grown graphene. Compared to the STM method, this approach significantly reduces the workload involved in measurement and analysis. Figure 3.3(e) presents a histogram of twist angles, which encompasses all hexagonal graphene islands shown in Figure 3.3(a). A total of 75 hexagonal islands were analyzed. A broad distribution of twist angles and a high random stacking ratio of 82% at 1300 °C were achieved.

This result aligns well with findings for bilayer Cu-CVD graphene [53,158]. Although bilayer Cu-CVD graphene is described as following a bottom-up growth

mechanism, in contrast to the overlayer growth model on a graphene template, Sun et al. [159] highlighted that the high ratio of twisted nucleation of second layer is influenced by local environmental variations and "gas-flow perturbation" near the nucleation sites. These two insights are attributed to the increased local nucleation rate, which is crucial for understanding the growth of twisted graphene structures.

3.3.2 Causes of random stacking

During the rapid nucleation process of graphene, the high occurrence of random twisted stacking can be explained from both thermodynamic and kinetic perspectives. According to thermodynamic principles, nuclei in the metastable state have a certain probability of overcoming the energy barrier via thermal fluctuations to transition into the most stable AB-stacked structure [106] (Figure 3.4). A system naturally evolves toward the most stable equilibrium state over time. However, in practical rapid nucleation processes, the system often remains in a metastable state rather than reaching the absolute energy minimum. This metastable state occurs because the system does not have enough energy in a short time to overcome the energy barriers, trapping it in a local minimum [160].

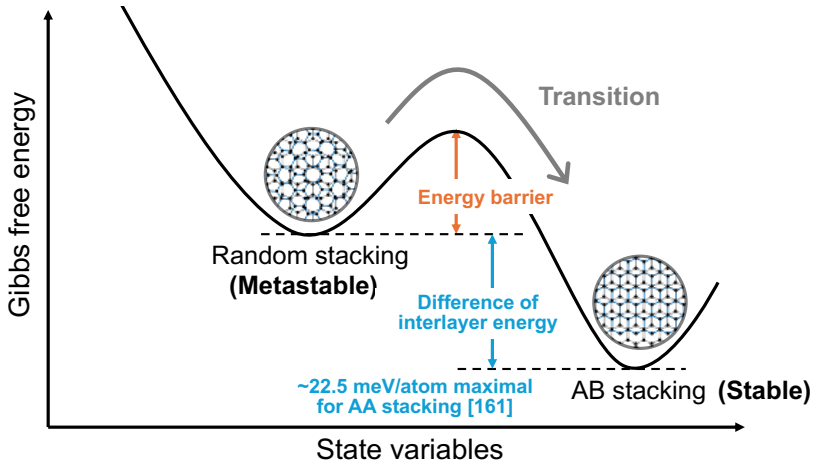

Figure 3.4 Gibbs free energy of random stacking in metastable state and AB stacking in stable state.

Theoretical calculations on bilayer graphene indicate that the interlayer energy in the stacked structure is minimal (most stable) for AB (BA) stacking, and maximal for AA stacking. The difference of interlayer energy between AB and AA stacking is typically in range of 10–30 meV/atom [161,162].

For a twisted structure, lattice structure locally resembles the regular stacking such as AA, AB, BA, or saddle point (SP), depending on the position. The graphene lattice deforms to increase the AB (BA) stacking region and decrease the AA stacking region depending on the location. We assume that the initial graphene nanoflakes adsorb onto the template graphene, forming a random twisted stacking. Subsequently, a twist-to-AB transition occurs. This process is often accompanied by multiple intermediate states and corresponding energy barriers (E_{b1}, E_{b2}, ..., E_{bx}), with the time required for each state gradually increasing [160]. Therefore, if the system does not have enough energy to overcome the energy barrier in a short period of time, it will be trapped in a metastable state.

Theoretically, the energy barrier for transition from a twisted state to an AB-stacked state increases with graphene size, leading to a higher temperature for phase transition. For example, in a rhombic graphene nanoflake with a side length of 1.9 nm and a twist angle of 7.34° (corresponding to one moiré period), the energy barrier is 0.052 eV, with an activation temperature of 150 K. In contrast, for a 7.6 nm nanoflake at the same twist angle (corresponding to four moiré periods), the energy barrier increases to 0.36–0.74 eV, requiring an activation temperature of 600 K [160].

Therefore, in the scenario of CVD growth, the initial nuclei of graphene form rapidly and remain in a random metastable state. As a few nuclei overcome the energy barrier via thermal fluctuations, others that fail to do so face an increasing energy barrier as their size grows. Consequently, the probability of overcoming the barrier gradually decreases,

ultimately preventing the system from reaching the most stable AB-stacked configuration (Figure 3.5).

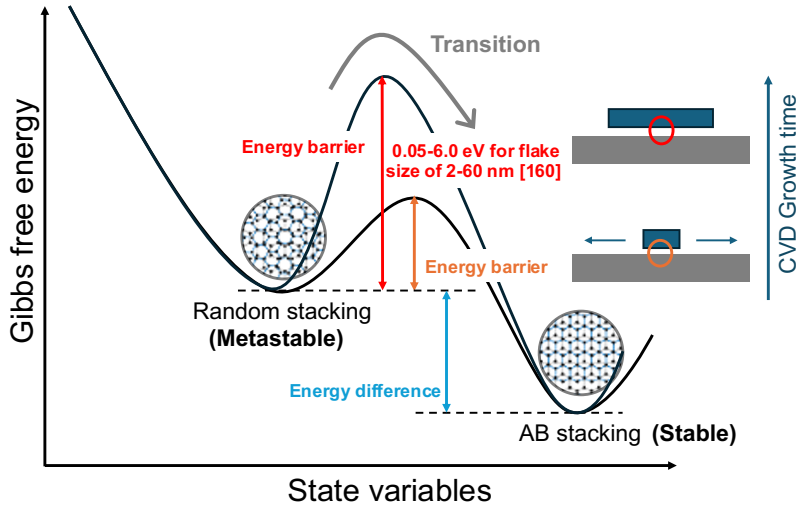

Figure 3.5 Energy barrier of metastable-to-stable transition in the growth scenario.

The **primary reasons** for the high randomness in layer stacking can thus be summarized as follows:

a) **Kinetic constraints during rapid nucleation**: The limited time available for carbon atom rearrangement inhibits the formation of a stable AB-stacked structure.

b) **Existence of energy barriers**: Existence of energy barriers: The transition from a randomly twisted stacking to AB stacking requires overcoming a certain energy barrier. The energy barrier increases as the graphene size grows. However, due to the rapid growth process, neither sufficient time nor increasing energy input is available to complete this transition.

c) **Instability of the template morphology**: Additionally, when ethanol is used as a carbon source for graphene growth on a graphene/SiC (SiC-G) template, the instability of the template morphology must also be considered as a factor affecting nucleation. As shown in Figure 3.6, graphene grown at SiC step edges experiences local strain, and reactions between ethanol byproducts and the SiC-G induce the

formation of defects and excessive dangling bonds. These regions exhibit higher adsorption energies, increasing the local density of carbon precursor (green-circle regions) and accelerating the growth rate. Therefore, the instability of the template morphology serves as an additional contributing factor to the high random stacking rate.

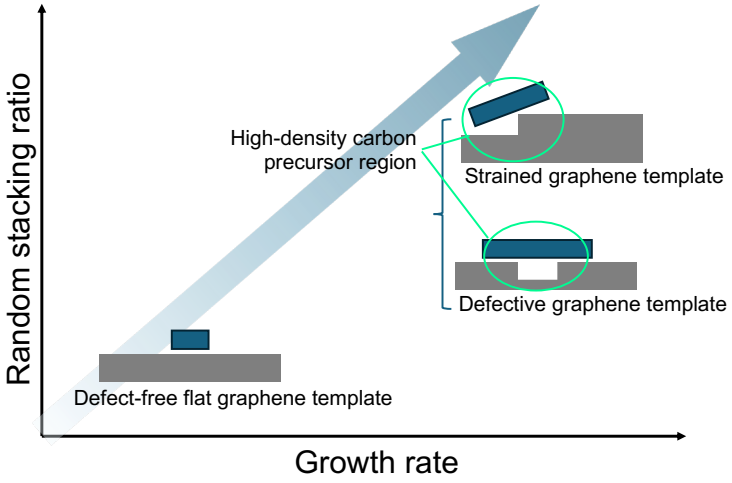

Figure 3.6 The relationship between growth rate and random stacking ratio in the instable template morphology scenario.

3.4 Effect of temperature on twisted graphene

3.4.1 Characterization of twisted graphene in different temperatures

Figure 3.7 compares the AFM images of the graphene islands grown on an epitaxial graphene/SiC at 900 ºC, 1200 ºC and 1300 ºC. For a growth temperature of 900 ºC, protruding structures with a non-uniform shape are slightly deposited on the surface. As indicated by the height profile along the L-L' line in Figure 3.7(a), the structure height is much higher than the step height (0.335 nm) of monolayer graphene. At 1200 ºC, additional protruding structures with non-uniform shape lower than the monolayer step height appeared. The relatively small coverage and irregular shape means that the structures may be the amorphous-like agglomerations of carbon. Although the primary

study did not further characterize the structure of the suspected amorphous carbon, a methodological approach involving multiple techniques can effectively reveal its structure and composition. STM and scanning tunneling spectroscopy (STS) are particularly useful for investigating its microstructure and electronic density of states. STM enables direct observation of surface morphology, allowing the evaluation of localized ordering or characteristic structures, such as graphene-like fragments. STS provides detailed electronic information, helping to assess properties such as bandgap and conductivity. Additionally, X-ray photoelectron spectroscopy (XPS) serves as a pivotal technique for analyzing the chemical composition and bonding states of amorphous carbon. Through XPS, the relative contributions of sp^2 and sp^3 carbon-carbon bonds can be quantified, alongside the identification of possible oxidation states or impurities. These insights, when integrated with other techniques, not only verify the amorphous nature of the sample but also provide a comprehensive understanding of its structural complexity and intrinsic properties.

The growth behavior completely differs for a growth temperature of 1300 ºC. Many islands with a hexagonal shape are observed on the epitaxial SiC-G as the solid template. The height of the islands is equivalent to the step height of monolayer graphene, as indicated by the height profile along the M-M' line in Figure 3.7(b). This means that the grown graphene islands are constructed by a monolayer graphene sheet. The hexagonal shape of the grown graphene islands implies that the island is composed of a single crystal terminated by the zigzag or armchair edges, reflecting the growth rate difference between these edge structures. The atomically flat terrace structure of the grown islands indicates that highly oriented 2D islands are expanded via lateral growth after nucleation. This means that highly crystalline bilayer graphene is successfully formed via the vapor-solid growth process.

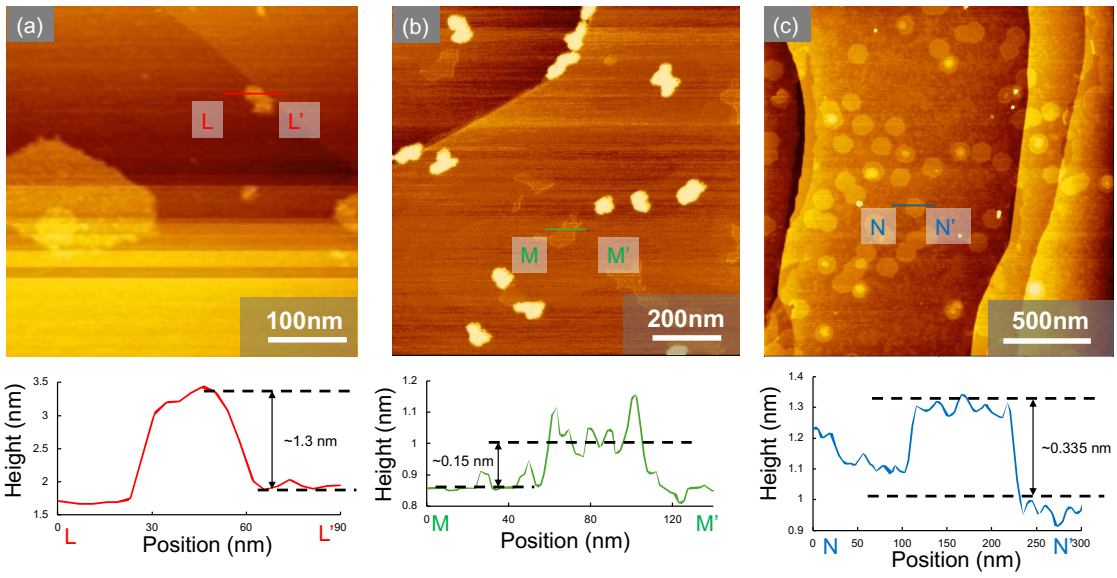

Figure 3.7 AFM images observed from the samples after the CVD process on epitaxial SiC-G substrates at (a) 900 ºC, (b) 1200 ºC and (c) 1300 ºC. Cross-sectional profiles along the L-L', M-M' and N-N' lines are also shown in the lower part of the AFM images.

The height distribution of the grown graphene islands significantly depends on the growth temperature. Figure 3.8(a) shows the analyzed result. The interval of the histogram is 0.35 nm, which is the step height of monolayer graphene. A height less than 0.35 nm corresponds to the small amorphous-like carbon clusters. The broken lines in the histogram are drawn to guide the eye. At lower growth temperatures of 900 ºC and 1200 ºC, the heights of the grown graphene islands show a broad distribution. The heights of the graphene islands grown in the lower temperature range cannot be specified as an integer multiple of the step height of the monolayer graphene, although the height indicated in Figure 3.8(a) is a multiple of 0.35 nm for convenience of the distribution comparison. The grown graphene islands form an amorphous-like carbon cluster without a flat terrace structure. On the other hand, for a growth temperature above 1300 ºC, few-layer graphene islands with a flat terrace structure are observed, and their heights can be specified by an integer multiple of the step height of monolayer graphene. In particularly,

it is noteworthy that the proportion of monolayer graphene corresponding to ~0.35 nm is very high for a growth temperature of 1300 ºC. For a growth temperature of 1400 ºC or above, few-layer islands consisting of 2–3 graphene layers are formed predominantly.

Figure 3.8(b) shows the growth temperature dependence of the average value of the island radius. In this analysis, we evaluated the size of the island radius from the AFM images by assuming that the island has a circular shape. We used samples only in the initial growth stage, where the coverage of the growth layer is less than 0.53. Thus, the distance between the nucleation sites on the samples used in this analysis is sufficient to prevent lateral growth from conflicting and coalescing with adjacent islands. As shown in Figure 3.8(b), the size of the grown graphene islands expands as the growth temperature increases. Considering the results of both Figure 3.8(a) and (b), we can conclude that the process temperature at 1300 ℃ is an optimized growth condition for graphene islands with a monolayer structure and uniform size.

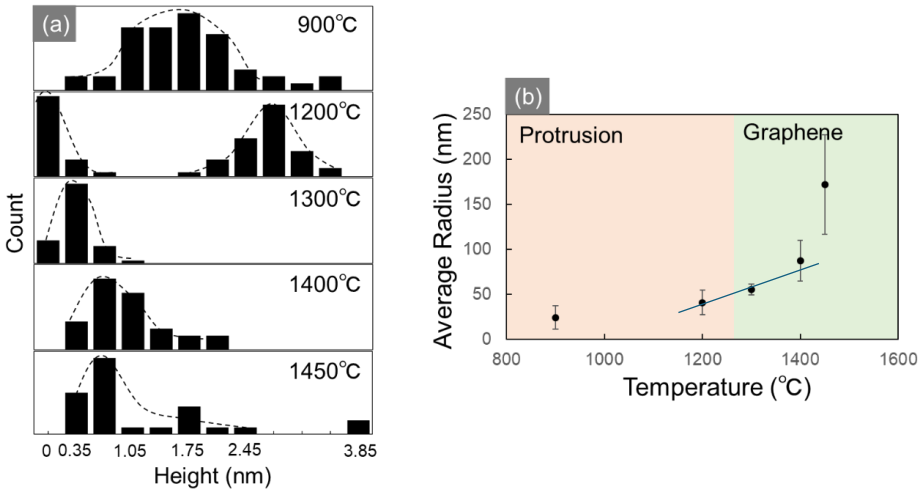

Figure 3.8 (a) Height distribution of the grown graphene islands evaluated from the AFM images and its temperature dependence. (b) Temperature dependence of the average radius observed from the grown islands.

Higher resolution STM images observed using HITACHI AFM5100N system were measured to examine the formation mechanism for the circular shape islands (Figure 3.9). STM images in Figure 3.9(a) indicated the graphene islands grown at 1300 ºC show a hexagonal shape composed of a single crystal. In this case, we determined the relative twist angle between the grown graphene and the epitaxial graphene from the edge direction in the hexagonal shape. As discussed in relation to Figure 3.3, the relative twist angle to the epitaxial graphene is random. This means that highly oriented 2D islands are randomly nucleated on the template graphene and expand to form highly crystalline twisted bilayer graphene via lateral growth.

For a higher growth temperature of 1400 °C or above, the shape of the grown graphene islands changes from hexagonal to circular with irregular shapes and sizes. In the circular graphene island grown at 1400 °C, intricate domain boundaries are observed, as indicated by the broken lines in Figure 3.9(b). Such domain boundaries are not observed in the epitaxial graphene template or hexagonal graphene islands grown at a lower temperature (Figure 3.9(a)). The moiré patterns with different periods are partly observed around the domain boundary, as shown in the enlarged images in Figure 3.9(b). Their periods are evaluated to be D = 16.6 nm and D = 19.6 nm. According to equation (1.1), the twist angles between the grown graphene and the epitaxial graphene in each image are estimated to be 0.85° and 0.72°, respectively [33, 34]. In some areas of the same island, moiré patterns are not observed. This may be due to a larger twist angle and much smaller moiré patterns that cannot be resolved in the STM images. These results indicate that the circular graphene islands grown at 1400 °C are composed of multiple domains with different crystal orientations.

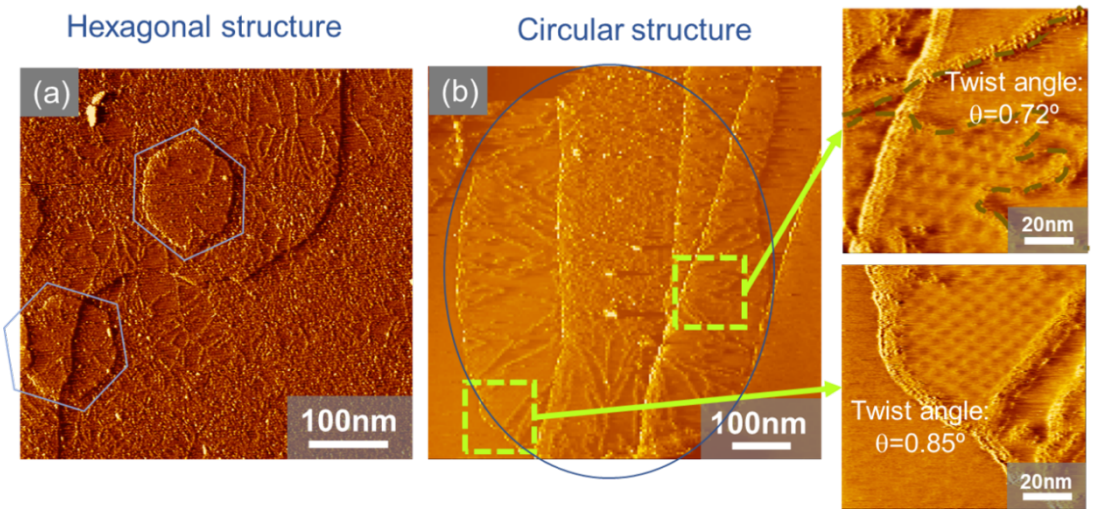

Figure 3.9 STM images (I = 244 pA, V = 0.1 V) observed from the graphene islands grown at (a) 1300 °C and (b) 1400 °C. Enlarged images of the regions indicated by the squares in figure 4(b) are shown to observe the moiré patterns.

3.4.2 Analysis of temperature dependence

The temperature dependence of graphene nucleation and growth rate is primarily influenced by three factors: growth driving force, carbon source decomposition, and template morphological instability.

a) Growth driving force

According to thermodynamic relations and performing Gibbs free energy in a close simple system [163]:

$$dG = -SdT + VdP \quad ...(3.1)$$

The partial derivative relationship is given by:

$$\left(\frac{\partial G}{\partial T}\right)_P = -S, \qquad \left(\frac{\partial G}{\partial P}\right)_T = V \quad ...(2)$$

The Gibbs free energy per particle is called the chemical potential μ [164].

$$\mu(P,T) = \frac{G(P,T,N)}{N} \quad \ldots(3)$$

Thus,

$$\left(\frac{\partial \mu}{\partial T}\right)_P = -\frac{S}{N}, \qquad \left(\frac{\partial \mu}{\partial P}\right)_T = \frac{V}{N} \quad \ldots(4)$$

For gas-solid growth processes, the relationship between growth driving force and temperature can be discussed using the diagram shown in Figure 3.10 [164]. Since volume V > 0, the blue and red lines in the figure represent the change in pressure P with respect to volume V under constant temperature conditions. Given that entropy S > 0, under constant pressure, an increase in temperature (represented by deep-colored lines) leads to a decrease in chemical potential μ. The extent of this decrease depends on the state of matter: since the entropy of the gas phase is greater than that of the solid phase ($S_{(g)} > S_{(s)}$), the change in the gas phase is more pronounced (represented by thin-colored lines).

For nucleation to occur, the actual pressure must exceed the equilibrium vapor pressure P_{eq}. As shown by the P_{growth} curve in Figure 3.10, as the processing temperature increases, the growth driving force decreases, making graphene nucleation less favorable.

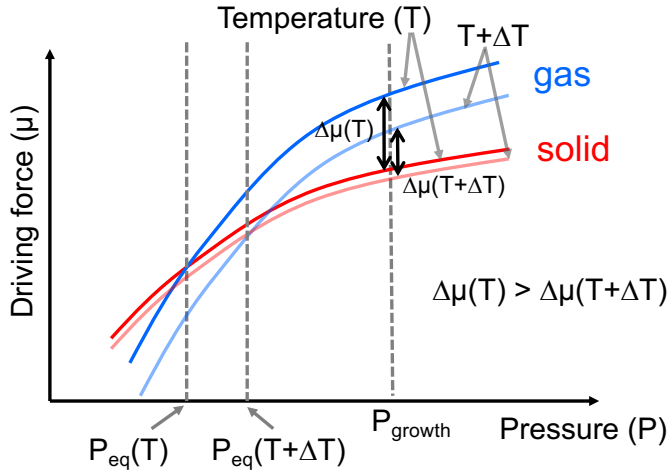

Figure 3.10 The relationship between temperature and driving force.

Considering the definition under standard state (denote standard state as "∘"), Δμ is

thermodynamically defined as [163]:

$$\Delta\mu(T,P) = \Delta\mu°(T) + RT\,\mathrm{ln}Q \ldots (5)$$

where $\Delta\mu°(T)$ is the standard Gibbs free energy change of the reaction at a temperature of T and standard pressure of $P°$ (generally taken as 1 bar). Q is the reaction quotient.

Assuming that the "effective reaction" can be simplified as:

$$C_{(g,\text{ from decomposition of ethanol})} \longrightarrow C_{(s,\text{ graphene})} \ldots (5)$$

Thus,

$$Q = \frac{a_{C(s)}}{a_{C(g)}} \ldots (6)$$

where the activity of solid $a_{C(s)}$ is usually approximated as 1. The activity of the gas phase is $P_{C(g)}/P°$. Therefore, the chemical driving force for the formation of solid carbon (graphene) can be characterized by:

$$\Delta\mu(T,P) = \Delta\mu°(T) - RT\,\ln\frac{P_{C(g)}}{P°} \ldots (7)$$

Therefore, for two different temperatures at a constant pressure, the change in the growth driving force can be expressed as follows:

$$\Delta\mu(T_1) - \Delta\mu(T_2) = [\Delta\mu°(T_1) - \Delta\mu°(T_2)] - \left[RT_1\,\ln\frac{P_{C(g)}}{P°} - RT_2\,\ln\frac{P_{C(g)}}{P°}\right]$$
$$= [\Delta\mu°(T_1) - \Delta\mu°(T_2)] - (T_1 - T_2)\left(R\ln\frac{P_{C(g)}}{P°}\right) \ldots (8)$$

For graphene growth on a graphene template under a carbon precursor pressure of 28 Pa (based on an experimental ethanol pressure of 14 Pa, assuming complete decomposition and neglecting other complex side reactions), the difference in driving force at 1300°C (T_1 = 1573 K) and 1400°C (T_2 = 1673 K) is estimated as follows:

$$\Delta\mu(T_1) - \Delta\mu(T_2) = [\Delta\mu°(T_1) - \Delta\mu°(T_2)] + 6.8\ \mathrm{kJ/mol} \ldots (10)$$

where R is the ideal gas constant, taken as 8.31 J/(mol·K). Referring to the JANAF

thermodynamic tables [165], the value of $[\Delta\mu^\circ(T_1) - \Delta\mu^\circ(T_2)]$ is approximately 15.8 kJ/mol. Thus,

$$\Delta\mu_{T1} - \Delta\mu_{T2} \approx 22.6\ \text{kJ/mol}$$

The above calculations further prove that the driving force decreases with increasing temperature. Obviously, the results of this study show the opposite trend to thermodynamic calculations. Therefore, other factors contributing to accelerated growth with increasing temperature need to be considered.

b) Carbon source decomposition

As temperature rises, carbon sources decompose more completely. According to theoretical calculations in hot-wall system, complete decomposition occurs within a few seconds at temperatures exceeding 1000°C [128]. However, in this study, the CVD system is equipped with a cold-wall reactor, where only the substrate and its immediate surroundings are locally heated. This suggests that due to the short residence time (far less than the order of seconds), ethanol passing through the heated zone of the reactor does not fully decompose. Therefore, even at 1300°C, complete decomposition may not occur.

As temperature increases, the production of reactive carbon species leads to a higher effective partial pressure, which promotes graphene nucleation.

c) Instability of template morphology

As described in the previous section (Reasons for random stacking structure), strained and defective graphene are the primary factors contributing to the instability of template morphology. On one hand, increasing the temperature enhances the reactivity of these unstable surfaces. On the other hand, the etching effect of oxygen-containing byproducts from ethanol decomposition becomes more pronounced at higher temperatures, leading to the formation of additional defects on the graphene template

surface.

These defects provide more sites for active carbon atoms to bind via vacancy bonds, potentially serving as nucleation sites on the template graphene during the initial growth stage. Therefore, a moderate increase in temperature promotes the formation of active sites, facilitating graphene nucleation. Notably, excessive temperature elevation can exacerbate template instability, leading to undesirable nucleation behaviors or the formation of non-graphene structures.

d) Conclusion

The nucleation of graphene is influenced by the interplay of three key factors, as discussed earlier. From the findings in this chapter, it appears that the promotions of carbon source decomposition and the changes in template structure become more significant than the growth restrictions imposed by thermodynamic forces as the temperature rises.

3.5 Initial growth investigation of twisted graphene

Figure 3.11 compares representative AFM images observed from the grown samples with the process duration of 1.5 min, 3 min, and 15 min to examine the time evolution of graphene island formation at 1450 °C. For the initial growth stage (Figure 3.11(a)), the density of graphene islands is relatively high although the island size is small and accordingly, the surface coverage of the island area is relatively low. As the growth process proceeds, the island density becomes lower and after the growth for 3 min, it reaches about one-tenth of that for the initial stage (Figure 3.11(b)). The island size is observed to be significantly enlarged after the growth for 3 min The island area expands remarkably after the further growth process for 15 min to form huge graphene islands covering almost the entire surface (Figure 3.11(c)). This observed behavior indicates that large graphene islands with low density are not formed simply by lateral growth of

nucleated carbon clusters, but instead, are formed by fusion of the high-density graphene islands in addition to the lateral growth. Consequently, the large graphene islands may exhibit irregular shapes and inhomogeneous sizes. This may be a similar process to the coalescence observed on the surface of the copper foil [166]. Note that the domain boundaries are observed in the fused graphene islands, possibly due to the random crystalline orientation of graphene islands formed on the graphene template. The coalescence phenomena of graphene islands shown here coincide with the analyzed results on twist angle indicated in Figure 3.9(b).

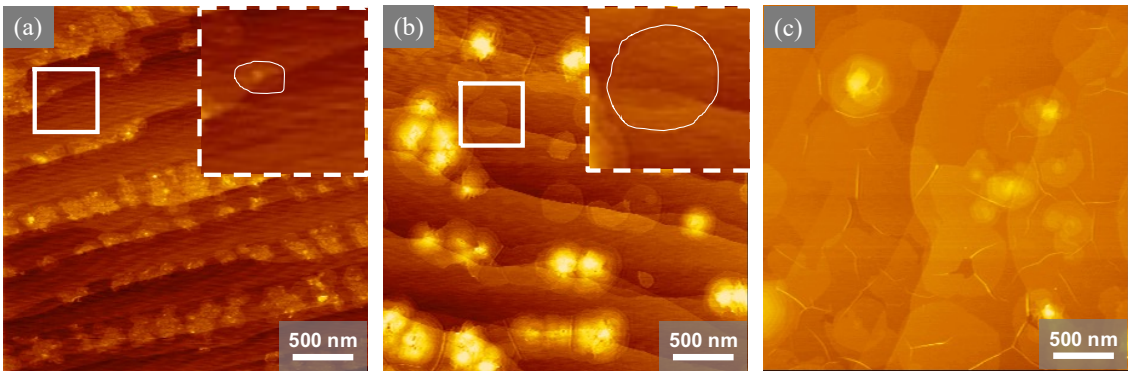

Figure 3.11 AFM images observed from the graphene islands after growth at 1450 °C for a process time of (a) 1.5 min, (b) 3 min and (c) 15 min.

3.6 Mechanism of twisted graphene grown on graphene/SiC template

Based on structural analysis of graphene islands grown in a temperature range of 900 - 1450 ºC, we propose a model for the growth behavior of tFLG on the epitaxial graphene template (Figure 3.12). At a lower growth temperature, the chemical potential of the carbon species in the gas phase is relatively high and the rate of crystallization from the adsorbed carbon species is too slow to form graphitic structures. Accordingly, the small amorphous-like nanocarbon aggregations tend to form at lower temperatures (Figure 3.12(c)). At a higher growth temperature (~1300 ºC), hexagonal graphene 2D islands composed of a single-crystalline domains are preferentially formed with random

twist angles (Figure 3.12(b)) since the crystallization rate becomes fast enough for the formation of graphitic structures. When the growth temperature increases above 1400 °C, the chemical potential of carbon atoms on a graphene surface should decrease according to the energetics based on thermodynamics.

The nucleation density at 1400 °C should decrease, but the observed phenomena is the opposite (Figure 3.12(a)). To explain this unexpected result, we should take the change of the surface layer structure and the reaction environment at higher temperatures into consideration on the growth mechanism. The most significant factor on the nucleation density should be the adsorption of oxygen or the carbon species formed in the gas phase on the growth sites as well as the incomplete decomposition of ethanol. The CVD system in this work is equipped with a cold-wall reactor, where only the sample substrate and its vicinity are heated locally. This situation suggests that ethanol may not be completely decomposed even at 1300 °C due to a short period, which is insufficient for ethanol to react while passing through the heating region of the reactor. In this case, the thermal process at 1400 °C should promote ethanol decomposition and the reactive carbon species generated at higher temperature increases the effective partial pressure. Namely, the chemical potential of the carbon species is greater than the compensation for the temperature increase. Consequently, the nucleation density possibly increases at 1400 °C, as observed in this experiment, but is contrary to expectations based on thermodynamics.

Oxygen-containing species formed by ethanol decomposition should be another factor on the nucleation density at 1400 °C. The etching effect by the oxygen-containing species should be enhanced at a higher temperature, producing defects on the surface of the graphene template such as the dark depressions in Figure 3.3(a). With the help of the defect sites on the continuous graphene template as a starter, Si species may sublimate from the SiC substrate. Activated carbon atoms remaining on the surface may act as active sites on the template graphene for nucleation at the initial growth stage.

After growth proceeds, larger graphene islands with a circle shape are formed by the

coalescence of many smaller graphene islands with random twist angles. Hence, each larger island contains many domains with various twist angles. The domain boundaries in a grown graphene island contain excess dangling bonds and may play a role in the nucleation sites on the grown islands. Additional graphene layers are grown, finally forming Few-layer graphene islands, as illustrated in Figure 3.12(a). Analysis of the growth behavior indicates that control of the chemical potential, or the growth driving force, is a key factor to achieve ideal growth of twisted graphene with a large area and a low defect density.

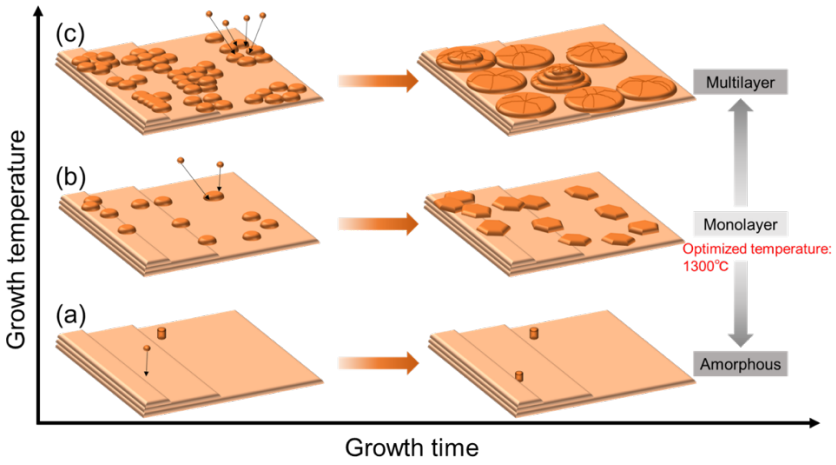

Figure 3.12 Schematic model for the growth behavior of tFLG on the epitaxial graphene/SiC template. (a) Below the optimum temperature, graphene is not formed, but a small amount of amorphous-like carbon materials precipitates on the sample surface. (b) At the optimum temperature, graphene precursors nucleate at a relatively low density on the surface. As the growth process proceeds, graphene seeds grow in the lateral direction, forming faceted hexagonal graphene islands composed of single-crystalline domains. (c) Beyond the optimum temperature, graphene nucleates at a relatively high density for the initial growth stage, possibly due to the change in the surface layer structure and reaction environment at higher temperatures (see text). As for the latter growth stage, small graphene islands formed in the initial stage aggregate into larger ones composed of multiple domains with various twist angles. Nucleation of graphene

continues on the defective two-dimensional islands, leading to the formation of three-dimensional islands.

3.7 Conclusion

Overlayer growth of graphene on an epitaxial graphene/SiC by ethanol CVD without a metal catalyst was examined over a wide growth temperature range from 900 °C to 1450 °C. The lateral and vertical growth behaviors of graphene and the grown graphene structures were investigated through AFM and STM observations. The structural analysis indicates that graphene islands grown at 1300 °C form hexagonal twisted bilayer graphene as a single crystal, although islands grown at a higher temperature (~1400 °C) are composed of several graphene domains with different twist angles. The extraordinary increase in the nucleation density and the coalescence growth process for the formation of circular graphene islands are observed for a higher temperature. This unusual behavior can be understood by the structural deformation of the sample surface due to a reactive environment. Based on the analysis of the dependence on growth temperature and time, we propose a growth model of the graphene overlayers with respect to the crystallinity (amorphous, single-crystalline, and polycrystalline) and layer numbers (monolayer and few-layer). Further optimization of the process conditions based on this work should prepare single- crystalline monolayer and few-layer graphene covering the entire surface of the template graphene with very low densities of defects and macrostructures such as wrinkles, which seriously degrade the graphene performance.

Chapter 4. Suppression of nucleation density in twisted graphene domains grown on graphene/SiC Template by sequential thermal process

4.1 Background

tFLG exhibits massless fermion behavior and linear dispersion of the electronic band near the Fermi level due to the misorientation of Bernal-stacked or rhombohedral-stacked graphene [5,167]. This behavior extends the electronic versatility of such 2D carbon materials. Owing to the weak interlayer coupling and screening effect [136], graphene is less influenced by the charged impurities on a substrate [140]. Thus, tFLG is a promising candidate to be applied to field-effect transistors, optoelectronics devices, and microsupercapacitors, as it enhances the transport characteristics [42,135,168,169].

A widely used method for fabricating tFLG involves the repeated transfer of monolayer graphene prepared by mechanical exfoliation [10], but the use of polymer stamps for transferring exfoliated graphene limits its scalability. CVD has been reported in numerous studies as a method for growing graphene on a large area. In these studies of CVD growth, the metal foil and hydrocarbons (methane, acetylene, etc.) were typically used as a catalytic surface and a carbon source to produce scalable graphene, respectively [53] . Unfortunately, fabricating more than two layers of twisted graphene on the copper foil remains challenging [114] due to the surface-mediated and self-limiting processes dominated in the CVD growth of graphene [46]. This limitation arises from the considerably high energy barrier on graphene surface for forming additional layers. A breakthrough approach of nucleating the second graphene layer involves the decomposition of ethanol to produce CH_3 radicals, which offer optimal binding energies on few-layer graphene/Cu. The suitable binding energies significantly promote nucleation on the graphene terrace, fostering the growth of graphene islands. Additionally, the OH radicals formed by ethanol decomposition potentially aid in reducing the activation energy required for dehydrogenation of graphene edges. This mechanism facilitates the layer-by-layer growth of graphene islands, thereby contributing to the formation of a

second graphene layer [118,119]. However, owing to the surface process induced by catalytic effect of the metal substrate, the resulting configuration between graphene layers tends towards AB stacking for bilayer graphene on Cu [118]. Thus, to simultaneously overcome both the limitations of the layer number and the twisted structure, the monolayer graphene is utilized as a template for non-catalyst layer-by-layer growth using the ethanol as the carbon source [170,171].

In the previous work, we demonstrated the twisted structure of CVD-G layers on monolayer graphene templates by STEM and G' peak analysis of Raman spectroscopy [135,139]. Moreover, using graphene from the thermal decomposition of SiC as a template, CVD-G grown on SiC-G with a twisted bilayer structure was observed with a STM [172]. The method of growing graphene on a graphene template lays the foundation for the study of tFLG applicable to high-performance electrical devices. However, the scattering effect of charged impurities in wedding cake-shaped multilayer graphene reduces carrier mobility, limiting the high quality of tFLG field-effect transistors [139]. Hence, studying the morphology of tFLG and understanding the layer-by-layer growth mechanism are the keys to improving the quality of graphene.

The process to achieve layer-by-layer growth is influenced by several factors, encompassing reaction conditions such as temperature, duration, and carrier gas flow rate [173,174] in addition to aspects like interface mismatches, surface defects, and substrate surface cleanliness . A previous study of grown tFLG revealed that the nucleation density is too high to allow sufficient space for the lateral growth of the graphene domain, which refers to graphene formed by binding carbon adatoms extending along the edges from a single nucleation site [172]. With the locally high nucleation probability, graphene is grown into multilayer domain islands due to successive nucleation in the new layer [116,174]. Therefore, reducing the nucleation probability is crucial for the layer-by-layer growth of CVD-G. When the two growth processes of SiC-G and CVD-G were performed, the samples were taken out of the growth chambers [172]. Consequently, the air-exposure

(AirE) process is considered to lead to the deposition of contaminants on the SiC-G surface [178], which may be one of the factors affecting the excessive nucleation and island-shaped growth of CVD-G. The effects of the surface cleanliness of template graphene should be investigated in detail, and ideal layer-by-layer growth conditions should be created to grow high-quality tFLG.

In this study, we examined an effective approach to growing tFLG with reduced nucleation density by restricting the exposure of template graphene to ambient air before CVD. We performed growth processes of SiC-G and CVD-G in the same chamber to create a sequential thermal (ST) process. As a result, the nucleation density of CVD-G decreased significantly, and the layer domains grew to have a larger radius and lower height compared to the case of the AirE process. This effect was attributed to the absence of air contaminants on the graphene templates during the ST process. Additionally, we discussed the temperature dependence and etching effect based on the suppression of nucleation density. We also proposed a growth model to systematically explain the nucleation and growth mechanism of CVD-G on graphene templates. This approach provides a basis for manufacturing high-quality tFLG consisting of large-domain single-crystal graphene.

4.2 Experiment design

Two coordinated growth stages were suggested in preparing tFLG: one of template monolayer SiC-G and one of CVD-G. A schematic diagram of the growth stages is shown in Figure 4.1. The SiC-G growth stage involves ultrahigh-temperature annealing to obtain graphene on SiC as a stable template for the following stage. The CVD-G growth stage involves growing graphene by CVD on the template SiC-G at high temperature while supplying ethanol as a carbon source. As depicted in Figure 4.1a, the process of exposing the sample to air between the two stages [139] is referred to as the AirE process.

Conversely, in the ST process, the two growth stages are carried out in the same chamber, which is isolated from the air environment, as illustrated in Figure 4.1(b). During the cooling transition between the two stages of the ST process, it is necessary to ensure that samples are in a continuous vacuum environment.

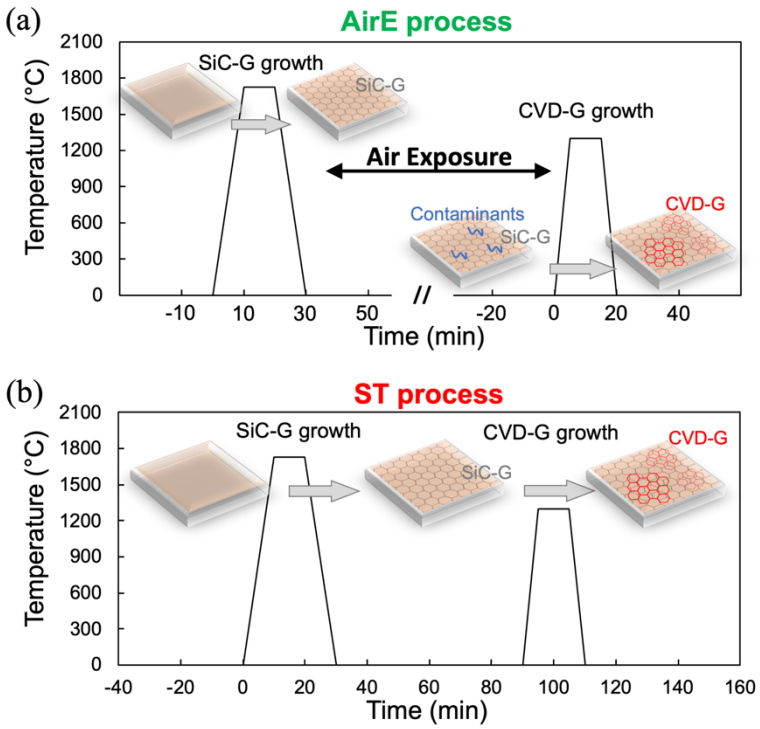

Figure 4.1 Schematic diagram of SiC-G and CVD-G growth of graphene in (a) AirE process and (b) ST process.

For the SiC-G growth stage, commercial 6H-SiC(0001) substrates (on-axis, semi-insulating purchased from II-VI Advanced Materials) were annealed at 1700 °C and 40 kPa for 10 min in an argon atmosphere[154]. In the CVD-G growth stage, graphene layers were synthesized without a metal catalyst by flowing a mixture of ethanol/argon (typically 1 sccm/100 sccm) at a total pressure of 10.5 kPa, corresponding to an ethanol partial pressure of 105 Pa. To compare the initial growth stage with respect to graphene nucleation of the ST and AirE processes, we conducted the growth of CVD-G at 1200 °C

for 10 min in both processes. To obtain more details about the difference in graphene nucleation between the two processes, the dependence of ethanol partial pressure was systematically investigated in both the AirE and ST processes. By adjusting the mixture ratio of ethanol to argon, the partial pressure of ethanol was varied from 15 to 530 Pa, while the temperature and growth time were kept at 1400 °C and 10 min, respectively. Furthermore, to investigate the CVD-G growth behavior in the ST process, we investigated a wide range of temperatures from 1000 to 1500 °C for 25 min at an ethanol partial pressure of 105 Pa. All the high-temperature treatments were conducted using an infrared heating furnace (SR1800G, Thermo Riko) which is a cold-wall system where the sample stage is heated to high temperatures while the chamber walls are not.

The grown tFLG was characterized using several analytical techniques. AFM (AFM5100N, Hitachi High-Tech) observations were conducted in dynamic force mode under atmospheric conditions at room temperature. A Raman spectrometer (HR800, Horiba) was used to analyze the layer number and twisted structure of the CVD-G, using a laser excitation of 532 nm with a 100× objective lens (typical spot diameter was ~1 μm). A previously developed method [179] was employed to subtract the spectra from the SiC substrates. The Raman spectra presented in this study were normalized to the characteristic peaks of the SiC substrates. By comparison of the G-band of SiC-G and that of the samples after CVD-G growth, it was possible to estimate the growth amount and layer number of CVD-G.

4.3 Effect of nucleation suppression in sequential thermal (ST) process

To examine the impact of surface cleanliness, we performed a set of control experiments, comparing the ST process with the AirE process, as shown in Figure 4.2. These experiments were conducted under optimized conditions at 1200 °C with an ethanol partial pressure of 105 Pa for 10 min, which were chosen to minimize the

occurrence of CVD-G domain coalescence for the initial growth stage with respect to graphene nucleation. We investigated the growth morphology, including the nucleation density, domain radius, and domain height of CVD-G in both the ST and AirE processes. A total of 12 sets of AFM images, each measuring 5 μm × 5 μm, were captured for both the ST and AirE processes for statistical analysis. Figure 4.2(a)–(c) represents one set of examples in the ST process, and Figure 4.2(d)–(f) represents one set of examples in the AirE process.

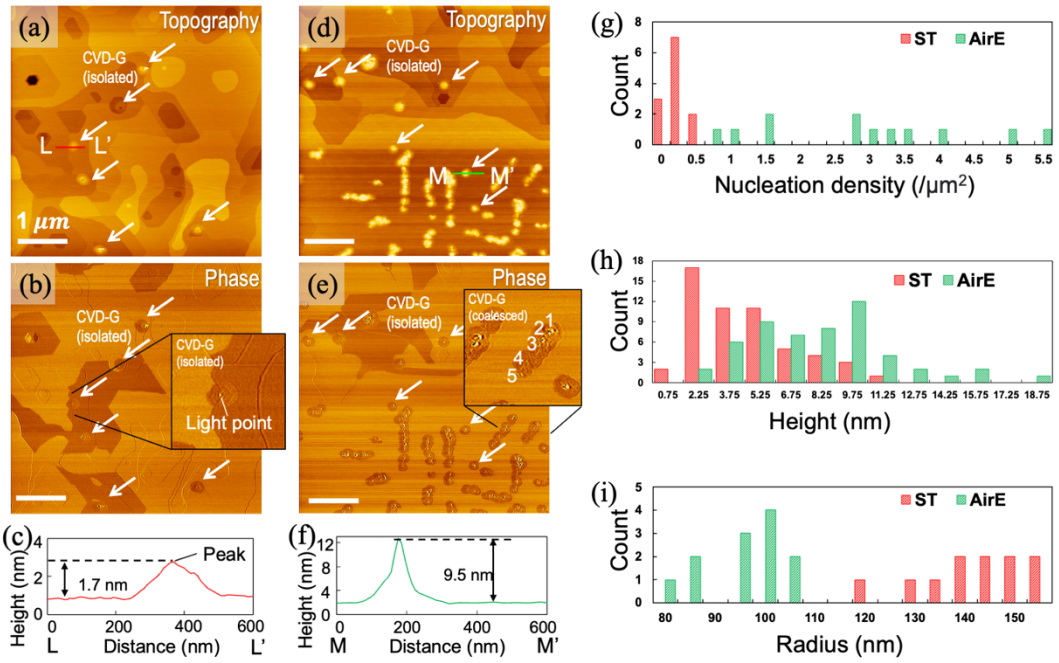

Figure 4.2 AFM images of the samples after CVD growth at 1200 °C for 10 min with an ethanol partial pressure of 105 Pa in the (a, b) ST process and (d, e) AirE process. (c) Cross-sectional view of red line segment L–L′ shown in (a). (f) Cross-sectional view of green line segment M–M′ shown in (d). Statistical distribution of the (g) nucleation density, (h) height of isolated and coalesced domains, and (i) average radius of isolated domains of CVD-G from 12 sets of AFM images in both the ST process and the AirE process.

As seen in Figure 4.2(a), (b), (d) and (e), the isolated domains and coalesced domains of CVD-G can be distinguished. The isolated domains, which refer to graphene formed from a single nucleation site and with approximately circular shapes, are indicated by arrows. A singular peak observed at the center of the domain is regarded as the nucleation site, as exemplified in Figure 4.2(c), which corresponds to the bright spot seen in the magnified phase image illustrated in Figure 4.2(b). In the case of the coalesced domains with irregular-shaped structures, the number of nucleation sites was estimated by counting the bright spots in the phase images. The magnified image of Figure 4.2(e) shows an example of one coalesced domain with five nucleation sites. The height was evaluated based on the cross sections (Figure 4.2(c), (f)) of both the isolated and coalesced domains. To clearly demonstrate the ability of lateral growth under different surface states in the two processes, the radius was evaluated exclusively by analyzing the cross sections (Figure 4.2(c), (f)) of the isolated domains.

The statistical data (Figure 4.2(g)) show that the ST process yielded significantly fewer nucleation sites compared to the AirE process. The CVD-G domains that formed in the ST process were fewer and more dispersed throughout the surface (Figure 4.2(a)), while the CVD-G domains that formed in the AirE process were numerous and locally coalesced (Figure 4.2(d)). Upon examination of the cross sections of the CVD-G domains, the statistical results (Figure 4.2(h), (i)) show that CVD-G from the ST process presented a lower height and a larger radius, indicating a greater potential for the formation of laterally grown large-domain graphene compared to that from the AirE process.

In addition to the comparison under optimized conditions, we also expanded the comparison between the ST and AirE processes under a range of varying pressure conditions for 10 min at 1400 °C. In the cold-wall system of our experiment, temperatures as high as 1400 °C are crucial for studying the partial pressure dependence. This high temperature is beneficial for achieving sufficient ethanol decomposition while also reducing the possibility of graphene nucleation, enabling critical nucleation conditions to

be observed in both processes. Figure 3(a)–(h) shows the AFM topography of the two processes. In Figure 4.3(a), (e) and (f), no graphene was grown. In Figure 4.3(b), monolayer 2D graphene domains were grown. In Figure 4.3(c), (d), (g) and (h), multilayer graphene domains were grown, forming multilayer graphene on the surface. The coverage (Figure 4.3(i)) determined from the AFM images obviously exhibited growth within different partial pressure ranges. This observation suggests that the critical saturations of the carbon sources for nucleation differ for the two processes. The nucleation threshold in the ethanol partial pressure for the ST process (53–105 Pa, Figure 4.3(f) and (g)) was observably higher than that for the AirE process (15–53 Pa, Figure 4.3(a) (b)). Figure 4.3(j) presents the Raman spectra that correspond to the AFM images shown in Figure 3(a)–(h). At 53 Pa, the intensified G-band and G′-band in the AirE process are attributed to the growth of CVD-G, while the spectra of the ST process demonstrate only the presence of a monolayer SiC-G template with buffer layer contributions. The Raman results are consistent with the AFM observations. It is worth noting that the Raman intensity of the G-band from the grown monolayer graphene is relatively weak. Hence, the substantial contribution of the G-band in the template graphene and buffer layer [146] on SiC is dominant in the observed Raman spectrum. Consequently, the differences in island density of the monolayer CVD-G are hard to distinguish from the Raman spectra. Over 53 Pa, the Raman intensity indicates a lower nucleation density in the ST process than in the AirE process.

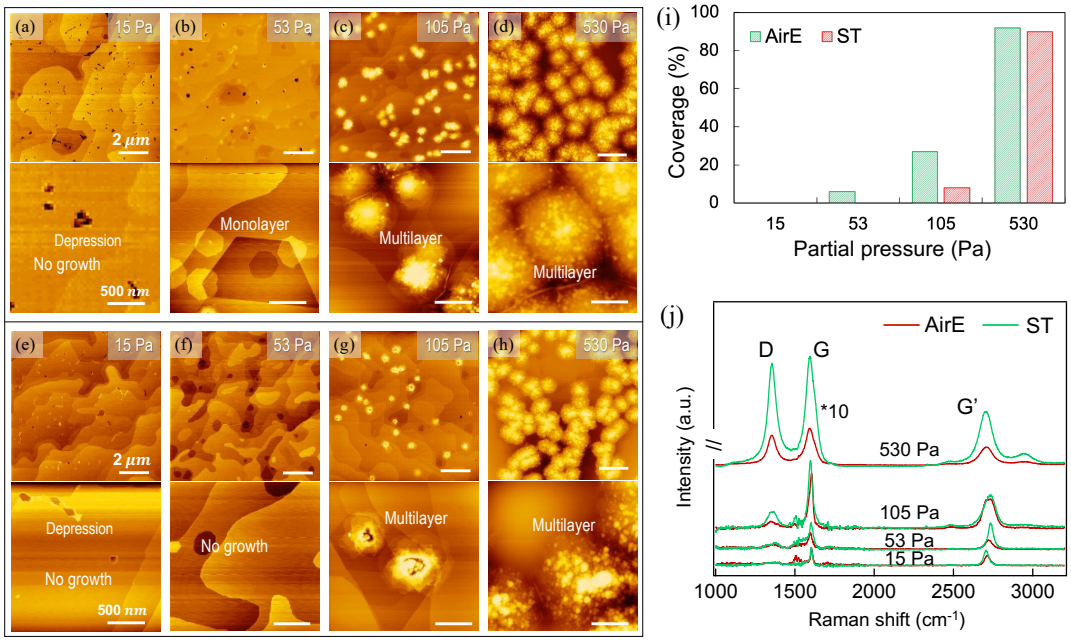

Figure 4.3 AFM images of the samples after CVD growth at 1400 °C for 10 min with various partial pressures of ethanol in the (a–d) AirE process and the (e–h) ST process. Comparison of AirE and ST processes in (i) coverage of grown CVD-G and (j) Raman spectra with 532 nm laser excitation. All these spectra are the results after the subtraction of the SiC substrate peaks and normalization.

We hypothesize that the effect of suppressing graphene growth in the ST process is due to the prevention of surface contaminants. In the AirE process, due to the interaction with the SiC(0001) substrates and carbon-rich buffer layers, the surface of SiC-G usually adsorbs contaminants, such as adsorbed oxygen, hydrocarbon, or water [180], when it is exposed to the ambient environment. The contaminants existing on the surface of SiC-G decompose at high temperatures during the CVD-G growth stage. On the surface of SiC-G, the decomposition of contaminants provides active sites with low surface energies [181] or where dangling bonds may exist [182], leading to the locally high nucleation density of CVD-G. Therefore, the extended diffusion length of adsorbed carbon atoms on a pristine surface provides a rational explanation for the decreased nucleation density in

the ST process [183].

4.4 Temperature dependence of grown graphene in ST process

To investigate the growth mechanism of CVD-G in the ST process in detail, we performed a parametric study of the growth temperature. Figure 4.4(a)-(l) shows the CVD-G growth morphology from AFM images as a function of growth temperature for the ST process. Figure 4(m) is a representative cross-sectional view of a graphene domain, which corresponds to the dotted line N–N′ in Figure 4.4(l). By employing the same statistical method described in section 4.3, Figure 4.4(n) illustrates the average radius of the isolated domains, revealing an increase in the domain radius with growth temperature. Moreover, as shown in Figure 4.4(o) and (p), the height and nucleation density were determined from AFM topography images, including the isolated and coalesced domains. The density of the CVD-G domains decreased and the height of CVD-G increased as the temperature increased. All trends of height, domain radius, and nucleation density were interrupted at 1300 °C with the disappearance of CVD-G. This disappearance suggests that the dominant mechanisms are different at temperatures below and above 1300 °C, which are explained in the next section. Furthermore, in the temperature range of 1100–1300 °C, isolated domains showed mono- or few-layer growth. At temperatures above 1300 °C, isolated domains showed larger multilayer growth, and striking pits were observed at the center of all domains (Figure 4.4(k) and (l)). As indicated in Figure 4(m), the depth of the pit was approximately 5 nm. This value is significantly larger than the layer distance of the graphene connected to SiC by the buffer layer [184]. At 1500°C, deeper pits are etched rather than more numerous ones. As a result, graphene is highly likely to grow at the bottom of the pits, which makes it challenging for us to quantify. Moreover, with the increase in temperature, the lower diffusion length due to the shorter residence time makes nucleation more difficult. This is likely one of the main reasons for the reduction in nucleation.

Since the Si-C bond breaking temperature is very high, the formation mechanism of pits needs further explanation. The formation of deep pits in epitaxial graphene is associated with the vacuum thermal decomposition method, which involves a lower decomposition temperature (~1140°C) [185]. To obtain high-quality monolayer graphene, our template graphene was thermally decomposed in an argon atmosphere at approximately 40 kPa. Argon plays an inhibitory role, allowing decomposition to occur at a high temperature of 1700°C. In contrast, under CVD growth conditions, the pressure is only 10 kPa, and the gas is in a flowing state. As a result, buffer layer damage is reduced under low pressure. Additionally, oxidizing substances such as H_2O, CO, and CO_2 accelerate the breaking of Si-C bonds.

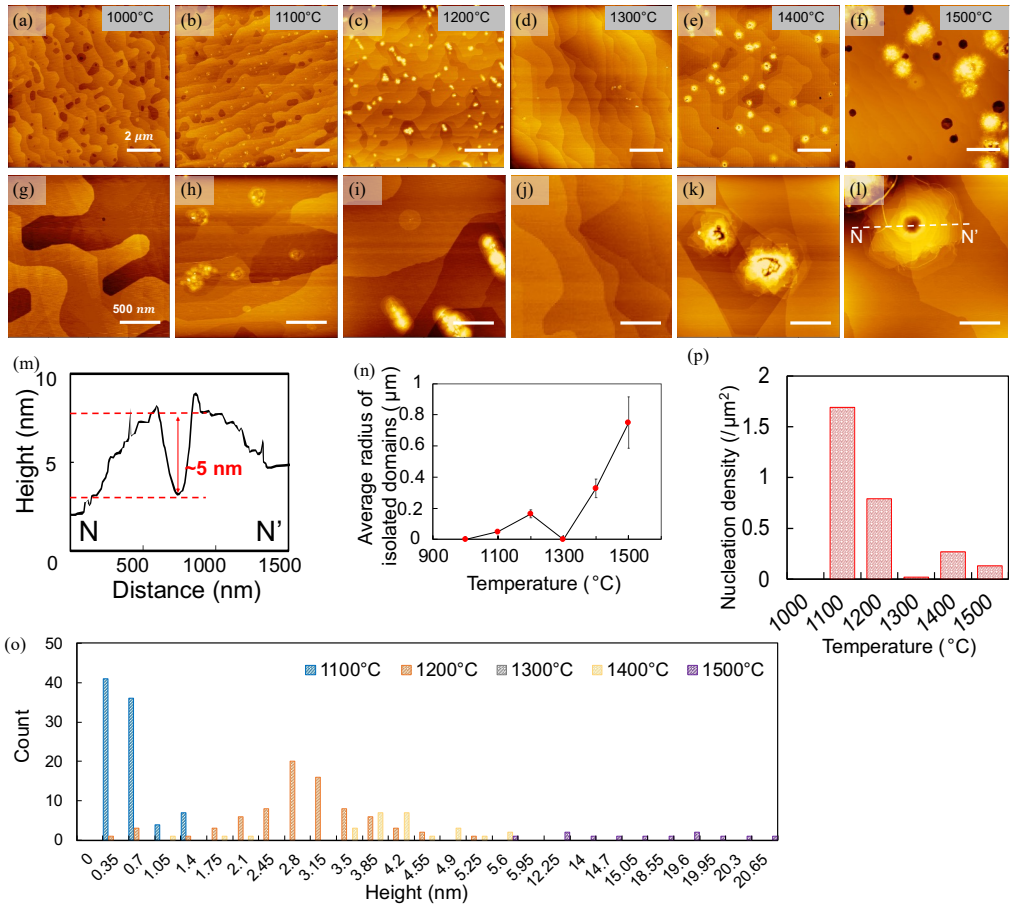

Figure 4.4 AFM images of the samples after CVD growth in the ST process on graphene templates/SiC substrates for 25 min with an ethanol partial pressure of 105 Pa at (a) 1000,

(b) 1100, (c) 1200, (d) 1300, (e) 1400, and (f) 1500 °C. (g–l) Magnified AFM images of (a–f). (m) Cross-sectional view of dotted line segment N–N′ shown in (l). (n) Temperature dependence of average radius of isolated domains observed from grown CVD-G from AFM images. Statistical distribution of (o) height and (p) nucleation density of CVD-G domains evaluated from AFM images at different temperatures.

4.5 Structure analysis of twisted graphene

Figure 4.5 shows the Raman spectra of the ST process samples and a sample of only SiC-G growth. The Raman spectrum of the only SiC-G growth sample exhibited characteristic peaks of monolayer graphene corresponding to the G-band around 1600 cm^{-1} and the G′-band around 2734 cm^{-1}. These features also align with the characteristics of epitaxial monolayer graphene on SiC substrates [186]. The Raman spectra of the sample after CVD-G growth at 1000 and 1300 °C were almost identical to that of only SiC-G. This confirms the absence of any CVD-G growth at this temperature and is consistent with the statistical results from the AFM images. Within the temperature range 1100–1200 °C, particularly at 1200 °C, the relative intensity of the G-band (including the contribution from the buffer layer [146]) increases, which serves as indicative evidence of CVD graphene growth. The morphologies of the samples observed by AFM are consistent with the Raman spectroscopy results. As the temperature continues to rise above 1300 °C, the relative intensity of the G-band increases significantly, which is a result of the combined effects of extensive CVD graphene growth and changes in the buffer layer.

Moreover, for the area completely covered by graphene (domain size must be larger than the typical spot diameter of the Raman spectrometer: ∼1 μm), we analyzed the ratio of twisted CVD-G at 1200 °C (Figure 4.5(b)). The G′-band of the spectrum was fitted with three Lorenz curves to calculate the proportion of AB stacking and twisted stacking

to estimate the ratio of twisted graphene [187]. G'_{2D} for two-dimensional (2D) graphene component, G'_{3DA} and G'_{3DB} for three-dimensional (3D) graphite component, to calculate the AB-stacking proportion:

$$R = \frac{I_{G'_{3DB}}}{I_{G'_{3DB}} + I_{G'_{2D}}} \qquad (4.1)$$

Then, the twisted ratio is represented by 1–R. By measuring the G'_{2D} band peak position of monolayer SiC-G, the fitting conditions for this study were set G'_{3DA}, G'_{3DB} of graphite, ($G'_{3DA} \sim G'_{2D}$ 18 cm^{-1}, $G'_{3DB} \sim G'_{2D}$ 27 cm^{-1}, $I_{G'3DA} : I_{G'3DB} = 1:2$), respectively. Peak fitting of the G'-band was performed using Igor Pro (manufactured by HULINKS) as analysis software. As a result, the normalized intensity of the three fitted Lorenz curves $I_{G'2D}$, $I_{G'3DA}$, and $I_{G'3DB}$ are 2318, 367, and 735, the twisted ratio at 1200 °C was determined to be 76%. It is significantly higher than that of few-layer graphene obtained by metal-catalyzed CVD [188,189], where there is a preference for the growth of AB-stacked graphene.

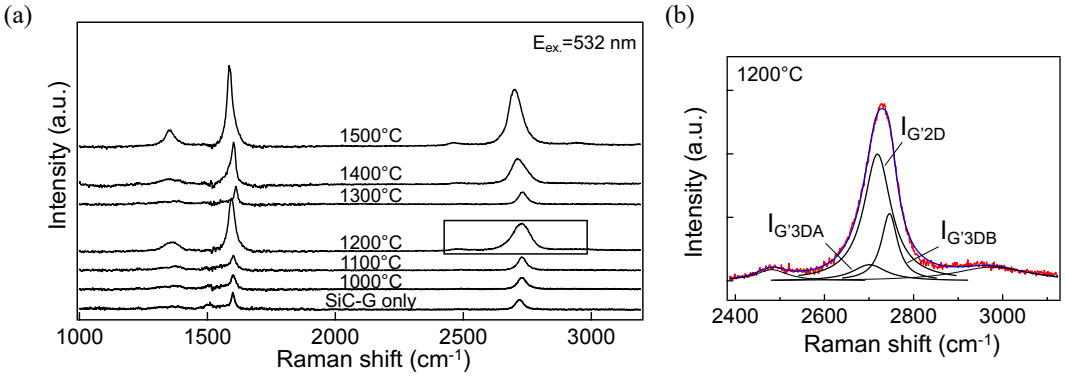

Figure 4.5 (a) Raman spectra (with 532 nm laser excitation) of SiC-G grown by ST process at various temperatures. (b) Three fitted Lorenz curves of G′-band in the Raman spectrum at 1200 °C. The ratio of twisted graphene was calculated to be 76%, which is close to the ratio at 1400 °C in both the ST and AirE processes (77% and 82%, respectively) (see Figure 4.6). All these spectra are the results after the subtraction of the SiC substrate peaks and normalization.

Additionally, at a higher ethanol pressure of 530 Pa at 1400 ºC for 10 min, in which multilayer graphene was grown to cover almost the entire surface, the ratios of twisted structure in tFLG are also calculated by fitting the peak shape of the G'-band. Both AirE and ST processes show twisted structures with ratios of 82% and 77%, respectively.

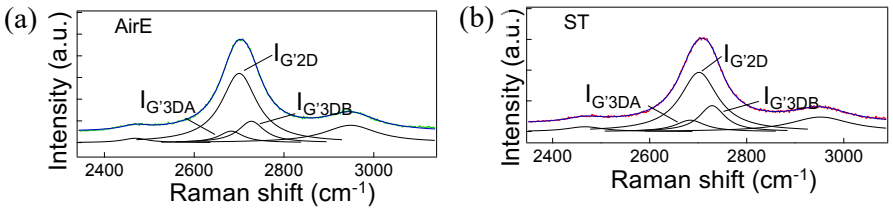

Figure 4.6 Three fitted Lorenz curves analyzed from the G'-band in Raman spectra for (a) AirE and (b) ST processes

The high ratio of the twisted structure agrees with the monolayer graphene growth with a random moiré pattern observed in our previous study [172]. Additionally, the high ratio of the twisted structure agrees with the microscopic observations in our previous studies [139,172]. The twisted structure in grown graphene has been previously observed using scanning transmission electron microscopy [139]. Additionally, the various moiré patterns of twisted bilayer graphene have been previously observed using STM (Section 3.3). It should be emphasized that the present study demonstrates multilayer CVD-G growth while maintaining a high twisted ratio on a scale exceeding a micrometer. This result confirms that our approach in this study is remarkably effective at obtaining tFLG in a scalable manner.

4.6 Mechanism of twisted graphene grown on graphene/SiC template in ST process

In this study, SiC-G was consistently arranged in tiles across the surface of SiC,

serving as a uniform template for subsequent CVD growth. This method avoids direct nucleation connected with atomic steps, enabling the epitaxial growth of graphene on SiC [190]. Therefore, crystal growth theories of 2D nucleation are considered as the basis of graphene growth models. A prior study [191] has described the energy difference of graphene with AB stacking and twisted stacking, elucidating the comparatively higher energy of twisted-stacked graphene as a metastable state. In the case of graphene growth without metal catalytic templates [172], the randomly formed graphene nuclei needs to be thermally excited at temperatures over 2000 °C to surmount the activation energy barrier to transform graphene from random stacking to AB stacking[187]. However, our CVD growth was conducted at temperatures lower than 1500 °C, prohibiting the graphene nuclei from overcoming the activation energy barrier. This energy barrier causes the randomly formed graphene nuclei to maintain a twisted angle, prompting graphene to form metastable twisted stacking during the growth stage.

In 2D nucleation, which occurs at a surface or interface, the chemical potential should decrease with increasing temperature according to the energetics based on thermodynamics [192,193]. The nucleation density typically decreases as the temperature increases [194]. In the cold-wall system for graphene nucleation and growth, the decomposition of ethanol increased with temperature. Although the surface with a higher temperature received more carbon adatoms from ethanol, the acceleration of carbon adatom desorption was more dominant for the overall nucleation process, resulting in a low nucleation probability. Thus, the nucleation density decreased, and the domain size increased with increasing temperature until CVD-G disappeared at 1300 °C, as demonstrated in the ST process (Figure 4.7).

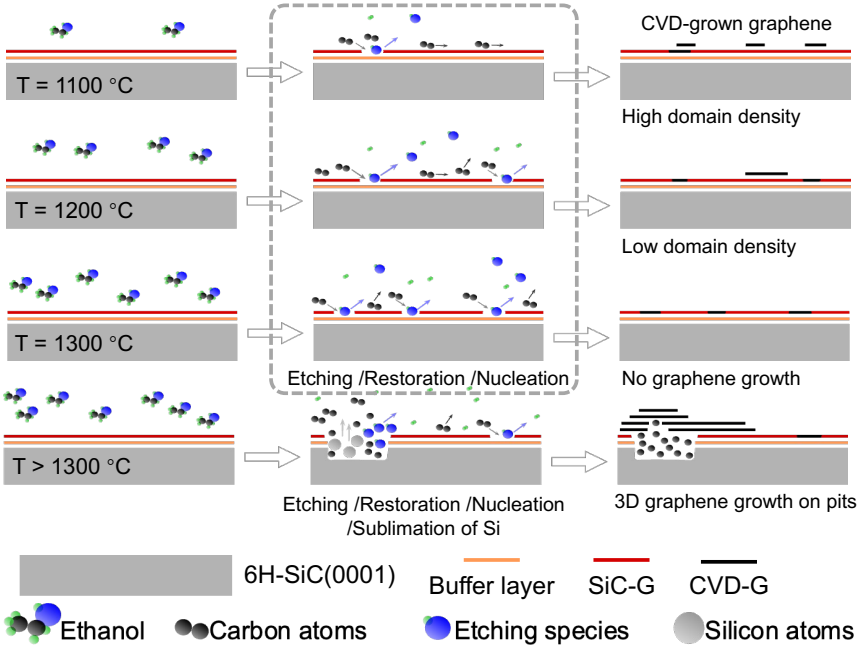

Figure 4.7 Schematic model of CVD-G growth at 1100, 1200, 1300, and >1300 °C for the ST process based on thermodynamics and the etching effect of ethanol decomposition.

However, at temperatures higher than 1300 °C, the appearance of CVD-G beyond the thermodynamic explanation led us to consider an additional mechanism. Previous studies of graphene growth on copper foils have reported the importance of etching effects [118,119], which induce a partial removal of graphene by the decomposition of ethanol molecules. The carbon atoms of ethanol also compensate for the removal, facilitating the restoration of the original graphene, and graphene nucleation occurs on the restored graphene. In our model, as the temperature rises in the cold-wall system, this decomposition of ethanol becomes more pronounced, subsequently elevating the concentrations of oxygen-containing species, such as H_2O and OH radicals, produced by ethanol decomposition [119]. These species play an active role in surface etching effects, inducing more defects in SiC-G. Consequently, there is an escalated requirement for supplementary carbon atoms to counterbalance the etching of SiC-G. Therefore, when the temperature exceeds the threshold, as depicted in the T > 1300 °C scenario in Figure 4.7,

the higher number of produced oxygen-containing species partially etch away SiC-G. Since the SiC substrate without a graphene cover sublimates as temperature increases [195], the sublimation of SiC occurs under the etched area of SiC-G.

In this scenario, we speculated that due to the inability of restoration to match the CVD-G removal of etching effects, when SiC sublimation is initiated, surface pits tend to develop. The decomposition of SiC leaves carbon atoms in the vicinity of the pits, resulting in a higher local concentration of carbon adatoms, which act as a carbon source for graphene growth. For the graphene domain shown in Figure 4.4(m), we estimated the volume of the pit part, and the graphene part based on the AFM morphology image and further calculated the number of carbon atoms corresponding to the volume to be 4.08×10^6 and 1.57×10^8, respectively, which are almost on the same order of magnitude. Therefore, we inferred that carbon atoms sublimating from pit regions participate in the local formation of multilayer CVD-G domains [196].

In section 3.4.1, we detailed how the temperature dependence of the ST process is affected by three key factors: the growth driving force, carbon source decomposition, and the instability of template morphology (see Table 4.1). Below 1300°C, the growth driving force plays a crucial role, with the nucleation density steadily decreasing as temperature rises. However, when the temperature surpasses 1300°C, the instability of the template's morphology takes precedence. Excessive etching of SiC leads to nucleation on rough-surfaced pits, resulting in the formation of island-like graphene.

Contrasting with the ST process, the AirE growth method operates under a lower ethanol partial pressure. This results in fewer ethanol decomposition products, which reduces the domination of instability of template morphology. Consequently, airborne contaminants that adhere to the step edges become the main factor for nucleation, explaining the localized nucleation seen in the AirE process. Conversely, the ST process effectively mitigates such localized nucleation. Nonetheless, it's clear that improvements in the process are necessary to better control nucleation, and specific strategies for this

will be explored in the next chapter.

		a) Growth driving force ($\boldsymbol{\Delta\mu_T}$)	**b)** Carbon source decomposition ($\boldsymbol{c_{precursor}}$)	**c)** Instability of template morphology ($\boldsymbol{c_{local}}$)
Higher temperature (T)		Lower $\Delta\mu_T$	Higher $c_{precursor}$	Higher c_{local}
Effect to nucleation		Nucleation suppression	Nucleation promotion	Local nucleation promotion
Chapter 3: Air-exposure (**AirE**) process	Result	**local nucleation** at higher T		
	Dominant factor	**b)** and **c):**By adsorbing air-contaminant on the step, the strained region becomes the most chemically active nucleation area.		
Chapter 4: Sequential thermal (**ST**) process	Result	**Nucleation suppression** (≤ 1300°C)	**Nucleation for island growth** (> 1300°C)	
	Dominant factor	**a)**	**c):** Excessive etching of SiC leads to nucleation occurring on pits with rough surface	

Table 4.1 Temperature-dependent nucleation determinants in ST and AirE processes.

4.7 Conclusion

An ST process was proposed to improve the growth of twisted graphene on graphene templates from SiC without a metal catalyst. By changing the degree of ethanol decomposition, which was controlled by adjusting the partial pressure of ethanol or the temperature of the substrate, different growth behaviors of graphene were observed in the ST and AirE processes. The growth of large-domain layer-by-layer tFLG relies on nucleation with a uniformly low density. In this regard, the ST process with a clean surface is a key step to effectively prevent locally high-density nucleation. Raman spectroscopy verified the high ratio of the twisted structure of graphene grown in the ST process. By investigating the temperature dependence of the ST process, we found that all trends in height, domain radius, and nucleation density were interrupted at 1300 °C. This disappearance suggests that the dominant mechanisms are different at temperatures below and above 1300 °C. We presented a model incorporating the etching effects of surface graphene, SiC-G restoration, and CVD-G growth to explain the unexpected growth at higher temperatures. This research contributes to a fundamental understanding of the tFLG growth mechanism, and the low nucleation density observed in this study is

expected to be advantageous for the development of large-scale tFLG synthesis and functional graphene devices.

Chapter 5. CO_2-assisted nucleation of twisted graphene on graphene/SiC templates

5.1 Background

tFLG is theoretically predicted to exhibit linear electronic band dispersion near the Fermi level. This is due to weak interlayer coupling, which resembles the massless fermions found in monolayer graphene [5,134,133]. This unique band structure allows tFLG to demonstrate electronic and optical properties similar to those of monolayer graphene. These properties include high electron mobility [197], quantum Hall effects [198], high transparency in the visible spectrum [14], tunable infrared light absorbance [199] and photoresponse up to the THz frequency range [200]. Furthermore, the few-layer stacked structure of tFLG effectively reduces the impact of charge impurities [136] and surface roughness [137,138] through a screening effect. This provides a beneficial approach to mitigating the extreme sensitivity of the electronic band structure in monolayer graphene to environmental factors. As a result, tFLG has garnered interest for its potential to translate the advantageous properties of monolayer graphene into practical device applications. Consequently, developing a system that enables the high-quality and large-scale synthesis of tFLG is highly desirable.

The transfer of monolayer graphene prepared by a mechanically exfoliation [10] and a CVD on transition metals [95] is commonly used for fabricating tFLG. Although mechanically exfoliated single-layer graphene with multiple transfers can precisely control the twist angle, the graphene size is limited and cannot be applied to practical production. In contrast, CVD uses transition metal foil as a catalytic surface, which is advantageous for achieving large-area scalable graphene growth. Both methods require transferring graphene onto an insulating substrate for performance characterization and electronic device applications. However, residual contamination [84,201], surface wrinkles [202,203] and sample breakage [84] from the transfer process extremally degrade the performance of graphene-based devices.

Recently, we introduced a method for preparing tFLG on graphene templates using a

catalyst-free CVD process [139,140,152,172]. This method utilizes ethanol as a carbon source to address problems related to surface mediation and self-limitation [118,119]. In this direct growth process, the carbon source generates graphene flakes in the gas surrounding the hot substrate, resembling the critical-size nuclei described in classical nucleation theory [123]. Without metal catalysis to reduces disorder at a lower energy levels [126], a higher temperature (above 2000°C) is necessary to reorient and align the layers effectively [125]. Furthermore, we successfully synthesized tFLG using a completely transfer-free CVD method on large-area monolayer graphene, which was produced through the thermal decomposition of SiC-G [172]. To enhance the uniformity and crystallinity of the resulting few-layer graphene, we proposed a sequential thermal (ST) process to reduce the local nucleation caused by step strain of SiC-G [204]. Due to the evident adhesion of airborne contaminants to SiC-G prepared by thermal decomposition, such contamination acts as a trigger for local nucleation during the CVD growth stage [178,205]. Therefore, our previous study combines two distinct steps—the epitaxial growth of SiC-G and the CVD growth of tFLG—within the same reaction chamber. The cooling process between these steps is conducted under a vacuum of approximately 1 Pa, ensuring that the SiC-G surface remains relatively clean.

Nucleation on a clean pristine graphene surface is less favorable compared to transition metal [112], oxide surfaces [121,141,206] and air-exposed SiC-G [178]. This is primarily due to the weak van der Waals interactions that cause carbon precursors and the small graphene flakes to desorb, reducing the probability of nucleation. Consequence, establishing a stable nucleation site requires overcoming a higher energy barrier. Although increasing the nucleation driving force by supplying additional carbon during the CVD process can help overcome this barrier, it tends to promote nucleation on the newly grown graphene rather than encouraging lateral layer-by-layer growth [180]. One effective strategy to tackle this issue is introducing defects. Single-vacancy defects or larger holes created by removing multiple atoms with dangling bonds should enhance the

adsorption of gas molecules [207]. The desorption of small graphene flakes is prevented, enabling them to serve as stable nuclei. As a result, the nucleation energy barrier can be lowered, which facilitates a more controlled and efficient growth process.

In this study, we proposed an effective method to create active sites on a clean graphene template, enabling layer-by-layer growth under low driving forces. The approach involves the reaction between CO_2 and graphene at high temperatures to produce CO [208], which facilitates the controlled etching of the SiC-G surface and creates activation sites for subsequent CVD growth of additional graphene layers (Figure 5.1(a)). Specifically, we introduced a CO_2 etching stage between the SiC-G growth stage and CVD-G growth stage, ensuring that no air exposure occurred throughout the procedure. This CO_2-assisted process formed activation sites on the SiC-G surface, promoting CVD-G nucleation. Our analysis revealed that the extent of etching depended on the etching conditions, and we identified optimized parameters to effectively promote the growth of monolayer graphene sheets. Furthermore, we confirmed regrowth of SiC-G during the CVD growth stage and introduced a CO_2-assisted nucleation model. This new model builds upon the previously proposed growth model [204] of CVD-G on SiC-G, systematically explaining the mechanisms of CO_2-assisted nucleation and growth.

5.2 Experiment design

The preparation of twisted graphene, as illustrated in Figure 5.1(b), involves three main growth stages: the SiC-G growth stage, the CO_2 etching stage of SiC-G, and the CVD-G growth stage. In the SiC-G growth stage, we utilized the ST process to produce SiC graphene with a clean surface, as previously reported. This was achieved through the thermal decomposition method, which allowed for the epitaxial growth of the 6H-SiC(0001) surface at 1700 °C, resulting in a monolayer template of graphene. Next, during the CVD growth stage, we incorporated a pretreatment step known as the CO2

etching stage of SiC-G. The impact of CO_2 during the etching process was examined by varying the temperature from 1130°C to 1200°C, at a pressure of 80 kPa and duration of 1 minute. We conducted screening test to optimize both the pressure and etching time, exploring ranges from 1.6 to 80 kPa and 1 to 30 minutes. In the CVD-G growth stage, all samples were synthesized with twisted graphene layers on the etched SiC-G templates. This was done by flowing an ethanol/argon mixture (typically 1 sccm/700 sccm) under a total pressure of 5 kPa, corresponding to an ethanol partial pressure of 7.1 Pa to a low nucleation driving force. Compared with our previous study [172], this is a low partial pressure that is favorable for the lateral growth of graphene. However, in previous reports, no graphene growth was observed at this partial pressure due to the small number of nucleation sites on the ST surface [204]. All high temperature treatments were performed using an infrared heating furnace (SR1800G, Thermo Riko).

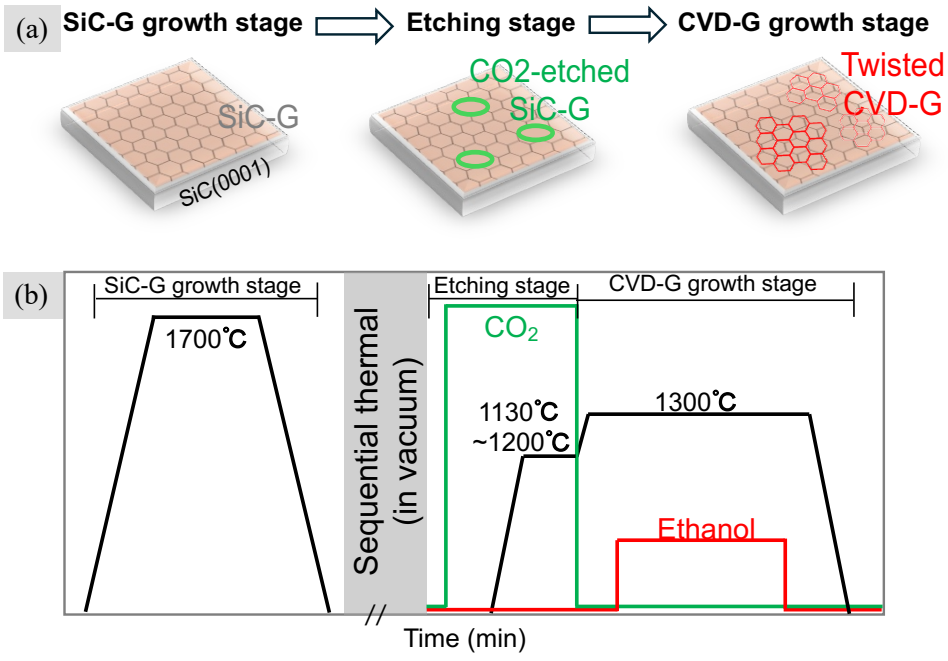

Figure 5.1 (a) Schematic diagram for SiC-G growth, etching and CVD-G growth stages. (b) Temperatures and gases used in the CO_2-assisted graphene synthesis process.

The etched SiC-G and the as-grown CVD-G were characterized using various analytical techniques. Atomic force microscopy (AFM) observations were performed in dynamic force mode under atmospheric conditions at room temperature to obtain morphology and phase images. Scanning electron microscopy (SEM) was employed to further confirm the morphology of both the etched SiC-G and as-grown CVD-G, using a Hitachi S-4800 SEM at acceleration voltage of 1.0 kV. To analyze the layer number and twisted structure of CVD-G, a Raman spectrometer (Horiba) with 532 nm laser excitation and a 100x objective was used (typical spot diameter: ~1 μm). The spectra were processed to subtract the contribution from the SiC substrate using a previously developed method [179,209]. The Raman spectra presented in this study were normalized to the characteristic peaks of the SiC substrate.

5.3 Etching effect of CO_2-assisted nucleation

This study aimed to investigate the effect of CO_2 as an etchant on clean SiC-G surfaces. To ensure consistency, the processing conditions for both the SiC-G and CVD-G growth stages were maintained across three preparation stages, with only the CO_2 etching conditions for SiC-G being varied. As shown in Figures 5.2(a)-(e), etching was performed at temperatures ranging from 1130 to 1200 °C to adjust the reactivity between CO_2 and the graphene surface.

No noticeable etching or CVD-G growth occurred at temperatures below 1130 °C. Increasing the temperature to 1150 °C created active sites that facilitated monolayer CVD-G grown on the surface (Figure 5.2(b), Type 1). At 1170 °C, the density of graphene growth sites increased. However, at higher temperatures, stronger etching effects were observed, leading to the formation of a different type of activation site (Figure 5.2(c), Type 2). Unlike Type 1, which corresponds to single nucleation sites, Type 2 is formed by the creation of undesired holes, resulting in multiple nucleation sites. The

CVD-G growth associated with these multiple nucleation sites typically occurs along the edges of the undesired holes, utilizing the unetched SiC-G regions as a template for growth. As shown in the two cross-sectional images in Figure 5.2(d), the green line indicates the edge of the etched SiC-G, which exhibits a height difference of approximately 0.35 nm. In contrast, the white line represents the edge of the grown CVD-G, showing a height difference of about 0.71 nm on the left and approximately 0.35 nm on the right. At elevated temperature, exceeding 1180 °C, the proportion of undesired holes increased, ultimately suppressing the graphene growth that was initiated by multiple nucleation sites (see Figures 5.2(d) and (e)). Figure 5.2(f) illustrates the distribution of Type 1 and Type 2 activation sites across different temperatures, based on data from 15 randomly selected AFM images. The counting criteria for Type 1 and Type 2 activation sites are provided in the inset of Figure 5.2(f). For Type 2, a single undesired hole created by multiple nucleation sites was counted as one site. Figure 5.2(g) presents the size distribution of undesired holes, demonstrating that higher temperatures lead to larger etching holes, a trend that is exacerbated by the merging of adjacent holes. We concluded that optimal etching conditions promote the formation of growth sites for CVD-G, allowing new graphene layers to develop at the active edges of the etched regions, with the unetched areas function as a template. However, aggressive etching increased the probability of undesired hole formation.

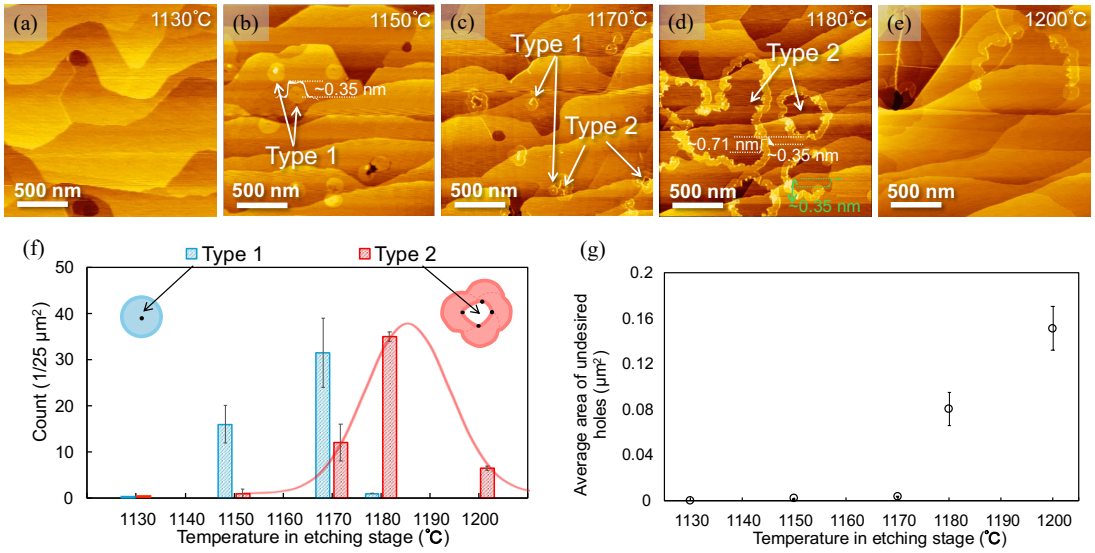

Figure 5.2 (a–e) AFM images of samples observed after CVD growth, with the etching stages performed at 1130°C, 1150°C, 1170°C, 1180°C, and 1200°C, respectively. (f) Statistical distribution of single nucleation sites (Type 1) and undesired holes formed by multiple nucleation sites (Type 2) from 12 sets of AFM images at each temperature: 1130°C, 1150°C, 1170°C, 1180°C, and 1200°C. (g) Temperature dependence of the average area of undesired holes formed by multiple nucleation sites (Type 2) shown in Figure (f).

In the screening experiments, a wide range of pressures and etching times were tested during the SiC-G etching stage to determine the optimal conditions, as detailed in the Figure 5.3. The results showed that increasing the CO_2 concentration enhanced its activity and increased the number of etched sites. Additionally, reducing the etching time helped prevent the expansion of undesired holes. Under the optimal etching conditions of 80 kPa and 1 minute and 1150°C, monolayer growth of CVD-G on SiC-G terrace was successfully achieved.

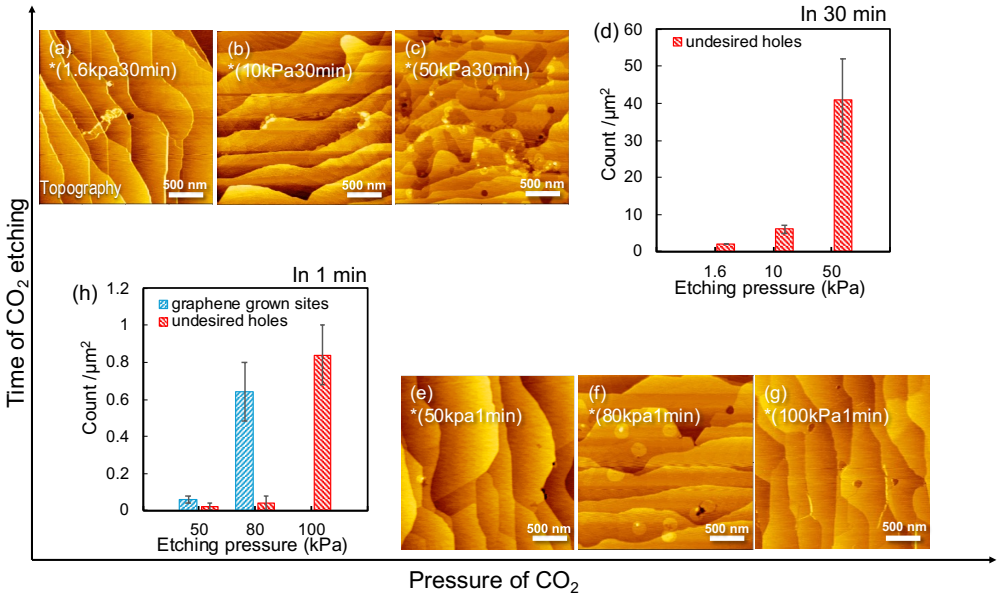

Figure 5.3 AFM images of samples observed after CVD growth, with the etching stages performed at 1150°C in 30 min in (a) 1.6 kPa, (b) 10 kPa, and (c) 50 kPa, respectively. (d) CO_2 pressure dependence of distribution of undesired holes from 8 sets of AFM images. AFM images of samples observed after CVD growth, with the etching stages performed at 1150°C in 1 min in (e) 50 kPa, (f) 80 kPa, and (g) 100 kPa, respectively. (h) CO_2 pressure dependence of distribution of graphene grown sites and undesired holes from 8 sets of AFM images.

5.4 Regrowth of graphene/SiC in CVD growth stage

We hypothesized that the active sites may be due to vacancy defects generated during the etching process. To confirm the defect structure formed in SiC-G during etching, etched SiC-G was directly observed after etching under optimized conditions of 80 kPa for 1 minute at 1150°C, without the CVD-G growth stage. However, upon examining the surface structure of etched SiC-G (Figure 5.4(a) and (b)), we remarkably observed large-scale graphene etching at the macroscopic scale. The retained SiC-G and etched regions are highlighted in both the morphology image (Figure 5.4(a)) and the phase image (Figure

5.4(b)). The etched regions in the morphology image were further confirmed by the cross-sections. For instance, the cross-section along the L-L' line (Figure 5.4(d)) clearly demonstrates that the monolayer-height graphene has been etched, corresponding to the

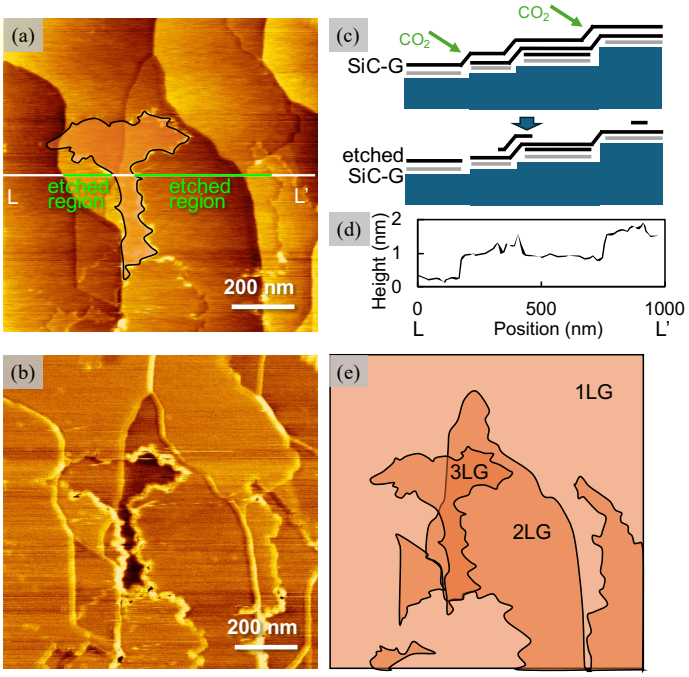

green segment of the L-L' line. Figure 5.4(e) illustrates the layer count and overlapping configuration of the retained SiC-G. In the phase image, the bright areas indicate etched SiC-G or the original monolayer SiC-G (1LG), while the dark areas represent retained bilayer (2LG) or trilayer SiC-G (3LG). This observation aligns with the morphology observations. As illustrated in Figure 5.4(c), it is inferred that regions primarily consisting of bilayer or trilayer SiC-G were etched following the CO_2 treatment. During the thermal decomposition growth of SiC-G, localized regions can develop 2–3 layers of graphene through a bottom-up growth mode, while the surface layer remains continuous [210]. Consequently, the distribution of retained SiC-G is utilized to understand the etching behavior of CO_2. Figure 5.4(c) clearly illustrates the state of retained SiC-G before and after the etching process, corresponding to the cross-section along the L-L' line in Figure 5.4(a).

Figure 5.4 AFM (a) topography image and (b) phase image observed after etching stage, at 1150°C and 80 kPa in 1 min. (c) Schematic model of etching of the changes of SiC-G

before and after etching, corresponding to the line segment L-L' shown in (a). (d) Cross-sectional view of the line segment L-L' shown in (a). (e) Schematic diagram of the layer number of retained SiC-G.

To clarify the relationship between the stages before and after etching, supplementary Figure S2 presents AFM images comparing samples processed during the SiC-G growth stage, the optimized etching stage, and the CVD-G growth stage. For samples treated after the etching stage (Figure 5.5(d) and (e)), there is a noticeable reduction in the coverage of 2LG and 3LG compared to those from the SiC-G stage (Figure 5.5(a) and (b)). In contrast, following the CVD-G growth stage (Figure 5.5(g) and 5.5(h)), the coverage of 2LG and 3LG increases, suggesting that the etched areas experienced significant regrowth during the CVD-G process. In these regions, a layer of CVD-G is observed to grow on the surface of the regrown 2LG areas. The etching and regrowth behaviors of SiC-G were further confirmed by SEM observations (Figure 5.5(c), (f), (i)). The areas with gray contrast indicate the presence of graphene, with darker shades representing a higher number of graphene layers [211]. Figure 5.5(f) shows the etched SiC-G, while Figure 5.5(i) illustrates the regrowth after CVD growth. The circular area with darker gray contrast, marked by an arrow in Figure 5.5(i), indicates the presence of a CVD-grown graphene domain. The results of SEM are consistent with those of AFM.

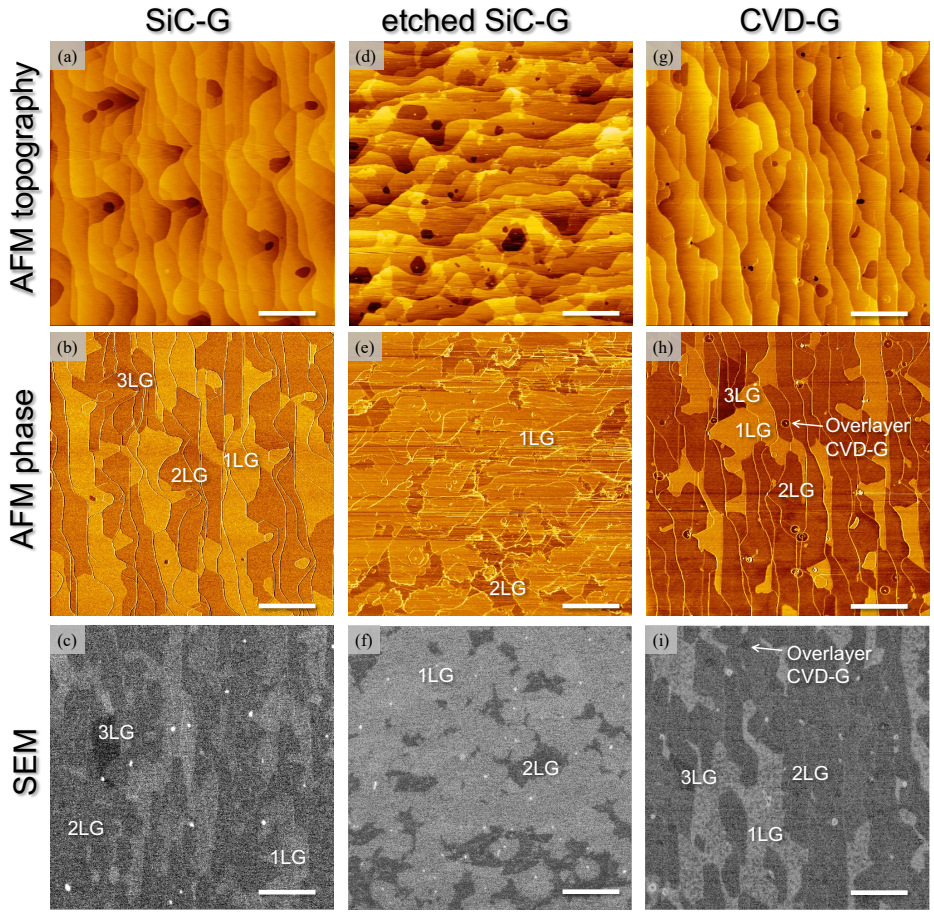

Figure 5.5 AFM topography, AFM phase and SEM (V_{acc} = 1kV, WD = 8.4mm) images of samples in (a-c) SiC-G growth stage, (d-f) optimized etching stage and (g-i) CVD-G growth stage. The scale bar in the figures indicate length of 1 μm.

A further evaluation of graphene structures across the three stages was conducted using Raman spectroscopy. Figure 5.6(a) presents the representative Raman spectra for the three stages, with all spectra normalized to the SiC substrate and substrate signals removed for clarity. The results indicate that the G band appears around 1600 cm^{-1}, corresponding to the in-plane stretching mode of the graphene hexagonal lattice, which confirms the growth of graphene. Figure 5.6(b) displays data from 15 random locations corresponding to the three stages. In comparison to the SiC-G template, the G band

intensity of etched SiC-G shows a noticeable reduction, along with an increased standard deviation across multiple samples. This variation is attributed to partial degradation of SiC-G (2LG and 3LG to 1LG) that occurs following the etching process. The intensity of CVD-G was approximately twice that of etched SiC-G and slightly higher than that of SiC-G. This increase can be attributed to the regrowth of etched SiC-G during CVD process, along with the growth of the overlayer CVD-G. The D band, which is located around 1380 cm^{-1}, did not show any significant changes (as seen in Figure 5.6(c), which is consistent with the data in Figure 5.6(d)). The very low intensity of the D band overlaps with the SiC characteristic peak, resulting in substantial noise even after substrate subtraction, which decreased the accuracy of the results.

Moreover, the etched SiC-G composed of macroscopic graphene flakes rather than point defects that would deactivate the hexagonal breathing mode. Consequently, no significant changes were observed in the D-band, which is typically associated with lattice defect activation. The G′ band located around 2730 cm^{-1}, exhibited variations in peak shape and intensity. Since the G′ band is sensitive to both the number of graphene layers and the twist angle, for twisted graphene, it can be fitted with a single Lorentzian curve that shows a blue shift relative to monolayer graphene [96,97]. Therefore, it can be indirectly inferred that the CVD-G, similar to our previous studies, exhibits a twisted structure, as indicated in Figure 5.6(d).

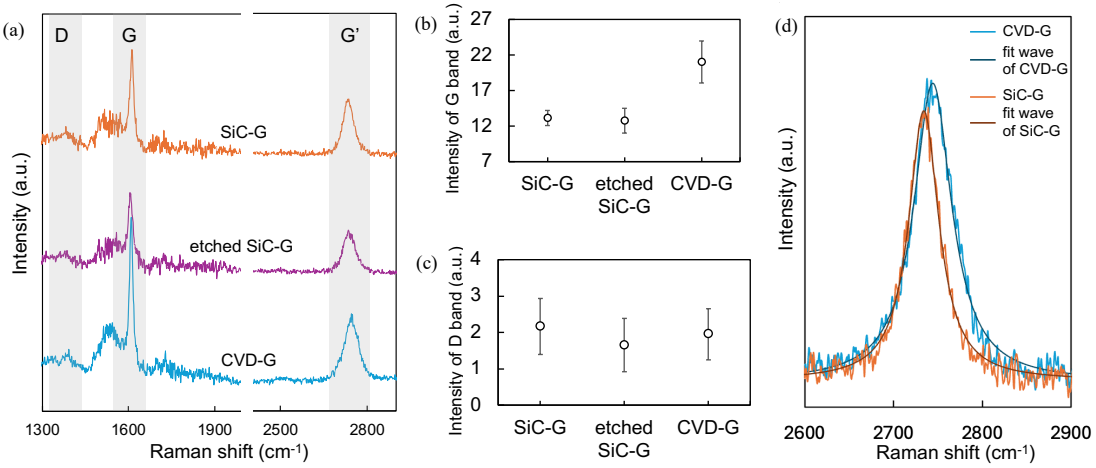

Figure 5.6 (a) Raman spectra (with 532 nm laser excitation) of SiC-G in SiC-G growth stage optimized etched SiC-G in etching stage and CVD-G in CVD-G growth stage. All these spectra are the results after subtraction of SiC substrate peaks and normalization. Normalized (b) G-band and (c) D-band intensities of SiC-G, etched SiC-G and CVD-G. (d) fitted Lorenz curves of G'-band in SiC-G and CVD-G.

5.5 Mechanism of CO_2-assisted nucleation

The results indicate that CO_2 significantly etches the SiC-G layer during the etching stage. Subsequently, in the CVD-G growth stage, the carbon source supplied first contributes to the regrowth of the etched SiC-G, creating activation sites on the regrown surface that facilitate the growth of the overlayer CVD-G. By analyzing the effects of temperature, CO_2 pressure, and etching time during the etching stage, we propose a growth mechanism in which CO_2 etches the template surface to promote overlayer growth. As shown in Figure 5.7(a), at lower temperatures and CO_2 pressures, the reaction rate between CO_2 and SiC-G is relatively low, resulting in minimal interaction or limited reaction with SiC-G. The limited reaction primarily occurs at the more reactive step edges, creating small etched holes after a short treatment. After the growth stage, these small etched holes do not provide enough activation sites for the overlayer CVD-G growth, as the lattice structure of rapidly regrown SiC-G remains largely intact. However, when treated for a longer duration, larger etched holes are formed. In this case, the regrowth of the etched SiC-G does not reach equilibrium with the overlayer growth before a complete SiC-G layer is formed, leading to the creation of undesired holes. These holes create multiple nucleation sites, resulting in monolayer graphene growth along their edges (corresponding to Type 2 in Figure 2).

At higher temperatures and pressures of CO_2 (see Figure 5.7(b)), CO_2 gas molecules have increased kinetic energy, enabling them to react more rapidly with the

solid graphene template. This enhanced reaction overcomes a high nucleation energy barrier present on the terraces of SiC-G, leading to the formation of etched holes on both the step edges and terraces. With a short etching time, the growth stage progresses more rapidly. As the regrowth of the etched SiC-G and the overlayer CVD-G growth reach equilibrium, activation sites are provided, allowing overlayer graphene to grow on the regrown SiC-G. However, with an extended CO_2 etching time, a significant number of undesired holes appear during the growth stage, resulting in only partial monolayer graphene forming along the edges of the holes. In contrast, during short CO2 etching, CVD-G grown from multiple nucleation sites fully encapsulates the holes. This discrepancy is due to the incomplete regrowth of SiC-G and the excessive consumption of the carbon source during the regrowth process.

In conclusion, a short treatment with a relatively high CO_2 reaction rate can effectively create active sites on the otherwise low-reactivity surface of the graphene template. These active sites are a result of carefully controlled etching of the SiC-G template by CO_2. This precise etching balances the regrowth of SiC-G with the growth of the CVD-G overlayer during the subsequent CVD-G stage, ultimately leading to the formation of a single nucleation site for the overlayer growth on the regrown SiC-G. However, the specific morphology of these active sites requires further investigation, such as in situ characterization. This is crucial because factors like the dangling bonds from vacancy defects, or the creation of new nucleation sites due to the clustering of carbon atoms during excessive regrowth, can effectively reduce the nucleation energy barrier. This reduction allows graphene clusters to adsorb more readily and act as nucleation sites for additional overlayer growth [123].

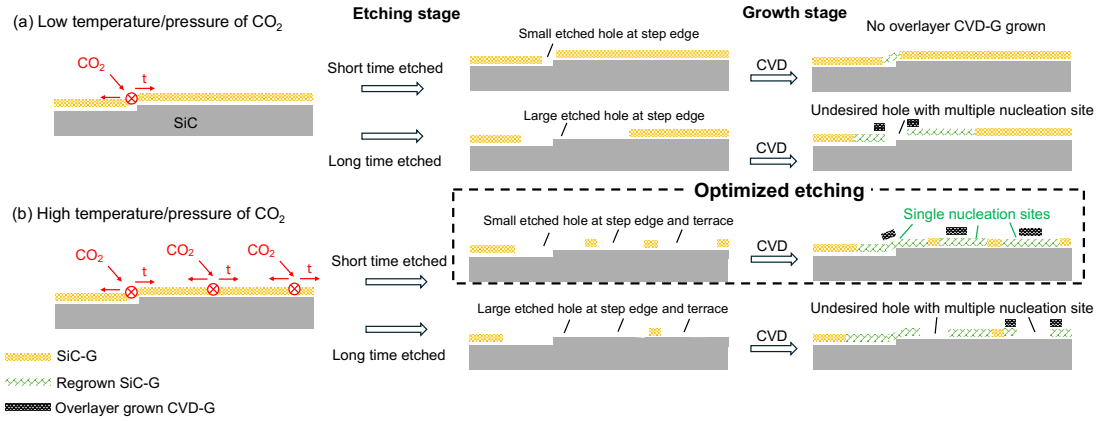

Figure 5.7 Schematic model of etching and CVD-G growth based on thermodynamics and reported research [118,204].

5.6 Etchant effect on CVD growth process

Beside the work of using CO_2 as an etchant to pre-treat SiC-G surfaces in the ST process, etchant effect during CVD growth were conducted and are described in this section. All the following CVD growth experiments were conducted in the ST process without air exposure.

Since there are few defects or dangling bonds on the surface of the SiC-G template in the ST process, it is challenging to spontaneously form additional graphene nuclei. A higher partial pressure of ethanol was employed to enhance the nucleation drive; however, this approach also leads to the formation of more vertically grown graphene islands, referred to as 3D component graphene in this section. To address this issue, CO_2 and H_2O are introduced as reactive etchants during the CVD-G growth stage, reacting with the excess carbon sources on the surface to ensure the lateral growth of graphene (Figure 5.8).

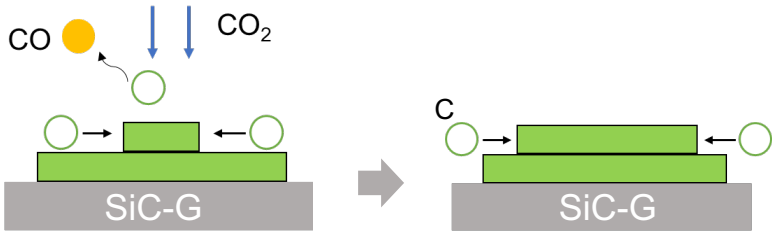

Figure 5.8 Simplified schematic diagram of the behavior of the etchant during CVD growth, exemplified by CO_2.

Figure 5.9 illustrates the effect of CO_2 as an etchant on the CVD process. By comparing the conditions without CO_2, it is concluded that a low concentration (flow rate < 10 sccm) of CO_2 reduces the proportion of 2D graphene, while a high concentration (flow rate > 10 sccm) of CO_2 increases the proportion of 2D graphene. This trend was also observed in the experimental groups with other conditions. However, the coverage rate remains unaffected and stays at 50%.

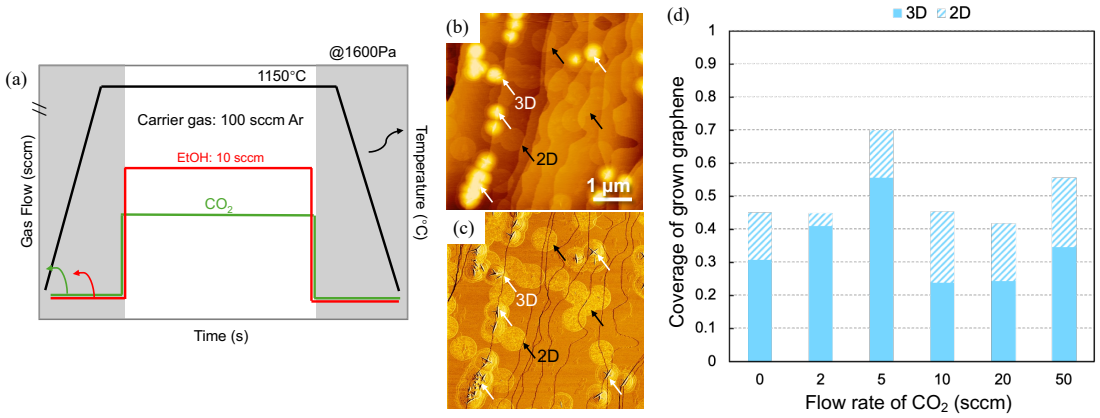

Figure 5.9 (a) Schematic diagram for CVD-G growth with CO_2 in ST process. A typical topography (b) and phase image (c) of AFM result. 3D graphene and 2D graphene are indicated by white and black arrows, respectively, in (b) and (c). (d) Coverage statistics under different CO_2 flow rates.

Figure 5.10 illustrates the effect of H_2O as an etchant on the CVD process. Although the growth conditions have been adjusted, H_2O is much more aggressive in etching compared to CO_2. This results in a drastic etching of the already grown graphene. As shown in Figure 5.10(b) and (c), the layered structure of the graphene is destroyed. Therefore, we concluded that H_2O is not the etchant we are looking for.

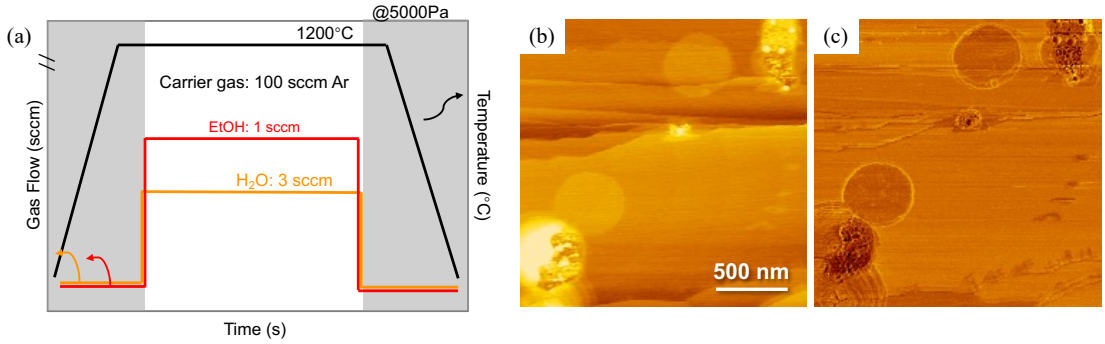

Figure 5.10 (a) Schematic diagram for CVD-G growth with H_2O in ST process. A typical topography (b) and phase image (c) of AFM result.

5.7 Two-stage growth of twisted graphene

In this subsection, two primary two-stage growth methods are proposed: the pulsed two-stage growth method and the temperature-regulated two-stage growth method. In both approaches, the first stage generates sufficient driving force for graphene nucleation, while the second stage reduces the driving force to ensure an appropriate carbon source supply for the lateral growth of graphene.

Figure 5.11(a) drafts the gas flow and temperature profiles of the pulsed two-stage growth method, while Figure 5.10(d) presents three schemes for adjusting the pulse stage (the first stage) conditions as typical examples of this method. The pulse settings are as follows: Pulse 1 uses 133 Pa ethanol for 1 minute, Pulse 2 uses 133 Pa ethanol for 5

minutes, and Pulse 4 uses 246 Pa ethanol for 1 minute. The total reaction time is 60 minutes, with an ethanol partial pressure of 13.3 Pa during the growth phase. A standard control experiment was conducted with a growth stage that excludes the pulse phase. The results indicate that the pulsed two-stage growth method can enhance the coverage of graphene but does not lead to any significant improvement in increasing the proportion of 2D graphene.

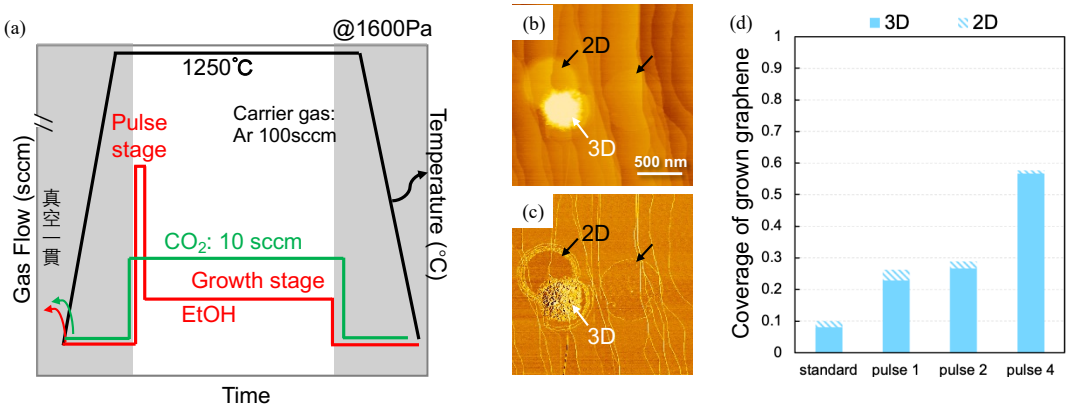

Figure 5.11 (a) Schematic diagram for pulsed two-stage growth method with pulse stage and growth stage noted. A typical topography (b) and phase image (c) of AFM result. 3D graphene and 2D graphene are indicated by white and black arrows, respectively, in (b) and (c). (d) Coverage statistics under different pulse conditions.

Figure 5.12 illustrates the temperature-regulated two-stage growth method. In gas-solid reaction systems, the phase equilibrium relationship shows that below the temperature corresponding to sublimation energy, a lower temperature results in a higher driving force for nucleation. Therefore, during the nucleation range on the graphene template (>900°C), the probability of graphene nucleation is increased by lowering the temperature in the first growth stage. Different temperature combinations are presented in Figure 5.12(d). The reaction time for the low-temperature stage (first stage) is 10 minutes, and for the high-temperature stage (second stage) is 15 minutes. The results

indicate that the combination of 1000°C in the low-temperature stage and 1300°C in the high-temperature stage achieves the best coverage and the highest proportion of 2D graphene.

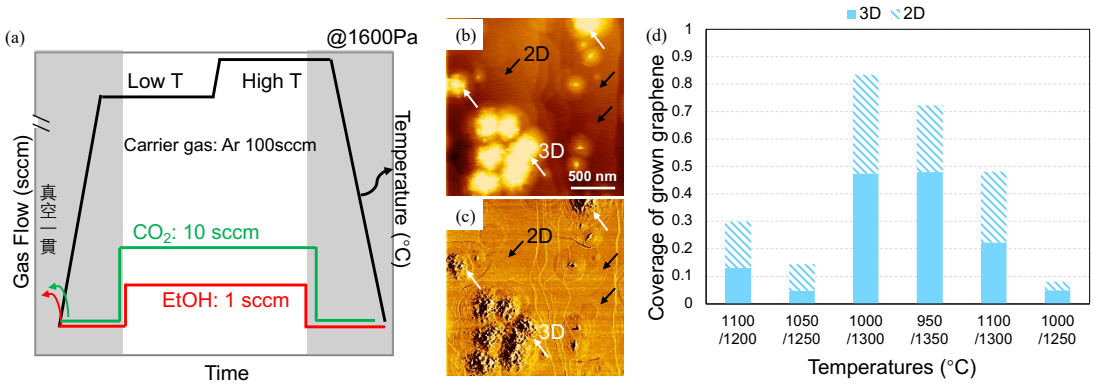

Figure 5.12 (a) Schematic diagram for CVD-G growth with low-temperature (Low T) stage and high-temperature (High T) stage. A typical topography (b) and phase image (c) of AFM result. 3D graphene and 2D graphene are indicated by white and black arrows, respectively, in (b) and (c). (d) Coverage statistics under different set of temperatures (Low T /High T).

Since the cold-wall system of the IR furnace thermally decomposes the carbon source gas primarily near the substrate, temperature adjustments also influence the carbon source concentration provided by ethanol. To optimize the temperature-regulated two-stage growth method, the ethanol concentration is appropriately increased during the low-temperature stage (first stage). The optimization results are shown in Figure 5.13, illustrating the enhancement of this increased ethanol concentration on the lateral growth of 2D graphene.

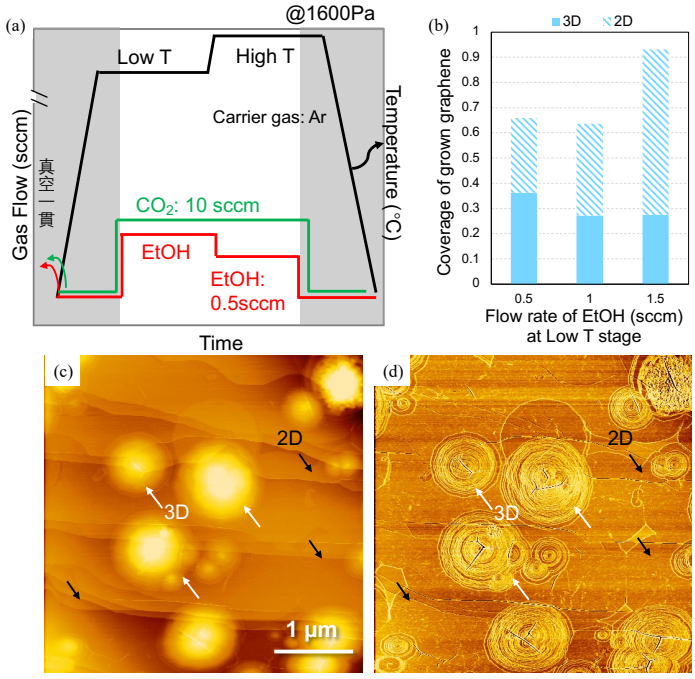

Figure 5.13 (a) Schematic diagram for CVD-G growth with low-temperature (Low T) stage with higher concentration of ethanol and high-temperature (High T) stage lower concentration of ethanol. (d) Coverage statistics under different ethanol flow rate at Low T stage. A typical topography (b) and phase image (c) of AFM result. 3D graphene and 2D graphene are indicated by white and black arrows, respectively, in (b) and (c).

Through a series of experiments, it was demonstrated that while the etching effect of CO_2 effectively suppresses island-like growth, eliminating this phenomenon through adjustments to growth parameters and process improvements is still challenging. This limitation is unfavorable for achieving layer-by-layer growth. Consequently, it was concluded that promoting nucleation during the pre-treatment stage is the most effective strategy for achieving layer-by-layer growth of graphene. This study provides new insights into extending the layer-by-layer CVD growth of graphene templates with CO_2 assistance. We eagerly anticipate further in-depth research to advance the development of graphene-based technologies.

5.8 Conclusion

A method for CO_2-assisted nucleation on clean graphene/SiC templates was proposed. Incorporating CO_2-etching stage in a sequential thermal process to etch graphene/SiC in a vacuum facilitated nucleation during the CVD growth stage. Through examining the temperature dependence of the CO_2 etching, we observed that weak etching fails to promote nucleation, while overly aggressive etching results in undesired holes rather than effective nucleation sites. Single nucleation sites of graphene growth were observed under appropriate etching conditions, 1150°C, 80 kPa, 1 min. Monolayer graphene was grown, forming a twisted structure with the template graphene/SiC, as confirmed by Raman spectroscopy. Additionally, observations of the etched graphene/SiC revealed that regrowth occurred during the CVD growth stage. Consequently, we proposed that the graphene nucleation sites were induced by the balance between the regrowth of the etched graphene/SiC and the nucleation of the overlayer graphene. This process ultimately results in an almost completely regrown graphene/SiC layer and the growth of the overlayer graphene. It is worth noting that we previously reported that in the sequential thermal process [204], monolayer CVD-G is unable to nucleate on a clean graphene/SiC surface. This CO_2-assisted nucleation method successfully overcomes this issue. Additionally, the findings on the etchant effects in the CVD growth process and results from the two-stage growth of twisted graphene, offering an effective method for the uniform synthesis of large-area tFLG. Therefore, this research provides a crucial groundwork for the CVD-based overlayer growth and scalable production of twisted graphene, paving the way for exploring its unique physical properties and advanced applications in electronic and optoelectronic devices.

Chapter 6. Conclusion and future perspective

To fully harness the high performance of graphene in macroscopic devices, it was essential to develop a method for synthesizing randomly stacked twisted graphene, rather than conventional AB-stacked graphene, using the CVD method. This was because the strong interlayer interactions in AB-stacked graphene significantly diminished the exceptional properties of single-layer graphene. However, existing methods for obtaining randomly stacked tFLG on graphene templates often suffer from low crystallinity and/or poor uniformity of the few-layer structures.

To address these challenges, this study adopted a process for growing tFLG on graphene/SiC templates (Chapter 3). Furthermore, a continuous heat treatment method was proposed to enhance crystallinity by effectively suppressing graphene nucleation (Chapter 4). Finally, to enable layer-by-layer growth, a CO_2-assisted nucleation method was introduced, which successfully synthesized single-layer graphene cores (Chapter 5).

In Chapter 3, the overlayer growth of graphene on epitaxial graphene/SiC using ethanol CVD without a metal catalyst was systematically studied across a wide temperature range (900 °C to 1450 °C). The lateral and vertical growth behaviors, as well as the structures of the grown graphene, were analyzed using AFM and STM observations. Structural analyses revealed that graphene islands grown at 1300 °C form hexagonal twisted bilayer graphene as single crystals, whereas islands grown at higher temperatures (~1400 °C) consist of multiple domains with varied twist angles. At elevated temperatures, an unusual increase in nucleation density and the coalescence of circular graphene islands were observed, attributed to surface deformation under reactive conditions. Based on these observations and theoretical analysis of the formation mechanism of randomly twisted structure and their temperature dependence, a growth model was proposed that correlates crystallinity (amorphous, single-crystalline, and polycrystalline) and layer numbers (monolayer and few-layer) with growth temperature and time. These findings provided a pathway for optimizing growth conditions to produce defect-free, single-

crystalline monolayer and few-layer graphene while minimizing the impact of macrostructural defects such as wrinkles that compromised structural uniformity.

In Chapter 4, the ST process was introduced to suppress the local nucleation of twisted graphene on graphene/SiC templates. By manipulating ethanol decomposition through adjustments in partial pressure and substrate temperature, contrasting growth behaviors were observed between the ST and AirE processes. The ST process, characterized by its clean surface, effectively suppressed high-density nucleation and enabled the overlayer growth of large-domain tFLG. Raman spectroscopy confirmed the high proportion of twisted structures in graphene grown through this process. Furthermore, temperature-dependent studies revealed distinct growth mechanisms below and above 1300 °C, with key trends in height, domain size, and nucleation density disrupted at this threshold. A model was proposed to explain these phenomena, incorporating the etching effects on surface graphene, SiC-G restoration, and CVD-G growth. These insights deepen the understanding of tFLG growth mechanisms and demonstrate the potential of the ST process for scalable synthesis of high-quality twisted graphene.

In Chapter 5, a CO_2-assisted nucleation method was developed to overcome challenges in CVD layer-by-layer growth on clean graphene/SiC templates. By incorporating CO_2 as an etchant during a sequential thermal process, nucleation was facilitated during the CVD growth stage. Temperature-dependent studies showed that mild etching was insufficient to promote nucleation, while excessive etching led to undesirable hole formation. Optimal conditions (1150 °C, 80 kPa, 1 min) allowed effective nucleation, as confirmed by Raman spectroscopy, with twisted monolayer graphene forming during the nucleation stage. Additionally, observations revealed a regrowth of SiC-G during the CVD growth, balancing etching-induced damage with SiC-G regrowth and overlayer nucleation. This method resolved prior challenges, the inability of monolayer CVD-G to nucleate on clean graphene/SiC surfaces, as previously discussed

in Chapter 4. Additionally, the findings on the etchant effects in the CVD growth process, along with the results from the two-stage growth of twisted graphene, provided an effective approach for the uniform synthesis of large-area tFLG. The CO_2-assisted nucleation method thus provides a robust foundation for scalable CVD-based layer-by-layer growth of twisted graphene.

In future work, it will be very important that the superior electronic performance of the tFLG grown on graphene/SiC should be explored extensively as already reported for the tFLG fabricated on the CVD-graphene [139]. The results of this work laid a solid foundation for mass production of tFLG grown on SiC graphene and provided ample opportunities for studies on the physical properties and applications of tFLG.

Appendix: Raman spectroscopy of graphene synthesized on SiC (0001)

During the thermal decomposition process of SiC (0001) to produce epitaxial graphene, a carbon-rich layer partially covalently bonded to the SiC substrate forms between the SiC and the graphene. This layer is referred to as the buffer layer. The presence of the buffer layer also contributes to the Raman spectrum of graphene, particularly in the 1200–1800 cm^{-1} range [146], where its signals overlap significantly with the graphene D-band and G-band. Therefore, when discussing changes in the intensity of the graphene G-band, the contribution of the buffer layer must be considered.

Referring to the method proposed by Wang et al. [209] for removing substrate background peaks, three steps were introduced to analyze the intensity of graphene characteristic peaks: baseline removal, substrate background removal, and buffer layer/graphene peak deconvolution.

1. Baseline removal: The Raman spectrum is averaged between 2010–2050 cm^{-1} and 3165–3265 cm^{-1} using to determine the baseline. Baseline removal is performed for both pristine SiC samples and processed SiC samples. Due to the complex processing of the SiC-G surface after thermal decomposition—such as additional CVD treatments—in this study, all samples with graphene on the SiC (including CVD-G and SiC-G) are collectively referred to as "processed SiC."
2. Substrate background removal: Using the SiC characteristic peaks between 1660–2000 cm^{-1}, a spectrum without contributions from the buffer layer or graphene is obtained. The pristine SiC spectrum is shifted and intensity-normalized to match the processed SiC spectrum. The normalized pristine SiC spectrum is then subtracted from the processed SiC spectrum, yielding the spectrum containing both buffer layer and graphene signals.
3. Buffer layer/graphene peak deconvolution: Following established methods [209,212], five Gaussian functions are used to fit the buffer layer and graphene G-band in the 1000–2000 cm^{-1} range. Figure A1 serves as an example, illustrating the spectral line

(green solid line) and the fitting results (black solid line) of the averaged Raman spectra of SiC-G in this study. The centers of the four Gaussian peaks corresponding to the buffer layer (red dashed lines) are located at 1351.1, 1505.3, 1549.6, and 1598.0 cm^{-1}, while the Gaussian peak center of the graphene G-band (red solid line) is at 1610.1 cm^{-1}. The spectral features of the buffer layer are consistent with those reported by Landois et al [212].

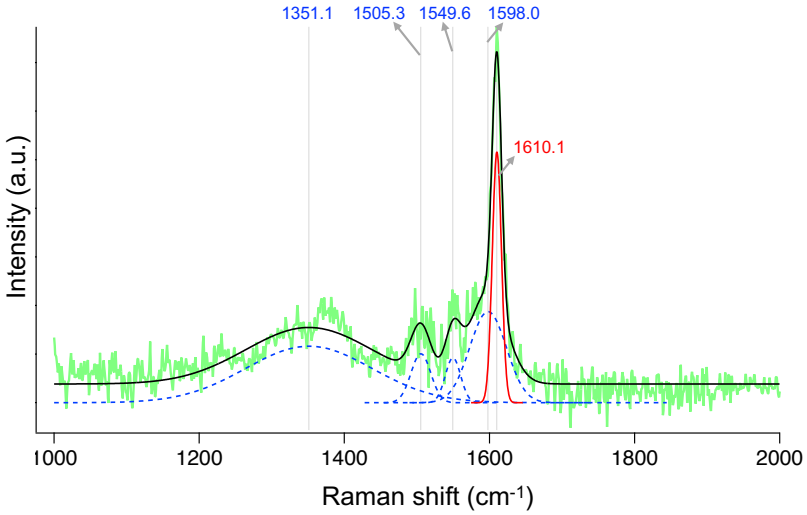

Figure A1 Representative Raman spectra of SiC-G, obtained after subtracting the SiC signal and fitting the buffer spectra separately from the G band.

Using this approach, the G-band and buffer layer contributions were separated. In this study, the relative intensity of the graphene G-band was characterized using the integral of the Gaussian peaks. The following table (Table A1) provides detailed information about the G-band intensities in the Raman spectra discussed in the main text, as presented in Figures 3.2, 4.3, 4.5, and 5.6. In cases where the CVD-grown graphene is a multilayer structure (with the G peak intensity exceeding more than five times that of monolayer graphene), the buffer layer may not be fit into four Gaussian peaks.

Gaussian centers, and integrated intensity of fitted Raman buffer layer signature (cm^{-1}, count/s)		G peak	Buffer peak 1	Buffer peak 2	Buffer peak 3	Buffer peak 4
Figure 3.2d	Before growth	1598.2, 408.8	1349.9, 349.5	1505.4, 190.9	1521.8, 14.8	1575.5, 408.8
	After growth	1602.1, 891.7	1354.2, 949.7	1504.7, 437.5	1550.1 60.1	1582.4, 572.3
Figure 4.3j	15 Pa ST	1604.9, 525.8	1366.7, 190.0	1510.5, 372.6	1538.9, 22.2	1567.9, 98.2
	15 Pa AirE	1604.2, 495.7	1353.3, 686.0	1494.4, 33.0	1514.3, 16.6	1584.6, 357.8
	53 Pa ST	1598.4, 598.6	1360.0, 391.3	1491.9, 69.0	1519.4, 37.8	1553.5, 339.4
	53 Pa AirE	1603.3, 1243.2	1362.6, 739.3	1496.1, 197.1	1524.0, 26.9	1552.3, 823.9
	105 Pa ST	1606.8, 2148.1	1355.3, 561.9	1493.5, 88.3	1563.3, 591.5	1596.0, 885.2
	105 Pa AirE	1597.9, 2681.9	1356.5, 1022.8	1502.5, 182.6	1525.7, 53.9	1556.6, 125.3
	530 Pa ST	1595.6, 31038.6	1355.3, 34081.2	1492.5, 2451.1	1525.1, 671.0	1541.1, 248.6
	530 Pa AirE	1590.8, 92364.6	1354.6, 64007.9	--	--	--
Figure 4.5a	SiC-G only	1599.3, 345.5	1355.8, 262.1	1505.8, 192.8	1563.1, 144.4	1602.7, 106.5
	1000 °C	1601.0, 558.7	1347.1, 331.9	1503.2, 103.6	1536.7, 15.1	1561.2, 101.7
	1100 °C	1601.6, 357.3	1334.8, 201.8	1492.9, 42.6	1547.4, 185.9	1595.5, 204.6
	1200 °C	1594.6, 2610.9	1362.5, 551.4	--	--	--
	1300 °C	1611.2, 549.0	1354.3, 682.4	1492.3, 52.3	1562.1, 118.3	1558.2, 35.7
	1400 °C	1603.6, 914.4	1359.3, 114.5	1496.0, 37.0	1560.0, 176.3	1591.2, 521.03
	1500 °C	1585.9, 4218.1	1352.4, 294.0	--	--	--
Figure 5.6a	SiC-G	1611.9, 392.8	1359.8, 420.6	1505.6, 191.7	1557.8, 287.7	1601.3, 26.7
	etched SiC-G	1606.4, 355.5	1354.9, 178.6	1498.3, 69.5	1524.2, 15.1	1552.8, 188.6
	CVD-G	1608.9, 627.7	1354.8, 408.3	1485.1, 17.5	1533.8, 563.0	1579.6, 26.7

Table A1 Detailed information on the fitting of the Raman G peak and the buffer layer spectral peak characteristics in this doctoral dissertation.

Reference

[1] K.S. Novoselov, A.K. Geim, S.V. Morozov, D. Jiang, Y. Zhang, S.V. Dubonos, I.V. Grigorieva, A.A. Firsov, Electric Field Effect in Atomically Thin Carbon Films, Science 306 (2004) 666–669. https://doi.org/10.1126/science.1102896.

[2] K.S. Novoselov, A.K. Geim, S.V. Morozov, D. Jiang, M.I. Katsnelson, I.V. Grigorieva, S.V. Dubonos, A.A. Firsov, Two-dimensional gas of massless Dirac fermions in graphene, Nature 438 (2005) 197–200. https://doi.org/10.1038/nature04233.

[3] A.C. Ferrari, J.C. Meyer, V. Scardaci, C. Casiraghi, M. Lazzeri, F. Mauri, S. Piscanec, D. Jiang, K.S. Novoselov, S. Roth, A.K. Geim, Raman Spectrum of Graphene and Graphene Layers, Phys. Rev. Lett. 97 (2006) 187401. https://doi.org/10.1103/PhysRevLett.97.187401.

[4] K. Kim, S. Coh, L.Z. Tan, W. Regan, J.M. Yuk, E. Chatterjee, M.F. Crommie, M.L. Cohen, S.G. Louie, A. Zettl, Raman Spectroscopy Study of Rotated Double-Layer Graphene: Misorientation-Angle Dependence of Electronic Structure, Phys. Rev. Lett. 108 (2012) 246103. https://doi.org/10.1103/PhysRevLett.108.246103.

[5] S. Latil, V. Meunier, L. Henrard, Massless fermions in multilayer graphitic systems with misoriented layers: Ab initio calculations and experimental fingerprints, Phys. Rev. B 76 (2007) 201402. https://doi.org/10.1103/PhysRevB.76.201402.

[6] S. Ha, N.H. Park, H. Kim, J. Shin, J. Choi, S. Park, J.-Y. Moon, K. Chae, J. Jung, J.-H. Lee, Y. Yoo, J.-Y. Park, K.J. Ahn, D.-I. Yeom, Enhanced third-harmonic generation by manipulating the twist angle of bilayer graphene, Light Sci. Appl. 10 (2021) 19. https://doi.org/10.1038/s41377-020-00459-5.

[7] P. Moon, M. Koshino, Optical absorption in twisted bilayer graphene, Phys. Rev. B 87 (2013) 205404. https://doi.org/10.1103/PhysRevB.87.205404.

[8] Y. Cao, V. Fatemi, S. Fang, K. Watanabe, T. Taniguchi, E. Kaxiras, P. Jarillo-Herrero, Unconventional superconductivity in magic-angle graphene superlattices, Nature 556 (2018) 43–50. https://doi.org/10.1038/nature26160.

[9] J.M. Park, Y. Cao, K. Watanabe, T. Taniguchi, P. Jarillo-Herrero, Tunable strongly coupled superconductivity in magic-angle twisted trilayer graphene, Nature 590 (2021) 249–255. https://doi.org/10.1038/s41586-021-03192-0.

[10] J.M. Park, Y. Cao, L.-Q. Xia, S. Sun, K. Watanabe, T. Taniguchi, P. Jarillo-Herrero, Robust superconductivity in magic-angle multilayer graphene family, Nat. Mater. 21 (2022) 877–883. https://doi.org/10.1038/s41563-022-01287-1.

[11] A.H. Castro Neto, F. Guinea, N.M.R. Peres, K.S. Novoselov, A.K. Geim, The electronic properties of graphene, Rev. Mod. Phys. 81 (2009) 109–162. https://doi.org/10.1103/RevModPhys.81.109.

[12] C.-H. Park, L. Yang, Y.-W. Son, M.L. Cohen, S.G. Louie, New Generation of Massless Dirac Fermions in Graphene under External Periodic Potentials, Phys. Rev. Lett. 101 (2008) 126804. https://doi.org/10.1103/PhysRevLett.101.126804.

[13] The rise of graphene | Nature Materials, (n.d.). https://www.nature.com/articles/nmat1849 (accessed November 17, 2024).

[14] R.R. Nair, P. Blake, A.N. Grigorenko, K.S. Novoselov, T.J. Booth, T. Stauber, N.M.R. Peres, A.K. Geim, Fine Structure Constant Defines Visual Transparency of Graphene, Science 320 (2008) 1308–1308. https://doi.org/10.1126/science.1156965.

[15] A.B. Kuzmenko, E. van Heumen, F. Carbone, D. van der Marel, Universal Optical Conductance of Graphite, Phys. Rev. Lett. 100 (2008) 117401. https://doi.org/10.1103/PhysRevLett.100.117401.

[16] F. Schwierz, Graphene transistors, Nat. Nanotechnol. 5 (2010) 487–496. https://doi.org/10.1038/nnano.2010.89.

[17] Y.-M. Lin, C. Dimitrakopoulos, K.A. Jenkins, D.B. Farmer, H.-Y. Chiu, A. Grill, Ph. Avouris, 100-GHz Transistors from Wafer-Scale Epitaxial Graphene, Science 327 (2010) 662–662. https://doi.org/10.1126/science.1184289.

[18] S.-L. Li, H. Miyazaki, A. Kumatani, A. Kanda, K. Tsukagoshi, Low Operating Bias and Matched Input−Output Characteristics in Graphene Logic Inverters, Nano Lett. 10 (2010) 2357–2362. https://doi.org/10.1021/nl100031x.

[19] F. Schedin, A.K. Geim, S.V. Morozov, E.W. Hill, P. Blake, M.I. Katsnelson, K.S. Novoselov, Detection of individual gas molecules adsorbed on graphene, Nat. Mater. 6 (2007) 652–655. https://doi.org/10.1038/nmat1967.

[20] F. Giannazzo, S.E. Panasci, E. Schilirò, A. Koos, B. Pécz, Integration of graphene and MoS2 on silicon carbide: Materials science challenges and novel devices, Mater. Sci. Semicond. Process. 174 (2024) 108220. https://doi.org/10.1016/j.mssp.2024.108220.

[21] C. Zeng, E.B. Song, M. Wang, S. Lee, C.M.Jr. Torres, J. Tang, B.H. Weiller, K.L. Wang, Vertical Graphene-Base Hot-Electron Transistor, Nano Lett. 13 (2013) 2370–2375. https://doi.org/10.1021/nl304541s.

[22] G. Fisichella, G. Greco, F. Roccaforte, F. Giannazzo, Current transport in graphene/AlGaN/GaN vertical heterostructures probed at nanoscale, Nanoscale 6 (2014) 8671–8680. https://doi.org/10.1039/c4nr01150c.

[23] G. Ruhl, S. Wittmann, M. Koenig, D. Neumaier, The integration of graphene into microelectronic devices, Beilstein J. Nanotechnol. 8 (2017) 1056–1064. https://doi.org/10.3762/bjnano.8.107.

[24] M. Kuwabara, D.R. Clarke, D.A. Smith, Anomalous superperiodicity in scanning tunneling microscope images of graphite, Appl. Phys. Lett. 56 (1990) 2396–2398. https://doi.org/10.1063/1.102906.

[25] E.J. Mele, Novel electronic states seen in graphene, Nature 556 (2018) 37–38. https://doi.org/10.1038/d41586-018-02660-4.

[26] K. Kim, A. DaSilva, S. Huang, B. Fallahazad, S. Larentis, T. Taniguchi, K. Watanabe, B.J. LeRoy, A.H. MacDonald, E. Tutuc, Tunable moiré bands and strong correlations in small-twist-angle bilayer graphene, Proc. Natl. Acad. Sci. 114 (2017) 3364–3369. https://doi.org/10.1073/pnas.1620140114.

[27] T. Kato, Direct observation of nucleation dynamics for atomically thin layered 2D semiconductor material, JSAP Rev. 2024 (2024). https://doi.org/10.11470/jsaprev.240410.

[28] T. Ohta, A. Bostwick, T. Seyller, K. Horn, E. Rotenberg, Controlling the Electronic Structure of Bilayer Graphene, Science 313 (2006) 951–954. https://doi.org/10.1126/science.1130681.

[29] E. McCann, M. Koshino, The electronic properties of bilayer graphene, Rep. Prog. Phys. 76 (2013) 056503. https://doi.org/10.1088/0034-4885/76/5/056503.

[30] J. Hass, F. Varchon, J.E. Millán-Otoya, M. Sprinkle, N. Sharma, W.A. de Heer, C. Berger, P.N. First, L. Magaud, E.H. Conrad, Why Multilayer Graphene on 4H-SiC(000-1) Behaves Like a Single Sheet of Graphene, Phys. Rev. Lett. 100 (2008) 125504. https://doi.org/10.1103/PhysRevLett.100.125504.

[31] J.C. Rode, D. Smirnov, H. Schmidt, R.J. Haug, Berry phase transition in twisted bilayer graphene, 2D Mater. 3 (2016) 035005. https://doi.org/10.1088/2053-1583/3/3/035005.

[32] G. Trambly de Laissardière, D. Mayou, L. Magaud, Localization of Dirac Electrons in Rotated Graphene Bilayers, Nano Lett. 10 (2010) 804–808. https://doi.org/10.1021/nl902948m.

[33] J.M.B. Lopes dos Santos, N.M.R. Peres, A.H. Castro Neto, Graphene Bilayer with a Twist: Electronic Structure, Phys. Rev. Lett. 99 (2007) 256802. https://doi.org/10.1103/PhysRevLett.99.256802.

[34] G. Li, A. Luican, J.M.B. Lopes dos Santos, A.H. Castro Neto, A. Reina, J. Kong, E.Y. Andrei, Observation of Van Hove singularities in twisted graphene layers, Nat. Phys. 6 (2010) 109–113. https://doi.org/10.1038/nphys1463.

[35] W. Yan, M. Liu, R.-F. Dou, L. Meng, L. Feng, Z.-D. Chu, Y. Zhang, Z. Liu, J.-C. Nie, L. He, Angle-Dependent van Hove Singularities in a Slightly Twisted Graphene Bilayer, Phys. Rev. Lett. 109 (2012) 126801. https://doi.org/10.1103/PhysRevLett.109.126801.

[36] J. González, Kohn-Luttinger superconductivity in graphene, Phys. Rev. B 78 (2008) 205431. https://doi.org/10.1103/PhysRevB.78.205431.

[37] S. Shallcross, S. Sharma, E. Kandelaki, O.A. Pankratov, Electronic structure of turbostratic graphene, Phys. Rev. B 81 (2010) 165105. https://doi.org/10.1103/PhysRevB.81.165105.

[38] Z. Yu, A. Song, L. Sun, Y. Li, L. Gao, H. Peng, T. Ma, Z. Liu, J. Luo, Understanding Interlayer Contact Conductance in Twisted Bilayer Graphene, Small 16 (2020) 1902844. https://doi.org/10.1002/smll.201902844.

[39] T. Ando, Screening Effect and Impurity Scattering in Monolayer Graphene, J. Phys. Soc. Jpn. 75 (2006) 074716. https://doi.org/10.1143/JPSJ.75.074716.

[40] S. Adam, E.H. Hwang, V.M. Galitski, S. Das Sarma, A self-consistent theory for graphene transport, Proc. Natl. Acad. Sci. 104 (2007) 18392–18397. https://doi.org/10.1073/pnas.0704772104.

[41] S.A. Mojtahedzadeh, H. Tanaka, N. Mori, Monte Carlo simulation of mobility enhancement in multilayer graphene with turbostratic structure, Jpn. J. Appl. Phys. 63 (2024) 031004. https://doi.org/10.35848/1347-4065/ad2aa3.

[42] K. Uemura, T. Ikuta, K. Maehashi, Turbostratic stacked CVD graphene for high-performance devices, Jpn. J. Appl. Phys. 57 (2018) 030311. https://doi.org/10.7567/JJAP.57.030311.

[43] M. Shimatani, N. Yamada, S. Fukushima, S. Okuda, S. Ogawa, T. Ikuta, K. Maehashi, High-responsivity turbostratic stacked graphene photodetectors using enhanced photogating, Appl. Phys. Express 12 (2019) 122010. https://doi.org/10.7567/1882-0786/ab5096.

[44] M. Shimatani, T. Ikuta, Y. Sakamoto, S. Fukushima, S. Ogawa, K. Maehashi, Turbostratic stacked graphene-based high-responsivity mid-wavelength infrared detector using an

enhanced photogating effect, Opt. Mater. Express 12 (2022) 458–467. https://doi.org/10.1364/OME.449757.

[45] Review of CVD Synthesis of Graphene - Muñoz - 2013 - Chemical Vapor Deposition - Wiley Online Library, (n.d.). https://onlinelibrary.wiley.com/doi/10.1002/cvde.201300051 (accessed November 19, 2024).

[46] X. Li, W. Cai, J. An, S. Kim, J. Nah, D. Yang, R. Piner, A. Velamakanni, I. Jung, E. Tutuc, S.K. Banerjee, L. Colombo, R.S. Ruoff, Large-Area Synthesis of High-Quality and Uniform Graphene Films on Copper Foils, Science 324 (2009) 1312–1314. https://doi.org/10.1126/science.1171245.

[47] J. Zhang, L. Lin, K. Jia, L. Sun, H. Peng, Z. Liu, Controlled Growth of Single-Crystal Graphene Films, Adv. Mater. 32 (2020) 1903266. https://doi.org/10.1002/adma.201903266.

[48] P. Zhao, A. Kumamoto, S. Kim, X. Chen, B. Hou, S. Chiashi, E. Einarsson, Y. Ikuhara, S. Maruyama, Self-Limiting Chemical Vapor Deposition Growth of Monolayer Graphene from Ethanol, J. Phys. Chem. C 117 (2013) 10755–10763. https://doi.org/10.1021/jp400996s.

[49] H. Ago, Y. Ogawa, M. Tsuji, S. Mizuno, H. Hibino, Catalytic Growth of Graphene: Toward Large-Area Single-Crystalline Graphene, J. Phys. Chem. Lett. 3 (2012) 2228–2236. https://doi.org/10.1021/jz3007029.

[50] S.J. Chae, F. Güneş, K.K. Kim, E.S. Kim, G.H. Han, S.M. Kim, H.-J. Shin, S.-M. Yoon, J.-Y. Choi, M.H. Park, C.W. Yang, D. Pribat, Y.H. Lee, Synthesis of Large-Area Graphene Layers on Poly-Nickel Substrate by Chemical Vapor Deposition: Wrinkle Formation, Adv. Mater. 21 (2009) 2328–2333. https://doi.org/10.1002/adma.200803016.

[51] P. Solís-Fernández, Y. Terao, K. Kawahara, W. Nishiyama, T. Uwanno, Y.-C. Lin, K. Yamamoto, H. Nakashima, K. Nagashio, H. Hibino, K. Suenaga, H. Ago, Isothermal Growth and Stacking Evolution in Highly Uniform Bernal-Stacked Bilayer Graphene, ACS Nano 14 (2020) 6834–6844. https://doi.org/10.1021/acsnano.0c00645.

[52] C.-C. Lu, Y.-C. Lin, Z. Liu, C.-H. Yeh, K. Suenaga, P.-W. Chiu, Twisting Bilayer Graphene Superlattices, ACS Nano 7 (2013) 2587–2594. https://doi.org/10.1021/nn3059828.

[53] J. Yin, H. Wang, H. Peng, Z. Tan, L. Liao, L. Lin, X. Sun, A.L. Koh, Y. Chen, H. Peng, Z. Liu, Selectively enhanced photocurrent generation in twisted bilayer graphene with van Hove singularity, Nat. Commun. 7 (2016) 10699. https://doi.org/10.1038/ncomms10699.

[54] L. Sun, Z. Wang, Y. Wang, L. Zhao, Y. Li, B. Chen, S. Huang, S. Zhang, W. Wang, D. Pei, H. Fang, S. Zhong, H. Liu, J. Zhang, L. Tong, Y. Chen, Z. Li, M.H. Rümmeli, K.S. Novoselov, H. Peng, L. Lin, Z. Liu, Hetero-site nucleation for growing twisted bilayer graphene with a wide range of twist angles, Nat. Commun. 12 (2021) 2391. https://doi.org/10.1038/s41467-021-22533-1.

[55] Highly Uniform Bilayer Graphene on Epitaxial Cu–Ni(111) Alloy | Chemistry of Materials, (n.d.). https://pubs.acs.org/doi/10.1021/acs.chemmater.6b01137 (accessed November 19, 2024).

[56] K. Sharda, Growing twisted bilayer graphene at small angles, Chem 7 (2021) 2860–2862. https://doi.org/10.1016/j.chempr.2021.10.018.

[57] Z. Gao, Q. Zhang, C.H. Naylor, Y. Kim, I.H. Abidi, J. Ping, P. Ducos, J. Zauberman, M.-Q. Zhao, A.M. Rappe, Z. Luo, L. Ren, A.T.C. Johnson, Crystalline Bilayer Graphene with

Preferential Stacking from Ni–Cu Gradient Alloy, ACS Nano 12 (2018) 2275–2282. https://doi.org/10.1021/acsnano.7b06992.

[58] H. Kageshima, H. Hibino, M. Nagase, H. Yamaguchi, Theoretical Study of Epitaxial Graphene Growth on SiC(0001) Surfaces, Appl. Phys. Express 2 (2009) 065502. https://doi.org/10.1143/APEX.2.065502.

[59] G.G. Jernigan, B.L. VanMil, J.L. Tedesco, J.G. Tischler, E.R. Glaser, A.I. Davidson, P.M. Campbell, D.K. Gaskill, Comparison of Epitaxial Graphene on Si-face and C-face 4H SiC Formed by Ultrahigh Vacuum and RF Furnace Production, Nano Lett. 9 (2009) 2605–2609. https://doi.org/10.1021/nl900803z.

[60] K.V. Emtsev, A. Bostwick, K. Horn, J. Jobst, G.L. Kellogg, L. Ley, J.L. McChesney, T. Ohta, S.A. Reshanov, J. Röhrl, E. Rotenberg, A.K. Schmid, D. Waldmann, H.B. Weber, T. Seyller, Towards wafer-size graphene layers by atmospheric pressure graphitization of silicon carbide, Nat. Mater. 8 (2009) 203–207. https://doi.org/10.1038/nmat2382.

[61] C. Berger, Z. Song, T. Li, X. Li, A.Y. Ogbazghi, R. Feng, Z. Dai, A.N. Marchenkov, E.H. Conrad, P.N. First, W.A. de Heer, Ultrathin Epitaxial Graphite: 2D Electron Gas Properties and a Route toward Graphene-based Nanoelectronics, J. Phys. Chem. B 108 (2004) 19912–19916. https://doi.org/10.1021/jp040650f.

[62] I. Razado-Colambo, J. Avila, D. Vignaud, S. Godey, X. Wallart, D.P. Woodruff, M.C. Asensio, Structural determination of bilayer graphene on SiC(0001) using synchrotron radiation photoelectron diffraction, Sci. Rep. 8 (2018) 10190. https://doi.org/10.1038/s41598-018-28402-0.

[63] I. Razado-Colambo, J. Avila, D. Vignaud, S. Godey, X. Wallart, D.P. Woodruff, M.C. Asensio, Structural determination of bilayer graphene on SiC(0001) using synchrotron radiation photoelectron diffraction, Sci. Rep. 8 (2018) 10190. https://doi.org/10.1038/s41598-018-28402-0.

[64] K. Lee, S. Kim, M.S. Points, T.E. Beechem, T. Ohta, E. Tutuc, Magnetotransport Properties of Quasi-Free-Standing Epitaxial Graphene Bilayer on SiC: Evidence for Bernal Stacking, Nano Lett. 11 (2011) 3624–3628. https://doi.org/10.1021/nl201430a.

[65] W. Norimatsu, Selective formation of ABC-stacked graphene layers on SiC(0001), Phys. Rev. B 81 (2010). https://doi.org/10.1103/PhysRevB.81.161410.

[66] L.A. Galves, J.M. Wofford, G.V. Soares, U. Jahn, C. Pfüller, H. Riechert, J.M.J. Lopes, The effect of the SiC(0001) surface morphology on the growth of epitaxial mono-layer graphene nanoribbons, Carbon 115 (2017) 162–168. https://doi.org/10.1016/j.carbon.2017.01.018.

[67] I. Razado-Colambo, Probing the electronic properties of graphene on C-face SiC down to single domains by nanoresolved photoelectron spectroscopies, Phys. Rev. B 92 (2015). https://doi.org/10.1103/PhysRevB.92.035105.

[68] Phys. Rev. Lett. 107, 216602 (2011) - Quantum Hall Effect in Twisted Bilayer Graphene, (n.d.). https://journals.aps.org/prl/abstract/10.1103/PhysRevLett.107.216602 (accessed November 19, 2024).

[69] Z. Ni, Reduction of Fermi velocity in folded graphene observed by resonance Raman spectroscopy, Phys. Rev. B 77 (2008). https://doi.org/10.1103/PhysRevB.77.235403.

[70] J. Zhang, Free Folding of Suspended Graphene Sheets by Random Mechanical Stimulation,

Phys. Rev. Lett. 104 (2010). https://doi.org/10.1103/PhysRevLett.104.166805.
[71] V. Carozo, Resonance effects on the Raman spectra of graphene superlattices, Phys. Rev. B 88 (2013). https://doi.org/10.1103/PhysRevB.88.085401.
[72] X. Chen, C. Yi, C. Ke, Bending stiffness and interlayer shear modulus of few-layer graphene, Appl. Phys. Lett. 106 (2015) 101907. https://doi.org/10.1063/1.4915075.
[73] B. Wang, M. Huang, N.Y. Kim, B.V. Cunning, Y. Huang, D. Qu, X. Chen, S. Jin, M. Biswal, X. Zhang, S.H. Lee, H. Lim, W.J. Yoo, Z. Lee, R.S. Ruoff, Controlled Folding of Single Crystal Graphene, Nano Lett. 17 (2017) 1467–1473. https://doi.org/10.1021/acs.nanolett.6b04459.
[74] M. Yi, Z. Shen, A review on mechanical exfoliation for the scalable production of graphene, J. Mater. Chem. A 3 (2015) 11700–11715. https://doi.org/10.1039/C5TA00252D.
[75] S. Neubeck, Y.M. You, Z.H. Ni, P. Blake, Z.X. Shen, A.K. Geim, K.S. Novoselov, Direct determination of the crystallographic orientation of graphene edges by atomic resolution imaging, Appl. Phys. Lett. 97 (2010) 053110. https://doi.org/10.1063/1.3467468.
[76] X.-D. Chen, W. Xin, W.-S. Jiang, Z.-B. Liu, Yongsheng Chen, J.-G. Tian, High-Precision Twist-Controlled Bilayer and Trilayer Graphene, Adv. Mater. 28 (2016) 2563–2570. https://doi.org/10.1002/adma.201505129.
[77] K. Kim, M. Yankowitz, B. Fallahazad, S. Kang, H.C.P. Movva, S. Huang, S. Larentis, C.M. Corbet, T. Taniguchi, K. Watanabe, S.K. Banerjee, B.J. LeRoy, E. Tutuc, van der Waals Heterostructures with High Accuracy Rotational Alignment, Nano Lett. 16 (2016) 1989–1995. https://doi.org/10.1021/acs.nanolett.5b05263.
[78] K. Kim, A. DaSilva, S. Huang, B. Fallahazad, S. Larentis, T. Taniguchi, K. Watanabe, B.J. LeRoy, A.H. MacDonald, E. Tutuc, Tunable moiré bands and strong correlations in small-twist-angle bilayer graphene, Proc. Natl. Acad. Sci. 114 (2017) 3364–3369. https://doi.org/10.1073/pnas.1620140114.
[79] C.-J. Kim, A. Sánchez-Castillo, Z. Ziegler, Y. Ogawa, C. Noguez, J. Park, Chiral atomically thin films, Nat. Nanotechnol. 11 (2016) 520–524. https://doi.org/10.1038/nnano.2016.3.
[80] J.T. Robinson, S.W. Schmucker, C.B. Diaconescu, J.P. Long, J.C. Culbertson, T. Ohta, A.L. Friedman, T.E. Beechem, Electronic Hybridization of Large-Area Stacked Graphene Films, ACS Nano 7 (2013) 637–644. https://doi.org/10.1021/nn304834p.
[81] K. Kim, Raman Spectroscopy Study of Rotated Double-Layer Graphene: Misorientation-Angle Dependence of Electronic Structure, Phys. Rev. Lett. 108 (2012). https://doi.org/10.1103/PhysRevLett.108.246103.
[82] Z. Tan, J. Yin, C. Chen, H. Wang, L. Lin, L. Sun, J. Wu, X. Sun, H. Yang, Y. Chen, H. Peng, Z. Liu, Building Large-Domain Twisted Bilayer Graphene with van Hove Singularity, ACS Nano 10 (2016) 6725–6730. https://doi.org/10.1021/acsnano.6b02046.
[83] B. Zhuang, S. Li, S. Li, J. Yin, Ways to eliminate PMMA residues on graphene —— superclean graphene, Carbon 173 (2021) 609–636. https://doi.org/10.1016/j.carbon.2020.11.047.
[84] Y.-C. Lin, C.-C. Lu, C.-H. Yeh, C. Jin, K. Suenaga, P.-W. Chiu, Graphene Annealing: How Clean Can It Be?, Nano Lett. 12 (2012) 414–419. https://doi.org/10.1021/nl203733r.
[85] Rapid Selective Etching of PMMA Residues from Transferred Graphene by Carbon Dioxide |

The Journal of Physical Chemistry C, (n.d.). https://pubs.acs.org/doi/full/10.1021/jp408429v (accessed November 20, 2024).

[86] M. Her, R. Beams, L. Novotny, Graphene transfer with reduced residue, Phys. Lett. A 377 (2013) 1455–1458. https://doi.org/10.1016/j.physleta.2013.04.015.

[87] H. Sun, D. Chen, Y. Wu, Q. Yuan, L. Guo, D. Dai, Y. Xu, P. Zhao, N. Jiang, C.-T. Lin, High quality graphene films with a clean surface prepared by an UV/ozone assisted transfer process, J. Mater. Chem. C 5 (2017) 1880–1884. https://doi.org/10.1039/C6TC05505B.

[88] W.J. Choi, Y.J. Chung, S. Park, C.-S. Yang, Y.K. Lee, K.-S. An, Y.-S. Lee, J.-O. Lee, A Simple Method for Cleaning Graphene Surfaces with an Electrostatic Force, Adv. Mater. 26 (2014) 637–644. https://doi.org/10.1002/adma.201303199.

[89] L. Sun, L. Lin, Z. Wang, D. Rui, Z. Yu, J. Zhang, Y. Li, X. Liu, K. Jia, K. Wang, L. Zheng, B. Deng, T. Ma, N. Kang, H. Xu, K.S. Novoselov, H. Peng, Z. Liu, A Force-Engineered Lint Roller for Superclean Graphene, Adv. Mater. 31 (2019) 1902978. https://doi.org/10.1002/adma.201902978.

[90] Y.-C. Chen, W.-H. Lin, W.-S. Tseng, C.-C. Chen, George.R. Rossman, C.-D. Chen, Y.-S. Wu, N.-C. Yeh, Direct growth of mm-size twisted bilayer graphene by plasma-enhanced chemical vapor deposition, Carbon 156 (2020) 212–224. https://doi.org/10.1016/j.carbon.2019.09.052.

[91] I. Razado-Colambo, J. Avila, J.-P. Nys, C. Chen, X. Wallart, M.-C. Asensio, D. Vignaud, NanoARPES of twisted bilayer graphene on SiC: absence of velocity renormalization for small angles, Sci. Rep. 6 (2016) 27261. https://doi.org/10.1038/srep27261.

[92] S. Pezzini, V. Mišeikis, G. Piccinini, S. Forti, S. Pace, R. Engelke, F. Rossella, K. Watanabe, T. Taniguchi, P. Kim, C. Coletti, 30°-Twisted Bilayer Graphene Quasicrystals from Chemical Vapor Deposition, Nano Lett. 20 (2020) 3313–3319. https://doi.org/10.1021/acs.nanolett.0c00172.

[93] T. Latychevskaia, C. Escher, H.-W. Fink, Moiré structures in twisted bilayer graphene studied by transmission electron microscopy, Ultramicroscopy 197 (2019) 46–52. https://doi.org/10.1016/j.ultramic.2018.11.009.

[94] H. Imamura, A. Visikovskiy, R. Uotani, T. Kajiwara, H. Ando, T. Iimori, K. Iwata, T. Miyamachi, K. Nakatsuji, K. Mase, T. Shirasawa, F. Komori, S. Tanaka, Twisted bilayer graphene fabricated by direct bonding in a high vacuum, Appl. Phys. Express 13 (2020) 075004. https://doi.org/10.35848/1882-0786/ab99d1.

[95] J. Campos-Delgado, G. Algara-Siller, C.N. Santos, U. Kaiser, J.-P. Raskin, Twisted Bi-Layer Graphene: Microscopic Rainbows, Small 9 (2013) 3247–3251. https://doi.org/10.1002/smll.201300050.

[96] K. Kim, Raman Spectroscopy Study of Rotated Double-Layer Graphene: Misorientation-Angle Dependence of Electronic Structure, Phys. Rev. Lett. 108 (2012). https://doi.org/10.1103/PhysRevLett.108.246103.

[97] P. Poncharal, Raman spectra of misoriented bilayer graphene, Phys. Rev. B 78 (2008). https://doi.org/10.1103/PhysRevB.78.113407.

[98] A.C. Ferrari, Raman Spectrum of Graphene and Graphene Layers, Phys. Rev. Lett. 97 (2006). https://doi.org/10.1103/PhysRevLett.97.187401.

[99] V. Carozo, Resonance effects on the Raman spectra of graphene superlattices, Phys. Rev. B

88 (2013). https://doi.org/10.1103/PhysRevB.88.085401.
[100] V. Carozo, C.M. Almeida, E.H.M. Ferreira, L.G. Cançado, C.A. Achete, A. Jorio, Raman Signature of Graphene Superlattices, Nano Lett. 11 (2011) 4527–4534. https://doi.org/10.1021/nl201370m.
[101] Y. Chen, L. Meng, W. Zhao, Z. Liang, X. Wu, H. Nan, Z. Wu, S. Huang, L. Sun, J. Wang, Z. Ni, Raman mapping investigation of chemical vapor deposition-fabricated twisted bilayer graphene with irregular grains, Phys. Chem. Chem. Phys. 16 (2014) 21682–21687. https://doi.org/10.1039/C4CP03386H.
[102] Yukio Saito, Statistical Mechanics of Surface, in: Stat. Phys. Cryst. Growth, WORLD SCIENTIFIC, 1996: pp. 20–45.
[103] M.R. Habib, T. Liang, X. Yu, X. Pi, Y. Liu, M. Xu, A review of theoretical study of graphene chemical vapor deposition synthesis on metals: nucleation, growth, and the role of hydrogen and oxygen, Rep. Prog. Phys. 81 (2018) 036501. https://doi.org/10.1088/1361-6633/aa9bbf.
[104] Q. Yuan, J. Gao, H. Shu, J. Zhao, X. Chen, F. Ding, Magic Carbon Clusters in the Chemical Vapor Deposition Growth of Graphene, J. Am. Chem. Soc. 134 (2012) 2970–2975. https://doi.org/10.1021/ja2050875.
[105] L.A. Girifalco, M. Hodak, Van der Waals binding energies in graphitic structures, Phys. Rev. B 65 (2002) 125404. https://doi.org/10.1103/PhysRevB.65.125404.
[106] 上羽 牧夫, ゆらぎと結晶核の生成, in: 結晶成長のしくみを探る その物理的基礎, 共立出版, 2002: pp. 26–43.
[107] 中田一郎, 結晶成長の一般理論, 日本結晶学会誌 9 (1967).
[108] C.-M. Seah, S.-P. Chai, A.R. Mohamed, Mechanisms of graphene growth by chemical vapour deposition on transition metals, Carbon 70 (2014) 1–21. https://doi.org/10.1016/j.carbon.2013.12.073.
[109] W. Liu, H. Li, C. Xu, Y. Khatami, K. Banerjee, Synthesis of high-quality monolayer and bilayer graphene on copper using chemical vapor deposition, Carbon 49 (2011) 4122–4130. https://doi.org/10.1016/j.carbon.2011.05.047.
[110] L. Wang, X. Zhang, H.L.W. Chan, F. Yan, F. Ding, Formation and Healing of Vacancies in Graphene Chemical Vapor Deposition (CVD) Growth, J. Am. Chem. Soc. 135 (2013) 4476–4482. https://doi.org/10.1021/ja312687a.
[111] H.-B. Li, A.J. Page, C. Hettich, B. Aradi, C. Köhler, T. Frauenheim, S. Irle, K. Morokuma, Graphene nucleation on a surface-molten copper catalyst: quantum chemical molecular dynamics simulations, Chem. Sci. 5 (2014) 3493–3500. https://doi.org/10.1039/C4SC00491D.
[112] X. Wang, Q. Yuan, J. Li, F. Ding, The transition metal surface dependent methane decomposition in graphene chemical vapor deposition growth, Nanoscale 9 (2017) 11584–11589. https://doi.org/10.1039/C7NR02743E.
[113] H. Kim, E. Saiz, M. Chhowalla, C. Mattevi, Modeling of the self-limited growth in catalytic chemical vapor deposition of graphene, New J. Phys. 15 (2013) 053012. https://doi.org/10.1088/1367-2630/15/5/053012.
[114] X. Li, W. Cai, L. Colombo, R.S. Ruoff, Evolution of Graphene Growth on Ni and Cu by Carbon Isotope Labeling, Nano Lett. 9 (2009) 4268–4272.

https://doi.org/10.1021/nl902515k.
[115] M.H. Ani, M.A. Kamarudin, A.H. Ramlan, E. Ismail, M.S. Sirat, M.A. Mohamed, M.A. Azam, A critical review on the contributions of chemical and physical factors toward the nucleation and growth of large-area graphene, J. Mater. Sci. 53 (2018) 7095–7111. https://doi.org/10.1007/s10853-018-1994-0.
[116] A.W. Robertson, J.H. Warner, Hexagonal Single Crystal Domains of Few-Layer Graphene on Copper Foils, Nano Lett. 11 (2011) 1182–1189. https://doi.org/10.1021/nl104142k.
[117] Z. Ullah, S. Riaz, Q. Li, S. Atiq, M. Saleem, M. Azhar, S. Naseem, L. Liu, A comparative study of graphene growth by APCVD, LPCVD and PECVD, Mater. Res. Express 5 (2018) 035606. https://doi.org/10.1088/2053-1591/aab7b4.
[118] P. Zhao, S. Kim, X. Chen, E. Einarsson, M. Wang, Y. Song, H. Wang, S. Chiashi, R. Xiang, S. Maruyama, Equilibrium Chemical Vapor Deposition Growth of Bernal-Stacked Bilayer Graphene, ACS Nano 8 (2014) 11631–11638. https://doi.org/10.1021/nn5049188.
[119] Y. Song, J. Zhuang, M. Song, S. Yin, Y. Cheng, X. Zhang, M. Wang, R. Xiang, Y. Xia, S. Maruyama, P. Zhao, F. Ding, H. Wang, Epitaxial nucleation of CVD bilayer graphene on copper, Nanoscale 8 (2016) 20001–20007. https://doi.org/10.1039/C6NR04557J.
[120] Q. Li, H. Chou, J.-H. Zhong, J.-Y. Liu, A. Dolocan, J. Zhang, Y. Zhou, R.S. Ruoff, S. Chen, W. Cai, Growth of Adlayer Graphene on Cu Studied by Carbon Isotope Labeling, Nano Lett. 13 (2013) 486–490. https://doi.org/10.1021/nl303879k.
[121] J. Chen, Y. Wen, Y. Guo, B. Wu, L. Huang, Y. Xue, D. Geng, D. Wang, G. Yu, Y. Liu, Oxygen-Aided Synthesis of Polycrystalline Graphene on Silicon Dioxide Substrates, J. Am. Chem. Soc. 133 (2011) 17548–17551. https://doi.org/10.1021/ja2063633.
[122] X. Chen, B. Wu, Y. Liu, Direct preparation of high quality graphene on dielectric substrates, Chem. Soc. Rev. 45 (2016) 2057–2074. https://doi.org/10.1039/C5CS00542F.
[123] J. Sun, M.T. Cole, N. Lindvall, K.B.K. Teo, A. Yurgens, Noncatalytic chemical vapor deposition of graphene on high-temperature substrates for transparent electrodes, Appl. Phys. Lett. 100 (2012) 022102. https://doi.org/10.1063/1.3675632.
[124] Z. Liu, Interlayer binding energy of graphite: A mesoscopic determination from deformation, Phys. Rev. B 85 (2012). https://doi.org/10.1103/PhysRevB.85.205418.
[125] J. Abrahamson, The surface energies of graphite, Carbon 11 (1973) 337–362. https://doi.org/10.1016/0008-6223(73)90075-4.
[126] A. Ōya, H. Marsh, Phenomena of catalytic graphitization, J. Mater. Sci. 17 (1982) 309–322. https://doi.org/10.1007/BF00591464.
[127] X.-D. Chen, Z. Chen, W.-S. Jiang, C. Zhang, J. Sun, H. Wang, W. Xin, L. Lin, M.K. Priydarshi, H. Yang, Z.-B. Liu, J.-G. Tian, Y. Zhang, Y. Zhang, Z. Liu, Fast Growth and Broad Applications of 25-Inch Uniform Graphene Glass, Adv. Mater. 29 (2017) 1603428. https://doi.org/10.1002/adma.201603428.
[128] A.V. Minakov, M.M. Simunin, I.I. Ryzhkov, Modelling of ethanol pyrolysis in a commercial CVD reactor for growing carbon layers on alumina substrates, Int. J. Heat Mass Transf. 145 (2019) 118764. https://doi.org/10.1016/j.ijheatmasstransfer.2019.118764.
[129] C. Yu, H. Liu, X. Sun, J. Shi, Z. Jing, X. Sun, Y. Song, W. Yin, G. Zhang, L. Sun, Z. Liu, Theoretical investigations on hydroxyl carbon precursor fueled growth of graphene on

transition metal substrates, Nano Res. 17 (2024) 10235–10241. https://doi.org/10.1007/s12274-024-6882-0.

[130] W. Zhang, P. Wu, Z. Li, J. Yang, First-Principles Thermodynamics of Graphene Growth on Cu Surfaces, J. Phys. Chem. C 115 (2011) 17782–17787. https://doi.org/10.1021/jp2006827.

[131] S.K. Tiwari, S.K. Pandey, R. Pandey, N. Wang, M. Bystrzejewski, Y.K. Mishra, Y. Zhu, Stone–Wales Defect in Graphene, Small 19 (2023) 2303340. https://doi.org/10.1002/smll.202303340.

[132] P.L. de Andres, J.A. Vergés, First-principles calculation of the effect of stress on the chemical activity of graphene, Appl. Phys. Lett. 93 (2008) 171915. https://doi.org/10.1063/1.3010740.

[133] A. Vela, Electronic structure and optical properties of twisted multilayer graphene, Phys. Rev. B 98 (2018). https://doi.org/10.1103/PhysRevB.98.155135.

[134] S. Shallcross, Electronic structure of turbostratic graphene, Phys. Rev. B 81 (2010). https://doi.org/10.1103/PhysRevB.81.165105.

[135] U. Mogera, S. Walia, B. Bannur, M. Gedda, G.U. Kulkarni, Intrinsic Nature of Graphene Revealed in Temperature-Dependent Transport of Twisted Multilayer Graphene, J. Phys. Chem. C 121 (2017) 13938–13943. https://doi.org/10.1021/acs.jpcc.7b04068.

[136] K. Nagashio, T. Nishimura, K. Kita, A. Toriumi, Systematic Investigation of the Intrinsic Channel Properties and Contact Resistance of Monolayer and Multilayer Graphene Field-Effect Transistor, Jpn. J. Appl. Phys. 49 (2010) 051304. https://doi.org/10.1143/JJAP.49.051304.

[137] T. Ohta, Interlayer Interaction and Electronic Screening in Multilayer Graphene Investigated with Angle-Resolved Photoemission Spectroscopy, Phys. Rev. Lett. 98 (2007). https://doi.org/10.1103/PhysRevLett.98.206802.

[138] Y. Sui, J. Appenzeller, Screening and Interlayer Coupling in Multilayer Graphene Field-Effect Transistors, Nano Lett. 9 (2009) 2973–2977. https://doi.org/10.1021/nl901396g.

[139] R. Negishi, C. Wei, Y. Yao, Y. Ogawa, M. Akabori, Y. Kanai, K. Matsumoto, Y. Taniyasu, Y. Kobayashi, Turbostratic Stacking Effect in Multilayer Graphene on the Electrical Transport Properties, Phys. Status Solidi B 257 (2020) 1900437. https://doi.org/10.1002/pssb.201900437.

[140] C. Wei, R. Negishi, Y. Ogawa, M. Akabori, Y. Taniyasu, Y. Kobayashi, Turbostratic multilayer graphene synthesis on CVD graphene template toward improving electrical performance, Jpn. J. Appl. Phys. 58 (2019) SIIB04. https://doi.org/10.7567/1347-4065/ab0c7b.

[141] A. Khan, S.M. Islam, S. Ahmed, R.R. Kumar, M.R. Habib, K. Huang, M. Hu, X. Yu, D. Yang, Direct CVD Growth of Graphene on Technologically Important Dielectric and Semiconducting Substrates, Adv. Sci. 5 (2018) 1800050. https://doi.org/10.1002/advs.201800050.

[142] K. Akhtar, S.A. Khan, S.B. Khan, A.M. Asiri, Scanning Electron Microscopy: Principle and Applications in Nanomaterials Characterization, in: S.K. Sharma (Ed.), Handb. Mater. Charact., Springer International Publishing, Cham, 2018: pp. 113–145. https://doi.org/10.1007/978-3-319-92955-2_4.

[143] Homma Y., Kato H., SEM Observation of Carbon Nanotube and Graphene, Hyomen Kagaku

36 (2015) 178–183. https://doi.org/10.1380/jsssj.36.178.

[144] C.C. Moura, R.S. Tare, R.O.C. Oreffo, S. Mahajan, Raman spectroscopy and coherent anti-Stokes Raman scattering imaging: prospective tools for monitoring skeletal cells and skeletal regeneration, J. R. Soc. Interface 13 (2016) 20160182. https://doi.org/10.1098/rsif.2016.0182.

[145] A. Downes, A. Elfick, Raman Spectroscopy and Related Techniques in Biomedicine, Sensors 10 (2010) 1871–1889. https://doi.org/10.3390/s100301871.

[146] F. Fromm, M.H.O. Jr, A. Molina-Sánchez, M. Hundhausen, J.M.J. Lopes, H. Riechert, L. Wirtz, T. Seyller, Contribution of the buffer layer to the Raman spectrum of epitaxial graphene on SiC(0001), New J. Phys. 15 (2013) 043031. https://doi.org/10.1088/1367-2630/15/4/043031.

[147] Y. Cao, V. Fatemi, A. Demir, S. Fang, S.L. Tomarken, J.Y. Luo, J.D. Sanchez-Yamagishi, K. Watanabe, T. Taniguchi, E. Kaxiras, R.C. Ashoori, P. Jarillo-Herrero, Correlated insulator behaviour at half-filling in magic-angle graphene superlattices, Nature 556 (2018) 80–84. https://doi.org/10.1038/nature26154.

[148] M. Zarenia, Enhanced hydrodynamic transport in near magic angle twisted bilayer graphene, Phys. Rev. B 101 (2020). https://doi.org/10.1103/PhysRevB.101.045421.

[149] I. Forbeaux, J.-M. Themlin, J.-M. Debever, Heteroepitaxial graphite on 6 H − SiC (0001) : Interface formation through conduction-band electronic structure, Phys. Rev. B 58 (1998) 16396–16406. https://doi.org/10.1103/PhysRevB.58.16396.

[150] K.K. Kim, A. Hsu, X. Jia, S.M. Kim, Y. Shi, M. Hofmann, D. Nezich, J.F. Rodriguez-Nieva, M. Dresselhaus, T. Palacios, J. Kong, Synthesis of Monolayer Hexagonal Boron Nitride on Cu Foil Using Chemical Vapor Deposition, Nano Lett. 12 (2012) 161–166. https://doi.org/10.1021/nl203249a.

[151] L. Zhang, Z. Shi, D. Liu, R. Yang, D. Shi, G. Zhang, Vapour-phase graphene epitaxy at low temperatures, Nano Res. 5 (2012) 258–264. https://doi.org/10.1007/s12274-012-0205-6.

[152] R. Negishi, H. Hirano, Y. Ohno, K. Haehashi, K. Matsumoto, Y. Kobayashi, Thickness Control of Graphene Overlayer via Layer-by-Layer Growth on Graphene Templates by Chemical Vapor Deposition, Jpn. J. Appl. Phys. 50 (2011) 06GE04. https://doi.org/10.1143/JJAP.50.06GE04.

[153] A.W. Cummings, D.L. Duong, V.L. Nguyen, D. Van Tuan, J. Kotakoski, J.E. Barrios Vargas, Y.H. Lee, S. Roche, Charge Transport in Polycrystalline Graphene: Challenges and Opportunities, Adv. Mater. 26 (2014) 5079–5094. https://doi.org/10.1002/adma.201401389.

[154] S. Tanabe, Carrier transport mechanism in graphene on SiC(0001), Phys. Rev. B 84 (2011). https://doi.org/10.1103/PhysRevB.84.115458.

[155] S. Tanabe, M. Takamura, Y. Harada, H. Kageshima, H. Hibino, Quantum Hall Effect and Carrier Scattering in Quasi-Free-Standing Monolayer Graphene, Appl. Phys. Express 5 (2012) 125101. https://doi.org/10.1143/APEX.5.125101.

[156] B.K. Daas, S.U. Omar, S. Shetu, K.M. Daniels, S. Ma, T.S. Sudarshan, M.V.S. Chandrashekhar, Comparison of Epitaxial Graphene Growth on Polar and Nonpolar 6H-SiC Faces: On the Growth of Multilayer Films, Cryst. Growth Des. 12 (2012) 3379–3387. https://doi.org/10.1021/cg300456v.

[157] C. Virojanadara, R. Yakimova, J.R. Osiecki, M. Syväjärvi, R.I.G. Uhrberg, L.I. Johansson, A.A. Zakharov, Substrate orientation: A way towards higher quality monolayer graphene growth on 6H-SiC(0001), Surf. Sci. 603 (2009) L87–L90. https://doi.org/10.1016/j.susc.2009.05.005.

[158] L. Sun, Z. Wang, Y. Wang, L. Zhao, Y. Li, B. Chen, S. Huang, S. Zhang, W. Wang, D. Pei, H. Fang, S. Zhong, H. Liu, J. Zhang, L. Tong, Y. Chen, Z. Li, M.H. Rümmeli, K.S. Novoselov, H. Peng, L. Lin, Z. Liu, Hetero-site nucleation for growing twisted bilayer graphene with a wide range of twist angles, Nat. Commun. 12 (2021) 2391. https://doi.org/10.1038/s41467-021-22533-1.

[159] L. Sun, Z. Wang, Y. Wang, L. Zhao, Y. Li, B. Chen, S. Huang, S. Zhang, W. Wang, D. Pei, H. Fang, S. Zhong, H. Liu, J. Zhang, L. Tong, Y. Chen, Z. Li, M.H. Rümmeli, K.S. Novoselov, H. Peng, L. Lin, Z. Liu, Hetero-site nucleation for growing twisted bilayer graphene with a wide range of twist angles, Nat. Commun. 12 (2021) 2391. https://doi.org/10.1038/s41467-021-22533-1.

[160] S. Bagchi, H.T. Johnson, H.B. Chew, Rotational stability of twisted bilayer graphene, Phys. Rev. B 101 (2020) 054109. https://doi.org/10.1103/PhysRevB.101.054109.

[161] F. Peymanirad, S.K. Singh, H. Ghorbanfekr-Kalashami, K.S. Novoselov, F.M. Peeters, M. Neek-Amal, Thermal activated rotation of graphene flake on graphene, 2D Mater. 4 (2017) 025015. https://doi.org/10.1088/2053-1583/aa58a4.

[162] I.V. Lebedeva, A.A. Knizhnik, A.M. Popov, Y.E. Lozovik, B.V. Potapkin, Interlayer interaction and relative vibrations of bilayer graphene, Phys. Chem. Chem. Phys. 13 (2011) 5687–5695. https://doi.org/10.1039/C0CP02614J.

[163] David S. Gaskell and David E. Laughlin, Phase equilibrium in a one-component system, in: Introd. Thermodyn. Mater., Sixth edition, 2018: pp. 199–228.

[164] 上羽 牧夫, 結晶成長のための統計熱力学, in: 結晶成長のしくみを探る その物理的基礎, 共立出版, 2002: pp. 5–25.

[165] Marvin W. Chase Jr., NIST-JANAF Thermochemical Tables, in: American Institute of Physics, 1998: p. 551.

[166] H. Kim, C. Mattevi, M.R. Calvo, J.C. Oberg, L. Artiglia, S. Agnoli, C.F. Hirjibehedin, M. Chhowalla, E. Saiz, Activation Energy Paths for Graphene Nucleation and Growth on Cu, ACS Nano 6 (2012) 3614–3623. https://doi.org/10.1021/nn3008965.

[167] K.S. Kim, A.L. Walter, L. Moreschini, T. Seyller, K. Horn, E. Rotenberg, A. Bostwick, Coexisting massive and massless Dirac fermions in symmetry-broken bilayer graphene, Nat. Mater. 12 (2013) 887–892. https://doi.org/10.1038/nmat3717.

[168] N. Gupta, U. Mogera, G.U. Kulkarni, Ultrafast planar microsupercapacitor based on defect-free twisted multilayer graphene, Mater. Res. Bull. 152 (2022) 111841. https://doi.org/10.1016/j.materresbull.2022.111841.

[169] I.H. Baek, J.M. Hamm, K.J. Ahn, B.J. Kang, S.S. Oh, S. Bae, S.Y. Choi, B.H. Hong, D.-I. Yeom, B. Min, O. Hess, Y.U. Jeong, F. Rotermund, Boosting the terahertz nonlinearity of graphene by orientation disorder, 2D Mater. 4 (2017) 025035. https://doi.org/10.1088/2053-1583/aa5c64.

[170] R. Negishi, H. Hirano, Y. Ohno, K. Maehashi, K. Matsumoto, Y. Kobayashi, Layer-by-layer

growth of graphene layers on graphene substrates by chemical vapor deposition, Thin Solid Films 519 (2011) 6447–6452. https://doi.org/10.1016/j.tsf.2011.04.229.

[171] R. Negishi, Y. Ohno, K. Maehashi, K. Matsumoto, Y. Kobayashi, Carrier Transport Properties of the Field Effect Transistors with Graphene Channel Prepared by Chemical Vapor Deposition, Jpn. J. Appl. Phys. 51 (2012) 06FD03. https://doi.org/10.1143/JJAP.51.06FD03.

[172] Y. Yao, R. Negishi, D. Takajo, M. Takamura, Y. Taniyasu, Y. Kobayashi, Scanning probe analysis of twisted graphene grown on a graphene/silicon carbide template, Nanotechnology 33 (2022) 155603. https://doi.org/10.1088/1361-6528/ac473a.

[173] S.A. Kukushkin, A.V. Osipov, Nucleation and Growth Kinetics of Nanofilms, in: Nucleation Theory Appl., John Wiley & Sons, Ltd, 2005: pp. 215–255. https://doi.org/10.1002/3527604790.ch7.

[174] M. Uwaha, 8 - Growth Kinetics: Basics of Crystal Growth Mechanisms, in: T. Nishinaga (Ed.), Handb. Cryst. Growth Second Ed., Elsevier, Boston, 2015: pp. 359–399. https://doi.org/10.1016/B978-0-444-56369-9.00008-3.

[175] X. Tong, J.M. Gibson, Observation of dislocation-mediated layer-by-layer interface growth, Appl. Phys. Lett. 65 (1994) 168–170. https://doi.org/10.1063/1.112661.

[176] S. Stoyanov, I. Markov, On the 2D-3D transition in epitaxial thin film growth, Surf. Sci. 116 (1982) 313–337. https://doi.org/10.1016/0039-6028(82)90436-8.

[177] L. Houben, M. Luysberg, P. Hapke, O. Vetterl, F. Finger, R. Carius, H. Wagner, Morphological and crystallographic defect properties of microcrystalline silicon: a comparison between different growth modes, J. Non-Cryst. Solids 227–230 (1998) 896–900. https://doi.org/10.1016/S0022-3093(98)00239-7.

[178] G.R. Yazdi, F. Akhtar, I.G. Ivanov, S. Schmidt, I. Shtepliuk, A. Zakharov, T. Iakimov, R. Yakimova, Effect of epitaxial graphene morphology on adsorption of ambient species, Appl. Surf. Sci. 486 (2019) 239–248. https://doi.org/10.1016/j.apsusc.2019.04.247.

[179] S. Shivaraman, M.V.S. Chandrashekhar, J.J. Boeckl, M.G. Spencer, Thickness Estimation of Epitaxial Graphene on SiC Using Attenuation of Substrate Raman Intensity, J. Electron. Mater. 38 (2009) 725–730. https://doi.org/10.1007/s11664-009-0803-6.

[180] C. Riedl, C. Coletti, U. Starke, Structural and electronic properties of epitaxial graphene on SiC(0001): a review of growth, characterization, transfer doping and hydrogen intercalation, J. Phys. Appl. Phys. 43 (2010) 374009. https://doi.org/10.1088/0022-3727/43/37/374009.

[181] D. Robertson, G.M. Pound, Heterogeneous nucleation and film growth, C R C Crit. Rev. Solid State Sci. 4 (1973) 163–204. https://doi.org/10.1080/10408437308245824.

[182] R. Beckmann, B. Sobisch, W. Kulisch, C. Rau, Investigation of the bias nucleation process in microwave plasma-enhanced chemical vapour deposition of diamond, Diam. Relat. Mater. 3 (1994) 555–559. https://doi.org/10.1016/0925-9635(94)90223-2.

[183] J.A. Venables, G.D.T. Spiller, M. Hanbucken, Nucleation and growth of thin films, Rep. Prog. Phys. 47 (1984) 399. https://doi.org/10.1088/0034-4885/47/4/002.

[184] M. Gruschwitz, Epitaxial graphene on 6H-SiC(0001): Defects in SiC investigated by STEM, Phys. Rev. Mater. 3 (2019). https://doi.org/10.1103/PhysRevMaterials.3.094004.

[185] J.B. Hannon, R.M. Tromp, Pit formation during graphene synthesis on SiC(0001): In situ electron microscopy, Phys. Rev. B 77 (2008) 241404.

https://doi.org/10.1103/PhysRevB.77.241404.
[186] J. Röhrl, M. Hundhausen, K.V. Emtsev, Th. Seyller, R. Graupner, L. Ley, Raman spectra of epitaxial graphene on SiC(0001), Appl. Phys. Lett. 92 (2008) 201918. https://doi.org/10.1063/1.2929746.
[187] L.G. Cançado, K. Takai, T. Enoki, M. Endo, Y.A. Kim, H. Mizusaki, N.L. Speziali, A. Jorio, M.A. Pimenta, Measuring the degree of stacking order in graphite by Raman spectroscopy, Carbon 46 (2008) 272–275. https://doi.org/10.1016/j.carbon.2007.11.015.
[188] H. Kato, N. Itagaki, H.J. Im, Growth and Raman spectroscopy of thickness-controlled rotationally faulted multilayer graphene, Carbon 141 (2019) 76–82. https://doi.org/10.1016/j.carbon.2018.09.017.
[189] J.M. Velasco, S.A. Giamini, N. Kelaidis, P. Tsipas, D. Tsoutsou, G. Kordas, Y.S. Raptis, N. Boukos, A. Dimoulas, Reducing the layer number of AB stacked multilayer graphene grown on nickel by annealing at low temperature, Nanotechnology 26 (2015) 405603. https://doi.org/10.1088/0957-4484/26/40/405603.
[190] W. Strupinski, K. Grodecki, A. Wysmolek, R. Stepniewski, T. Szkopek, P.E. Gaskell, A. Grüneis, D. Haberer, R. Bozek, J. Krupka, J.M. Baranowski, Graphene Epitaxy by Chemical Vapor Deposition on SiC, Nano Lett. 11 (2011) 1786–1791. https://doi.org/10.1021/nl200390e.
[191] M. Koshino, Interlayer interaction in general incommensurate atomic layers, New J. Phys. 17 (2015) 015014. https://doi.org/10.1088/1367-2630/17/1/015014.
[192] M.O. Jahma, M. Rusanen, A. Karim, I.T. Koponen, T. Ala-Nissila, T.S. Rahman, Diffusion and submonolayer island growth during hyperthermal deposition on Cu(1 0 0) and Cu(1 1 1), Surf. Sci. 598 (2005) 246–252. https://doi.org/10.1016/j.susc.2005.09.030.
[193] Y. Kangawa, T. Ito, A. Taguchi, K. Shiraishi, T. Irisawa, T. Ohachi, Monte Carlo simulation for temperature dependence of Ga diffusion length on GaAs(0 0 1), Appl. Surf. Sci. 190 (2002) 517–520. https://doi.org/10.1016/S0169-4332(01)00930-8.
[194] T. Michely, J. Krug, Condensation, Diffusion and Nucleation, in: T. Michely, J. Krug (Eds.), Isl. Mounds At., Springer, Berlin, Heidelberg, 2004: pp. 13–59. https://doi.org/10.1007/978-3-642-18672-1_2.
[195] J.L. Tedesco, G.G. Jernigan, J.C. Culbertson, J.K. Hite, Y. Yang, K.M. Daniels, R.L. Myers-Ward, C.R. Eddy Jr., J.A. Robinson, K.A. Trumbull, M.T. Wetherington, P.M. Campbell, D.K. Gaskill, Morphology characterization of argon-mediated epitaxial graphene on C-face SiC, Appl. Phys. Lett. 96 (2010) 222103. https://doi.org/10.1063/1.3442903.
[196] Z. Guo, P. Zu, Z. Liu, M. Cecillia, Y. Cao, J. Li, J. Li, The role of etching on growth of adlayer graphene by chemical vapor deposition, Diam. Relat. Mater. 119 (2021) 108549. https://doi.org/10.1016/j.diamond.2021.108549.
[197] A. Luican, Single-Layer Behavior and Its Breakdown in Twisted Graphene Layers, Phys. Rev. Lett. 106 (2011). https://doi.org/10.1103/PhysRevLett.106.126802.
[198] P. Moon, Energy spectrum and quantum Hall effect in twisted bilayer graphene, Phys. Rev. B 85 (2012). https://doi.org/10.1103/PhysRevB.85.195458.
[199] K. Yu, Gate tunable optical absorption and band structure of twisted bilayer graphene, Phys. Rev. B 99 (2019). https://doi.org/10.1103/PhysRevB.99.241405.

[200] X. Zou, Terahertz Conductivity of Twisted Bilayer Graphene, Phys. Rev. Lett. 110 (2013). https://doi.org/10.1103/PhysRevLett.110.067401.

[201] A. Pirkle, J. Chan, A. Venugopal, D. Hinojos, C.W. Magnuson, S. McDonnell, L. Colombo, E.M. Vogel, R.S. Ruoff, R.M. Wallace, The effect of chemical residues on the physical and electrical properties of chemical vapor deposited graphene transferred to SiO2, Appl. Phys. Lett. 99 (2011) 122108. https://doi.org/10.1063/1.3643444.

[202] N. Liu, Z. Pan, L. Fu, C. Zhang, B. Dai, Z. Liu, The origin of wrinkles on transferred graphene, Nano Res. 4 (2011) 996–1004. https://doi.org/10.1007/s12274-011-0156-3.

[203] W. Zhu, T. Low, V. Perebeinos, A.A. Bol, Y. Zhu, H. Yan, J. Tersoff, P. Avouris, Structure and Electronic Transport in Graphene Wrinkles, Nano Lett. 12 (2012) 3431–3436. https://doi.org/10.1021/nl300563h.

[204] Y. Yao, T. Inoue, M. Takamura, Y. Taniyasu, Y. Kobayashi, Suppression of Nucleation Density in Twisted Graphene Domains Grown on Graphene/SiC Template by Sequential Thermal Process, Cryst. Growth Des. 24 (2024) 1682–1689. https://doi.org/10.1021/acs.cgd.3c01331.

[205] Z.H. Ni, H.M. Wang, Z.Q. Luo, Y.Y. Wang, T. Yu, Y.H. Wu, Z.X. Shen, The effect of vacuum annealing on graphene, J. Raman Spectrosc. 41 (2010) 479–483. https://doi.org/10.1002/jrs.2485.

[206] S.P. Koenig, N.G. Boddeti, M.L. Dunn, J.S. Bunch, Ultrastrong adhesion of graphene membranes, Nat. Nanotechnol. 6 (2011) 543–546. https://doi.org/10.1038/nnano.2011.123.

[207] F. Banhart, J. Kotakoski, A.V. Krasheninnikov, Structural Defects in Graphene, ACS Nano 5 (2011) 26–41. https://doi.org/10.1021/nn102598m.

[208] J. Zhang, K. Jia, L. Lin, W. Zhao, H.T. Quang, L. Sun, T. Li, Z. Li, X. Liu, L. Zheng, R. Xue, J. Gao, Z. Luo, M.H. Rummeli, Q. Yuan, H. Peng, Z. Liu, Large-Area Synthesis of Superclean Graphene via Selective Etching of Amorphous Carbon with Carbon Dioxide, Angew. Chem. Int. Ed. 58 (2019) 14446–14451. https://doi.org/10.1002/anie.201905672.

[209] T. Wang, J.-R. Huntzinger, M. Bayle, C. Roblin, J.-M. Decams, A.-A. Zahab, S. Contreras, M. Paillet, P. Landois, Buffer layers inhomogeneity and coupling with epitaxial graphene unravelled by Raman scattering and graphene peeling, Carbon 163 (2020) 224–233. https://doi.org/10.1016/j.carbon.2020.03.027.

[210] H. Huang, W. Chen, S. Chen, A.T.S. Wee, Bottom-up Growth of Epitaxial Graphene on 6H-SiC(0001), ACS Nano 2 (2008) 2513–2518. https://doi.org/10.1021/nn800711v.

[211] L. Huang, D. Zhang, F.-H. Zhang, Z.-H. Feng, Y.-D. Huang, Y. Gan, High-Contrast SEM Imaging of Supported Few-Layer Graphene for Differentiating Distinct Layers and Resolving Fine Features: There is Plenty of Room at the Bottom, Small 14 (2018) 1704190. https://doi.org/10.1002/smll.201704190.

[212] P. Landois, T. Wang, A. Nachawaty, M. Bayle, J.-M. Decams, W. Desrat, A.-A. Zahab, B. Jouault, M. Paillet, S. Contreras, Growth of low doped monolayer graphene on SiC(0001) via sublimation at low argon pressure, Phys. Chem. Chem. Phys. 19 (2017) 15833–15841. https://doi.org/10.1039/C7CP01012E.

List of publications

Relating publications to this dissertation:

1. **Yao Yao**, Ryota Negishi, Daisuke Takajo, Makoto Takamura, Yoshitaka Taniyasu and Yoshihiro Kobayashi. "**Scanning probe analysis of twisted graphene grown on a graphene/silicon carbide template**", Nanotechnology 33 (2022): 155603.
   DOI: 10.1088/1361-6528/ac473a

2. **Yao Yao**, Taiki Inoue, Makoto Takamura, Yoshitaka Taniyasu and Yoshihiro Kobayashi. "**Suppression of nucleation density in twisted graphene domains grown on graphene/SiC template by sequential thermal process**", Crystal Growth & Design 24.4 (2024): 1682-1689.
   DOI: 10.1021/acs.cgd.3c01331

3. **Yao Yao**, Taiki Inoue, Makoto Takamura, Yoshitaka Taniyasu and Yoshihiro Kobayashi. "**CO_2-assisted nucleation of twisted graphene on graphene/SiC templates**". In preparation.

Co-author:

1. Ryota Negishi, Chaopeng Wei, **Yao Yao**, Yui Ogawa, Masashi Akabori, Yasushi Kanai, Kazuhiko Matsumoto, Yoshitaka Taniyasu, Yoshihiro Kobayashi. "**Turbostratic Stacking Effect in Multilayer Graphene on the Electrical Transport Properties**", Physica status solidi (b), 257 (2020): 1900437
   DOI:10.1002/pssb.201900437

2. Kaipeng Rong, Ryosuke Noro, Hayato Nishigaki, Mingda Ding, **Yao Yao**, Taiki Inoue, Ryuji Katayama, Yoshihiro Kobayashi, Kazunari Matsuda, Shinichiro Mouri. "**Far-reaching Remote Doping for Monolayer MoS2 Using Ferroelectric Substrate: Unveiling the Impact of h-BN Spacer Thickness**", ACS Applied Electronic Materials 6, 8 (2024): 5914–5922.
   DOI: 10.1021/acsaelm.4c00880

List of attended scientific conferences

International conferences:

1. **Yao Yao**, Taiki Inoue, Makoto Takamura, Yoshitaka Taniyasu and Yoshihiro Kobayashi. “Control of graphene island nucleation on graphene/SiC template by sequential thermal processes in vacuo without air exposure”, The 23rd International Conference on the Science and Applications of Nanotubes and Low-Dimensional Materials (NT'23), Arcachon France, (June 4-9, 2023). (Poster)

2. **Yao Yao**, Taiki Inoue, Makoto Takamura, Yoshitaka Taniyasu and Yoshihiro Kobayashi. “Twisted graphene growth on graphene/SiC template using sequential thermal processes in vacuo without air exposure”. 2022 MRS Fall Meeting, Boston USA, (Nov.27-Dec.2, 2022). (Poster)

Domestic conferences:

1. **Yao Yao**, Taiki Inoue, Makoto Takamura, Yoshitaka Taniyasu and Yoshihiro Kobayashi. “Clean environment effect on nucleation of twisted graphene islands grown on graphene/SiC template by serial thermal process without air exposure”, 2022 年第 83 回応用物理学会秋季学術講演会（東北大学河内北キャンパス＆オンライン、2022 年 9 月 20-23 日）(Oral)

2. **Yao Yao**, Taiki Inoue, Royta Negishi, Makoto Takamura, Yoshitaka Taniyasu, Yoshihiro Kobayashi. “Lateral growth of twisted graphene on graphene/SiC template in a continuous vacuum environment", 1P-55、2021 年 第 61 回フラーレン・ナノチューブ･グラフェン総合シンポジウム（オンライン、2021 年 9 月 1 日）(Oral)

3. **姚 瑶**、井ノ上 泰輝、根岸 良太、高村 真琴、谷保 芳孝、小林 慶裕: “グラフェン/ SiC テンプレート上に乱層グラフェンの形成メカニズム”、19p-P01-18、2021 年第 68 回応用物理学会春季学術講演会（オンライン、2021 年 3 月 16 日～19 日）(Oral)

4. **Yao Yao**, Ryota Negishi, Yuki Fukaya, Makoto Takamura, Yoshitaka Taniyasu and Yoshihiro Kobayashi. “Temperature dependence of twisted graphene formation on graphene/silicon carbide template”, 9a-Z29-8、2020 年 第 81 回応用物理学会秋季学術講演会（オンライン、2020 年 9 月 8 日～11 日). (Oral)

5. **Yao Yao**, Ryota Negishi, Daisuke Takajo, Yuki Fukaya, Makoto Takamura, Yoshitaka Taniyasu and Yoshihiro Kobayashi. “Growth mechanism of twisted graphene layers on graphene/silicon carbide template”, 14p-A403-5、2020 年 第 68 回応用物理学

会春季学術講演会（上智大学、2020 年 3 月 12 日～15 日）. (Oral)

6. **Yao Yao**, Ryota Negishi, Daisuke Takajo, Yuki Fukaya, Makoto Takamura, Yoshitaka Taniyasu, Yoshihiro Kobayashi. “Growth mechanism of twisted graphene layers on graphene/silicon carbide template”, 新学術領域「ハイブリッド量子科学」第 10 回領域会議（2020 年 2 月 25 日）(Poster)

7. **Yao Yao**, Ryota Negishi, Daisuke Takajo, Makoto Takamura, Yoshitaka Taniyasu, Yoshihiro Kobayashi. “Structural analysis of twisted graphene by scanning probe microscope grown on template graphene”, 21a-PB1-29、2019 年第 80 回応用物理学会秋季学術講演会（北海道大学、2019 年 9 月 18 日～21 日）. (Poster)

8. **Yao Yao**, Ryota Negishi, Chaopeng Wei, Yui ogawa, Yoshitaka Taniyasu, Yoshihiro Kobayashi. “Analysis of staking structure in the multilayer graphene grown on monolayer graphene template”, 新学術領域「ハイブリッド量子科学」第 8 回領域会議（沖縄科学技術大学院大学 OIST、2019 年 1 月 9 日～10 日）. (Poster)

Co-author:

1. K. Rong, R. Noro, H. Nishigaki, M. Ding, **Y. Yao**, T. Inoue, R. Katayama, Y. Kobayashi, S. Mouri. “DOPING EFFECT OF MOS2 USING PERIODICALLY POLARIZATION-INVERSED SUBSTRATE”, The 23rd International Conference on the Science and Applications of Nanotubes and Low-Dimensional Materials (NT'23), Arcachon France, (June 4-9, 2023), P045.

2. 亀井 翔太, **姚 瑶**, 井ノ上 泰輝, 小林 慶裕：“CO2 添加化学気相成長によるテンプレート上グラフェン層状成長”, 2024 年 第 71 回 応用物理学会 春季学術講演会（東京都市大学世田谷キャンパス＆オンライン、2024 年 3 月 22-25 日）

3. 亀井 翔太, **姚 瑶**, 井ノ上 泰輝, 小川 友以, 高村 真琴, 谷保 芳孝, 小林 慶裕“乱層・多層グラフェンの化学気相成長における成長テンプレートの影響” 2023 年第 70 回応用物理学会春季学術講演会（上智大学四谷キャンパス＋オンライン、2023 年 3 月 15～18 日）

4. 根岸 良太、魏 超鵬、**姚 瑶**、小川 友以、谷保 芳孝、小林 慶裕: “グラフェンテンプレート上に成長した多層グラフェンの積層構造と電気伝導解析”, 19p-311-13、2018 年第 79 回応用物理学会秋季学術講演会（名古屋国際会議場、2018 年 9 月 18 日～21 日）

5. Chaopeng Wei, **Yao Yao**, Ryota Negishi, Yui Ogawa, Masashi Takamura, Yoshitaka Taniyasu and Yoshihiro Kobayashi. “Turbostratic multilayer graphene synthesis on CVD graphene template toward improving electrical performance”, 14th

International Conference on Atomically Controlled Surfaces, Interfaces and Nanostructures, Sendai, (Oct. 21-25, 2018). (Oral)

Acknowledgments

First and foremost, I wish to express my deepest gratitude to everyone who has guided, supported, and encouraged me throughout my academic journey. Their selfless assistance and profound influence have been instrumental in shaping my growth as a researcher and as an individual.

I am deeply thankful to Professor Kobayashi for his exceptional academic guidance and unwavering support during my doctoral studies. His profound expertise and consistent encouragement have not only inspired my research but also provided me with the confidence and direction to navigate the challenges of scientific exploration. I am sincerely grateful for the time and effort he has dedicated to fostering my academic growth.

I also wish to extend my heartfelt thanks to Assistant Professor Inoue for his patient guidance and insightful advice. His extensive knowledge and meticulous explanations have helped me overcome numerous challenges, deepen my understanding of complex academic issues, and significantly enhance my scientific writing skills.

My special thanks go to Professor Negishi for his invaluable mentorship in introducing critical experimental techniques. His constructive feedback and invaluable suggestions have enriched my research experience, broadened my technical expertise, and improved the quality of my work, enabling me to tackle academic challenges with greater confidence.

Furthermore, I am deeply grateful to Professor Taniyasu and Professor Takamura for providing essential graphene/SiC and copper-based monolayer graphene samples for my initial research. Their professional insights and generous support have laid a solid foundation for my early studies and opened doors to new research opportunities.

I would also like to thank NTT Basic Research Laboratories and II-VI Japan Incorporated for their generous provision of crucial substrate materials. Their support has

been indispensable for the successful execution of my experiments and has greatly facilitated my progress in addressing technical challenges.

My sincere appreciation goes to the professors who reviewed my doctoral dissertation. Their thoughtful feedback and constructive suggestions have greatly enhanced the quality and depth of my work.

I am equally grateful to all my colleagues in the laboratory. In particular, I wish to thank Mr. Kamei, Mr. Wei, and Mr. Chou from the CVD twisted graphene group. Your collaborative spirit and teamwork have been invaluable in overcoming experimental challenges and advancing my research. I also want to extend my gratitude to other lab members, including Mr. Ding, Mr. Liu, Mr. Shimizu, Mr. Mizuno, Mr. Akamatsu, Mr. Suzuki, Mr. Hirai, Mr. Hayato Watanabe, Mr. Nishio, Mr. Yoshida, and Mr. Atsutaka Watanabe, for their priceless cooperation and support, which have filled our laboratory with innovation and warmth. A special mention goes to Mr. Liu for his encouragement and thoughtful care, which made me feel at home while pursuing my studies abroad.

Finally, I wish to express my heartfelt thanks to everyone who has supported and encouraged me during this academic journey. Your guidance and contributions have helped me overcome obstacles, broaden my horizons, and motivated me to pursue further achievements in my field. Without your selfless dedication and silent support, none of this would have been possible.

Thank you all from the bottom of my heart.